STUDIES ON ANTIMICROBIAL PROPERTIES OF METALS AND METAL OXIDE BASED NANOSTRUCTURES

A THESIS

Submitted to

THAPAR UNIVERSITY, PATIALA

For the award of

DOCTOR OF PHILOSOPHY

Submitted by

CHANDNI

Under the Supervision of

Dr. B. Chudasama (Assistant Professor)	Dr. O. P. Pandey (Senior Professor)

School of Physics and Materials Science
Thapar University
Patiala, Punjab
INDIA

JULY 2014

DEDICATION

This thesis is dedicated to my entire loving and supportive family

My parents whose constant encouragement helps me to reach all goals

My brother whose guidance keeps me moving forward in a positive direction
&
My sister and brother-in-law for their support at every moment

CERTIFICATE

This is to certify that the thesis entitled **"Studies on Antimicrobial Properties of Metals and Metal Oxide Based Nanostructures"** which is being submitted by **Chandni** in fulfilment of the requirements for the award of the degree of Doctor of Philosophy in the School of Physics and Materials Science, Thapar University, Patiala (Punjab), India is an exclusive record of candidate's own research work under our supervision. The thesis in part or in full has not been submitted in any other University or Institute for the award of any degree. The thesis is fit to be considered for the award of degree of Doctor of Philosophy.

Dr. B. Chudasama
Assistant Professor
School of Physics and Materials Science
Thapar University
Patiala-147004 (INDIA)

Dr. O. P. Pandey
Senior Professor
School of Physics and Materials Science
Thapar University
Patiala-147004 (INDIA)

Date: July 11, 2014
Place: Patiala, India

ACKNOWLEDGEMENT

An acknowledgement in my thesis is just a small gesture and doesn't truly represent how much I appreciate the influence that many people have had on my life. It is a pleasant task to express my thanks to all those who contributed in many ways to my doctoral work and made it an unforgettable journey for me.

With deep regards and profound respect, I take this opportunity to express my deep sense of gratitude and indebtedness to my supervisor Dr. Bhupendra Chudasama, Assistant Professor, Thapar University, Patiala for his trust and encouragement at every stage. His vision, optimistic attitude, enthusiasm and continual pursuit of scientific challenges have provided me with lifetime benefits. I am glad to be his student; a million thanks to him for making my dreams come true.

I would also like to express my gratitude towards my co-supervisor Dr. O. P. Pandey, Senior Professor, Thapar University, Patiala. I am thankful to him for his guidance and valuable suggestions throughout this research work. It is a fortune for me being associated with him.

I am indebted to Prof. Kulvir Singh, Head, School of Physics and Materials Science, Thapar University for his invaluable support and cooperation. I would also like to thank doctoral committee members Dr. S. D. Tiwari and Dr. Bonamali Pal for their valuable advice at each and every stage of my doctoral work. I would never have been able to finish my dissertation without their guidance. Thanks to Dr. P. K. Bajpai, Dean, Research and Sponsored Projects, Thapar University, Patiala for providing the necessary research facilities to meet the goals of this assignment. I would also like to extend my warm appreciation towards faculties and staff of SPMS.

I want to thank Dr. Anjana K. Vala, Bhavnagar University, Bhavnagar for her kind help and assistance in carrying out experiments on antibacterial activities. I would like to express my sincere thanks to Prof. Dinesh Goyal, Head, Department of Biotechnology, Thapar University, Patiala for extending facilities of Industrial Microbiology lab. I am thankful to Purnima Sharma for her help and support during experimentation in Microbiology lab. I am also thankful to SAIF, IIT

Bombay and SAI Labs, Thapar University for extending characterization facilities. Deep thanks must be given to Dr. Nidhi Andhariya for her kind assistance, discussion and suggestions during my doctoral work.

With great appreciation, I shall acknowledge all my lab mates Deepika Jain, Rajni Mittal, Sangeeta Arora, Mintu Tyagi, Paramjot Jha and Rubina Bansal. Many thanks to my juniors Parveer Kaur and Navjot Dhindsa for their love and cheerful company. Many friends have helped me stay sane through these difficult years. Their support and care helped me to stay focused on my Ph.D work. I greatly value their friendship and deeply appreciate their belief in me. Thanks to Rajinder Kaur, Samiksha Verma and Suninder Jeet for their love and affection during my stay at Thapar University. Special appreciation goes to my close friends Rajan Singh and Samita Thakur for their love, care, suggestions and moral support. I truly believe that this thesis would not have been complete without their help and co-operation. Words fail me to express my appreciation for them.

I am indebted to University Grants Commission (UGC) and Council of Scientific & Industrial Research (CSIR), New Delhi for Junior and Senior Research Fellowships.

I am grateful to my dad, brother, sister and brother-in-law for their unflagging patience, love and constant support. This acknowledgement is incomplete without the mention of my loving nephew *Taanshu*, whose charming smile always de-stressed me during these difficult days. My special thanks are due to my loving mom, who inspired me to be strong and brave throughout the journey of my life.

Last but not the least; I would like to pay high regards to almighty God for giving me skills, wisdom, knowledge and ability to work hard to reach where I am today. Moreover, I thank God for the blessings and support He has showered on me through my family, friends, professors and colleagues. Without His blessings and support, this thesis would have never been possible.

(Chandni)

List of Publications

SCI Journals

1. **Chandni,** Nidhi Andhariya, O.P.Pandey and Bhupendra Chudasama, A Growth Kinetic Study of Ultrafine Monodispersed Silver Nanoparticles. RSC Advances 3, 1127-1136 (2013).
2. **Chandni Khurana,** Anjana K Vala, Nidhi Andhariya, O.P.Pandey and Bhupendra Chudasama, Antibacterial activity of silver: The role of hydrodynamic particle size at nanoscale, Journal of Biomedical Materials Research Part A, DOI: 10.1002/jbm.a.350 (2013).
3. **Chandni Khurana**, Anjana K Vala, Nidhi Andhariya, O.P.Pandey and Bhupendra Chudasama, Antibacterial activities of silver nanoparticles and antibiotics adsorbed silver nanoparticles against biorecycling microbes, Environmental Science: Processes & Impacts, DOI: 10.1039/C4EM00248B (2014).

Non-SCI Journals

1. **Chandni,** O.P.Pandey and Bhupendra Chudasama, Effect of Nucleation & Growth Temperatures on the Synthesis of Monodisperse Silver Nanoparticles, AIP Conf. Proc. 1512, 442-443 (2013).
2. **Chandni,** O.P.Pandey and Bhupendra Chudasama, Single Phase Synthesis of Highly stable Copper Nanoparticles, AIP Conf. Proc. 1536, 149-150 (2013).

Conference Presentations

1. **Chandni**, Poonam Benjwal, Nidhi Andhariya, Anjana Vala, O. P. Pandey and Bhupendra Chudasama, "Collidal silver nanostructures: Synthesis and antimicrobial activities" 22nd Annual General Meeting of Materials Research Society of India (AGM: MRSI), Bhopal, India. Feb 14-16 (2011).
2. **Chandni,** O.P.Pandey and Bhupendra Chudasama, "Size Controlled Synthesis of Silver Nanoparticles" National Conference on Emerging Trends in Chemistry-Biology Interface (ETCBI-2011), Kumaun University, Nainital, India. Nov 3-5 (2011).
3. **Chandni,** O.P.Pandey and Bhupendra Chudasama, "Ostwald ripening: A key to achieve silver nanostructure" 4th National Symposium for Materials Research Scholars (MR-12), Indian Institute of Technology Bombay, Mumbai, India. May 3-5 (2012).
4. **Chandni,** O.P.Pandey and Bhupendra Chudasama, "Effect of Nucleation & Growth Temperatures on the Synthesis of Monodisperse Silver Nanoparticles" 57th DAE Solid State Physics Symposium, Indian Institute of Technology Bombay, Mumbai, India. Dec 3-7 (2012).
5. **Chandni,** O.P.Pandey and Bhupendra Chudasama, "Single Phase Synthesis of Highly Stable Copper Nanoparticles" International Conference on Recent Trends in Applied Physics & Material Science (RAM 2013), Govt. College of Engineering & Technology, Bikaner, Rajasthan, India. Feb 1-2(2013).
6. **Chandni Khurana,** O.P.Pandey and Bhupendra Chudasama, "Low temperature Synthesis of Single Phase Copper Oxide Nanoparticles" National Conference on Innovative Molecules for Sustainable Future (NCIMSF 2013), Thapar University, Patiala, Punjab, India. Oct 24-26(2013).
7. **Chandni Khurana**, O. P. Pandey and Bhupendra Chudasama, "Enhanced Antibacterial Activity of Silver Nanoparticles Conjugated Commercial Antibiotics" International Conference on Nanoscience and Nanotechnology (ICNN-2013), Babasaheb Bhimrao Ambedkar University, Lucknow, India. Nov 18-20 (2013).
8. **Chandni Khurana,** O.P.Pandey and Bhupendra Chudasama, "Control of Nanoparticle Agglomeration: Role of Synthesis Technique and Surfactant" International Conference on Powder, Granule and Bulk Solids: Innovations and Applications (PGBSIA-2013), Thapar University, Patiala, Punjab, India. Nov 28-30 (2013).

Table of Contents

Chapter 3 Synthesis of Metals and Metal Oxide Nanostructures and Their Properties……………………………………….... 39-104

Chapter 4 Antibacterial Activity ………………………………………… 105-128

PREFACE

Infection is a biological process in which the host organism's body tissues are invaded by disease causing microorganisms like virus, bacteria, fungi and other macroparasites. Infectious disease is the outcome of interplay between pathogenic microorganisms and immune system of the host. In the history of human civilization, the epidemics suffered by mankind are due to the infectious diseases. Billions of humans were killed due to infections which were not curable. According to the World Health Organization report in the year 2002, 26% of the total deaths were caused by the infectious diseases. Nearly 14.7 million people died due to infections in the year 2002. The mortality caused by infectious diseases is expected to rise further due to environmental pollution and rapid changes in the ecosystem.

Anti-infective drugs are used in the curative and preventive health care to treat various infections caused by pathogenic microorganisms. An antibiotic is a substance that kills microorganisms or inhibits their growth. Antibiotics work on different mechanisms. Some of them kill the microorganisms, while the others just prevent their growth. Few antibiotics disrupt the bacterial cell walls or interfere with the genetic material of the cell, leading to death, while the others may prevent them from making important chemical compositions required for their growth.

To fight against infections, antibiotic is the only option available with pharmacologists. Even though antibiotics are widely used, cautions must be exercised while using them. Some common side effects that occur in patients include nausea, diarrhea, stomach pains, headache, fever, body and muscle aches and vomiting to life threatening diseases like abnormal blood clotting, kidney stones, blood disorders, etc. Antibiotics can decrease the effectiveness of birth control pills. Hence, there is an urgent need for the development of alternative medicines, which are as efficient as antibiotics but have no potential side effects.

Development of pathogenic strains of microorganisms that are resistant to most of the currently available antibiotics is another challenge in health care. For example, MRSA (methicillin resistant *S. aureus*) bacteria kill 5000 hospital patients a year in the UK alone. These strains are resistant to at least one antibiotic, which is presently available in the market and any method of attacking them not involving antibiotics, is becoming increasingly important. Microbes possess an internal mechanism of changing their structure so that the antibiotic no longer works. They develop ways to inactivate or neutralize the antibiotics. They can transfer gene coding for antibiotic resistance amongst them, making it possible for the microorganisms never exposed to an antibiotic to acquire resistance. Further, the development process of antibiotics is slow and lengthy and hence, developing new antibiotics will not be able to cope up the threats posed by the evolution of multidrug resistant strains of microorganisms. Hence, there is a vital and immediate need for the discovery of non-traditional medicines, against which microbes are unlikely to develop resistance. The new approach should be able to minimize the side-effects associated with the medication of traditional antibiotics.

Metal and metal oxide based materials are widely used for the treatment of infectious diseases since ancient time. However, technological advancement in the field of antibiotics had declined interest in these conventional medicines in the 20th century. Recent developments of multidrug resistant strains of microorganisms have rejuvenated interest in the antimicrobial properties of metals and metal oxides. The major objective of this thesis is to synthesize metals (silver and copper) and metal oxide (titanium dioxide) nanoparticles and evaluate their antimicrobial properties against clinically important pathogens and environmental friendly microorganisms, which are critical to sustain natural cycles.

First chapter of this thesis introduces subject of infection and infectious diseases. The details of epidemics caused by infectious diseases in the history of human civilization are overviewed to highlight the importance of this class of diseases. The concept of antibiotics is introduced, which is the only alternative available with pharmacologist for the treatment of infectious diseases. Detailed mechanism of microbial action of antibiotics is also reviewed along with their merits and demerits. The origin of resistance in microorganisms against antibiotics is reviewed in this introductory chapter. The need for alternate medical modality to fight against the threats raised by the development of resistance strains of microorganisms is pressed upon and the possibility of metals and metal oxide nanostructures to be used as non-conventional antibiotics to target multidrug resistance strains is explored. A brief review on possible environmental hazards of nanomaterial based non-traditional antibiotics is also presented in chapter - 1.

The second half of chapter - 1 reviews the existing state of art of nanomaterials' preparation with specific focus on tailored synthesis of metals (silver and copper) and metal oxide (titanium dioxide) nanostructures. Based on the existing literature, the correlation between processing parameters and their biological activities have been established. From the literature survey, it is found that no systematic correlation between the synthesis protocols and bioactivity of silver, copper and titanium dioxide nanoparticles exist, which can be used as authenticate and reliable source of information in nanomedicine.

The second chapter includes description of various characterization tools/techniques, which are used to characterize nanomaterials synthesized to fulfill the objectives of this thesis. The detailed experimental protocols of each characterization technique (XRD, PCS, FTIR, UV-visible spectroscopy, ICP-AES, TG/DSC, TEM, SEM/EDS) along with sample preparation details and measurement conditions are presented.

The third chapter is divided into three subparts. The first part of this chapter deals with the evolvement of synthesis protocols for size selective synthesis of silver nanoparticles. They are synthesized by chemical reduction technique in which oleylamine is used as both reducing and capping agent. Effect of various synthesis parameters like concentration of reducing/capping agent, nucleation temperature, nucleation time, growth temperature and growth time on nanoparticles' yield, their hydrodynamic, crystallite and physical size, morphology and plasmonic characteristics are studied. From the detailed investigation of synthesized nanoparticles by various characterization techniques, the optimized conditions for high yield, nearly monodisperse, water dispersible silver nanoparticles that can be directly used as antimicrobial agent in nanomedicine are being laid down.

Synthesis of copper nanoparticles by chemical reduction technique is described in the second part of chapter - 3. It has been established that three component system i.e. strong reducing agent ($NaBH_4$), weak reducing agent (L-ascorbic acid) and surfactant (PVP) is essential for the formation of metallic copper phase. Uniform, nearly monodisperse, ultra-small copper nanoparticles obtained under ambient conditions are stable against aggregation and oxidation. The plausible mechanism responsible for stabilization of copper nanoparticles' surface against oxidation is also provided.

Third part of chapter - 3 describes synthesis of undoped and cobalt (0-2 wt%) doped Titanium dioxide nanoparticles by sol-gel technique. The effect of cobalt doping on the optical band gap of anatase phase of TiO_2 nanoparticles have been evaluated by diffuse reflectance UV-visible spectroscopy. It has been found that increasing cobalt concentration in the TiO_2 matrix reduces its band gap from 3.03 eV to 1.93 eV. By cobalt doping, the spectral response of TiO_2 nanoparticles has been shifted from UV region to the visible region of the electromagnetic spectrum, which is an essential condition for photoinduced bioactivity of TiO_2 nanoparticles.

Evaluation of antimicrobial activities of as-synthesized and antibiotics adsorbed nanoparticles is the subject matter of chapter - 4. The antimicrobial activities of nanoparticles and antibiotic adsorbed nanoparticles have been evaluated against clinically important pathogenic strains of *E. coli*, *S. aureus* and *P. vulgaris* and eco-friendly microorganisms of *B. subtilis* and *P. fluorescens*. The antimicrobial activities of a particular antibiotic against pathogenic / eco-friendly microorganism under test have been evaluated in terms of minimum inhibitory concentration (MIC) and zone of inhibition (ZIH) by micro-dilution method and disk diffusion test, respectively. Highest biocidal activity is observed for copper nanoparticles amongst the studied nanoparticulate systems. The MIC values of copper nanoparticles ranges between 20-50 µg/mL. For silver nanoparticles, the MIC values lies in the range of 25-150 µg/mL. This observation is in contradiction with the existing literature where highest biocidal activity is reported for silver nanoparticles amongst all nano-antimicrobial systems. The exact reason behind observed enhanced antimicrobial activities of copper nanoparticles is not completely understood. This enhanced biocidal activity of copper nanoparticles could be ascribed to their colloidal stability, ultra-small size and high oxidation resistance. No significant inhibition of organism growth is observed under light or dark conditions in the tested concentration range (0 - 500 µg/mL) of TiO_2. Irrespective of the optical band gap (i.e. Co-dopant concentration), no MIC of TiO_2 is observed for pathogenic/ecofriendly microorganisms.

The antimicrobial activities of silver nanoparticles increase by 60-346% for tetracycline adsorption and 70-289% for kanamycin adsorption on nanoparticles. For tetracycline adsorbed copper nanoparticles, the enhancement is in the range of 0-49% and for kanamycin adsorbed copper nanoparticles, it improves by 0-20%. From these results, it is concluded that when antibiotics adsorbed on silver nanoparticles, it drastically enhances the biocidal activities of silver nanoparticles while same is not happening for copper nanoparticles. This might be because of adsorption of copper nanoparticles at biologically active sites of antibiotics. The phenomenological description of mechanism governing the microbial activities of nanoparticles is also provided in this chapter.

Chapter - 5 summarizes the important findings along with the scope for future work in the proposed field of antibacterial nanobiotechnology.

CHAPTER 1

INTRODUCTION

1.1 Infection

Infection is a biological process in which the host organism's body tissues are invaded by disease causing microorganisms [1]. It is a three step process. In the first step, microorganism(s) multiplies on the tissues followed by their interaction with the host and release of toxins into the host tissues. Infectious diseases are caused by the growth of pathogenic virus, bacteria, fungi and other macroparasites. In healthy humans, only few microorganisms can cause disease. Infectious disease is the outcome of the interplay between these few pathogens and the immune system of the host. The appearance and severity of a disease depends on the ability of the pathogen to damage the host and the ability of the host to resist the pathogen. Based on the status of the host defense, pathogens are classified as primary and opportunistic. Primary pathogens cause disease due to their activity in a normal healthy host while opportunistic pathogens cause infections in a host having depressed resistance [1]. Such depressed resistance may occur due to genetic disorder, over exposure to antimicrobial drugs or immunosuppressive chemicals, exposure to radiations or due to immunosuppressive diseases like HIV [1].

Infections are generally classified on the basis of anatomic location or organ system that is infected. This includes urinary tract infection, skin infection, respiratory tract infection, odontogenic infection, vaginal infections and Intra-amniotic infection like pneumonia, meningitis and salpingitis. Symptoms of an infection includes fatigue, loss of appetite, weight loss, aches, fever, chills, rashes, coughing, running nose, night sweats, pain, etc.

1.2 Infectious Diseases

A disease that affects humans over the vast stretch of globe or geographical area is called epidemic. All epidemics suffered by the mankind are due to the infectious diseases. In between 541-750, 50-60% of Europe's population was killed by Plague [2]. In 1347-1352, 25 million population of Europe was killed by pandemics called "Black Death". The pathogen *Yersinia pestis*, a cause of several forms of plague has reduced the world population from 450 million to 350 million in the 14th century. In 1556-1560, influenza epidemic has an estimated mortality rate of 20% [3]. In 18th century, 60 million Europeans were killed by smallpox. 30% of infected patients including 80% children under the age of 5 were died from the disease and rest survivors went blind [4]. In 19th century, a quarter of the adult population of Europe was killed by tuberculosis [5]. In 1918, influenza pandemic killed 50 million people, which is approximately 2% of the world population at that time [6]. Even today, influenza kills 5 million people every year [6]. World Health Organization data shows that nearly 14.7 million of total death (25.9%) in the year 2002 was caused by infectious diseases. Various infections caused by pathogens are listed in **Fig. 1.1** [1]. The details of mortality caused by various infectious diseases are listed in **Table 1.1** [7].

Table 1.1 Leading cause of mortality in the year 2002 by various infectious diseases.

Cause of death	Deaths (in millions)	Percentage of all deaths
All infectious diseases	14.70	25.9
Lower respiratory infections	3.90	6.9
HIV/AIDS	2.80	4.9
Diarrheal diseases	1.80	3.2
Tuberculosis	1.60	2.7
Malaria	1.30	2.2
Measles	0.60	1.1
Pertussis	0.29	0.5
Tetanus	0.21	0.4
Meningitis	0.17	0.3
Syphilis	0.16	0.3
Hepatitis B	0.10	0.2
Tropical diseases	0.13	0.2

1.3 Antibiotics

Anti-infective drugs are used in the preventive and curative healthcare to treat infections caused by various pathogenic microorganisms [6]. Anti-infective drugs are of four types, namely, antibacterial (antibiotic), antiviral, antifungal and antitubercular. Traditional antibiotics work only against bacterial infections and are not effective on viruses or fungus. Antibiotics are low-molecular-weight microbial metabolites that inhibit the growth of other microorganisms at low concentrations [1]. The expression "inhibition of the growth of other microorganisms" by an antibiotic, means inhibition of the ability of the microorganism to reproduce and consequently, restraint the growth of the bacterial population rather than of an individual cell. Antibiotic activity is termed as bactericidal when inhibition is permanent. The antibiotic is said to be bacteriostatic if the inhibition is lost when it is removed from the medium [1].

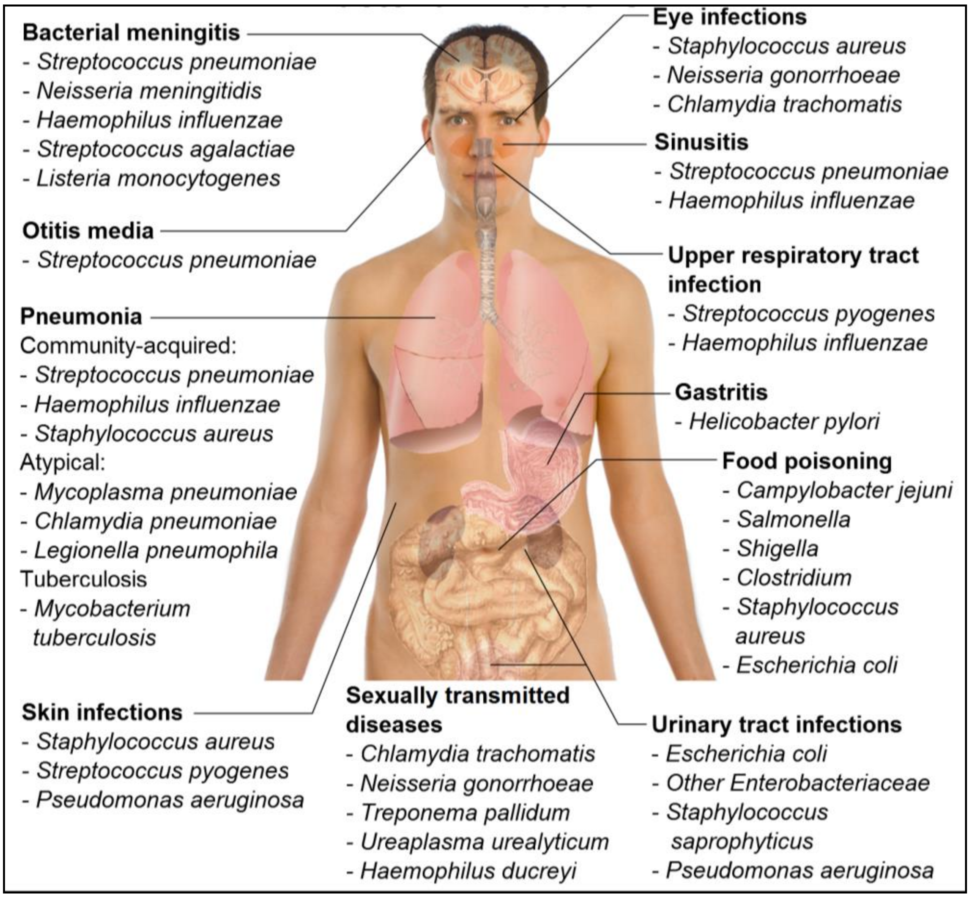

Fig. 1.1 Various infections in humans caused by pathogenic bacterial strains [1].

Antibiotics work on different mechanisms. They are summarized in **Fig. 1.2** [8]. Some of them kill the microorganisms while others just prevent their growth. Few of them disrupts the bacterial cell walls or interfere with the genetic material of the cell, leading to cell death, while the others may prevent them from making important chemical compositions required for cell growth [8]. Penicillin was the first antibiotic discovered as natural products from the mold *Penicillium*. All Penicillin derivatives produce their bactericidal effects by inhibition of bacterial cell wall synthesis [9]. They prevent bacteria from using a substance that is necessary for the maintenance of cell wall. Unable to use this substance for the cell wall maintenance, the bacteria swell, rupture, assume unusual shapes, and finally die [8, 9]. The Penicillin may be bactericidal or bacteriostatic. They are used to treat various infections such as urinary tract infections, septicemia, meningitis, intra-abdominal infection, gonorrhea, syphilis, pneumonia, respiratory, ear, nose, skin and throat infections, etc. [9].

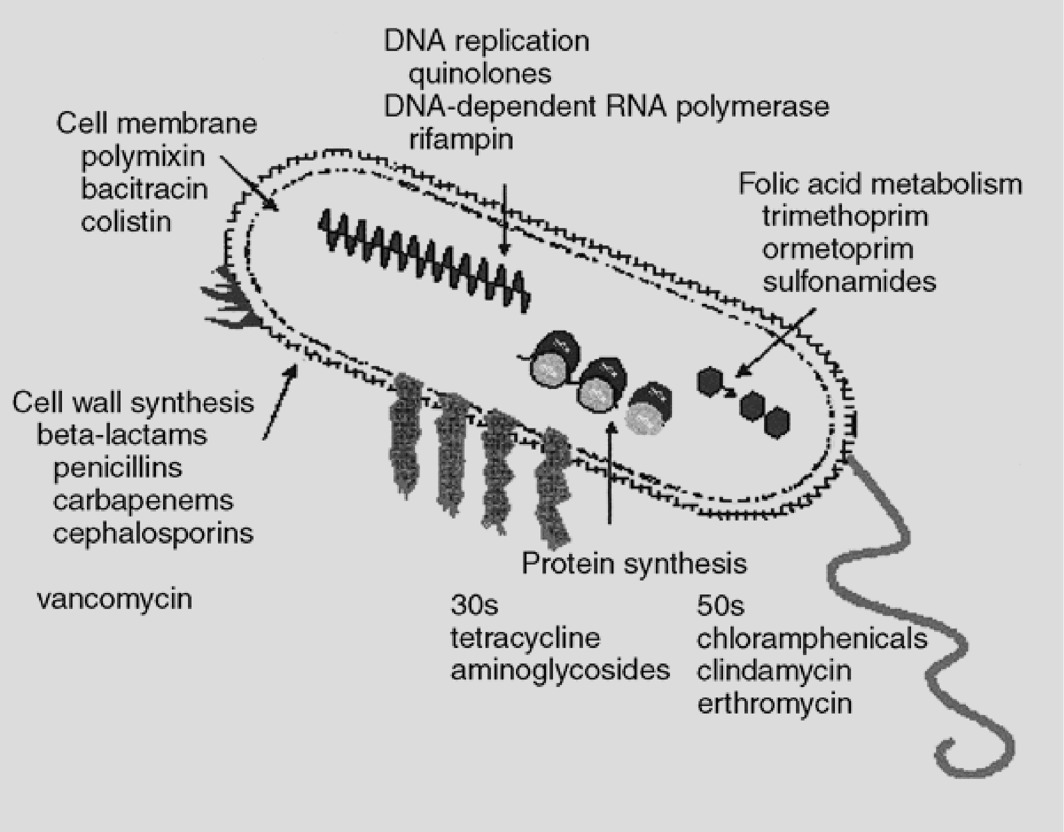

Fig. 1.2 Various modes of antibacterial action of antibiotics [8].

Apart from Penicillin, the other important classes of antibiotics are [8]:

1. Tetracycline
2. Kanamycin
3. Cephalosporins
4. Fluoroquinolones
5. Macrolides
6. Aminoglycosides

Antibiotics are widely used in pharmacopoeia to treat diseases caused by infections. Antibiotics need to be used with caution. Some common side effects that occur in patients which are treated with antibiotics include nausea, diarrhea, stomach pains, headache, fever, body and muscle aches, vomiting, etc. Penicillin's side effects also include severe skin rashes accompanied by itching and sometimes peeling. It can also create a confused state of mind with an increase in agitation and anxiety [1, 8, 9]. Antibiotics can also decrease the effectiveness of birth control pills. They do not hurt unborn babies but there are potential risks involved if a newborn baby takes it orally through mother's milk. Rare, but more serious side effects include the formation of kidney stones with the sulphonamides, abnormal blood clotting with some of the cephalosporin, increased sensitivity to the sun with the tetracycline, blood disorders with trimethoprim, and deafness with erythromycin and the amino glycosides [1, 8, 9]. Hence, there is an urgent need for the development of alternative medicines, which are as efficient as antibiotics but have no or minimum side effects.

1.4 Antibacterial Action

An antibiotic inhibits the microbial growth. Microbes grow by reproduction of cells i.e. a single cell divides into two daughter cells. For antibacterial activity of antibiotic it must

1. Enter into the bacterial cell and should reach the site of action
2. Physically binds to a specific cellular structure (molecule or macromolecule), which is essential for maintenance of cell growth or homeostasis and
3. Markedly inhibit this process.

At the cellular level, an antibiotic can be bactericidal or bacteriostatic. The bactericidal effect may result from either of two mechanisms: (i) Irreversible disruption of the cell integrity due to the interaction between antibiotic and target molecule and (ii) Irreversible binding via covalent interaction between antibiotic and enzyme or cellular structure. If the complex between antibiotic and target moiety dissociates and the target molecule resumes its normal functioning when an antibiotic is removed from the medium than the corresponding antibiotic is termed as bacteriostatic.

Antibiotics can inhibit cellular growth by interfering with essential metabolic processes. Some antibiotics block the energy-providing mechanisms, while the others interfere with the synthesis of intermediate metabolites or polymerization processes. The mechanism or mode of action of an antibiotic is the specific mechanism by which inhibition is achieved. Antibiotics are classified according to the processes by which they interfere with the bacterial cell culture. They are commonly classified into following four groups:

1. Inhibitors of cell wall synthesis
2. Inhibitors of the replication or transcription of genetic material
3. Inhibitors of protein synthesis
4. Inhibitors of cell membrane functions

1.5 Advantages of Antibiotics

Antibiotics are the cost effective and affordable mode of medication that is used for the treatment of vast variety of infections caused by microorganisms [1, 8]. With the advancement in the medicinal chemistry, antibiotics are discovered to treat infections of fatal diseases, which are otherwise incurable and have claimed millions of lives in the history of human civilization [2-6]. Antibiotics can be administered orally, intravenously or topically. They are relatively inexpensive to produce and available in natural, semi synthetic and synthetic varieties. They have different usages depending on their strength and makeup. A single antibiotic is effective against infections caused by multiple microorganisms. Antibiotics are also used to prevent damages to fruits and grains by bacterial and fungal infections. Small quantities of antibiotics are also used to stimulate animal growth. Some common antibiotics are also used as food preservatives.

1.6 Limitations of Antibiotics

Despite of massive advantages associated with the medication of antibiotics for the treatment of common infections like pimples to fatal and life threating diseases like tuberculosis; medical practitioners have found challenging and worrisome limitations of antibiotics [9]. The key issue associated with the medication of antibiotics is their unrestrained overuse worldwide. This has caused exponential rise in the number of microorganisms, which are resistant to one or more antibiotics [1, 8]. The other major limitation associated with the medication of antibiotics is their inherent and eventually toxicity towards healthy cells, which causes severe toxicity in the body that results into numerous side effects. Some antibiotics can also cause complications like yeast infections. Higher dose of antibiotics may develop resistance in the microorganisms which were never exposed to that particular antibiotic [10].

1.6.1 Development of Resistance against Antibiotics

Many infectious diseases which were previously curable by specific antibiotics are no longer curable. This is due to the development of resistance in pathogenic microorganisms, which are causing these infectious diseases. Development of resistant strains of microorganisms is of high clinical importance. A bacterial strain, which is susceptible to an antibiotic is said to be resistant when the minimum inhibitory concentration (MIC) of antibiotic no longer inhibits the growth of that particular strain [1, 8, 10]. In other words, a bacterial strain is said to be resistant to an antibiotic if it can grow in the presence of an antibiotic whose concentration is equal or greater than that reachable in serum or tissue.

Microorganisms will develop resistance against a particular antibiotic if either of the following conditions is established [1]:

1. Antibiotic transforms into an inactive form.
2. Alteration/modification in the target site of the antibiotic.
3. Change in the permeability of the microorganism.
4. Increased production of structures that inhibits activity of antibiotics.

These possible mechanisms are summarized in **Fig. 1.3**. Many resistance strains of bacteria produce enzymes, which are capable of chemically transforming the antibiotic into an inactive product. Amongst the enzymes, the most important are: peptidases, acetyl-transferases, phosphoryl-transferases and adenyl-transferases [11-14]. The other mode of development of antibiotic resistance is by modification of antibiotic target. Many antibiotics functions by deactivating a receptor [11]. A receptor is nothing but a target protein where the antibiotics bind and forms a complex. Large number of bacterial strains through mutation develops a target protein, which is unable to bind to the antibiotic or retains its function even after binding [12, 13]. The third possibility that could lead to the development of resistance is due to the change in the permeability of the cell membrane. Generally antibiotics enter into the bacterial cell membrane via passive diffusion or by specific active transport. When the physical characteristics of antibiotics are compatible with the passive diffusion, it is unlikely to have mutation by means of change in the permeability of the cell membrane as it may be lethal to the cell itself [12]. However, there are good chances of mutation, when the antibiotics transports into the cell membrane via active transport. Normally, specific transport proteins are involved in active transport of antibiotics across the cell membrane. Alteration in the structure of this protein leads to the development of resistance. In the fourth possibility, bacterial cell produces specific enzymes that binds with the antibiotics and thus develops mutation against specific antibiotics [14].

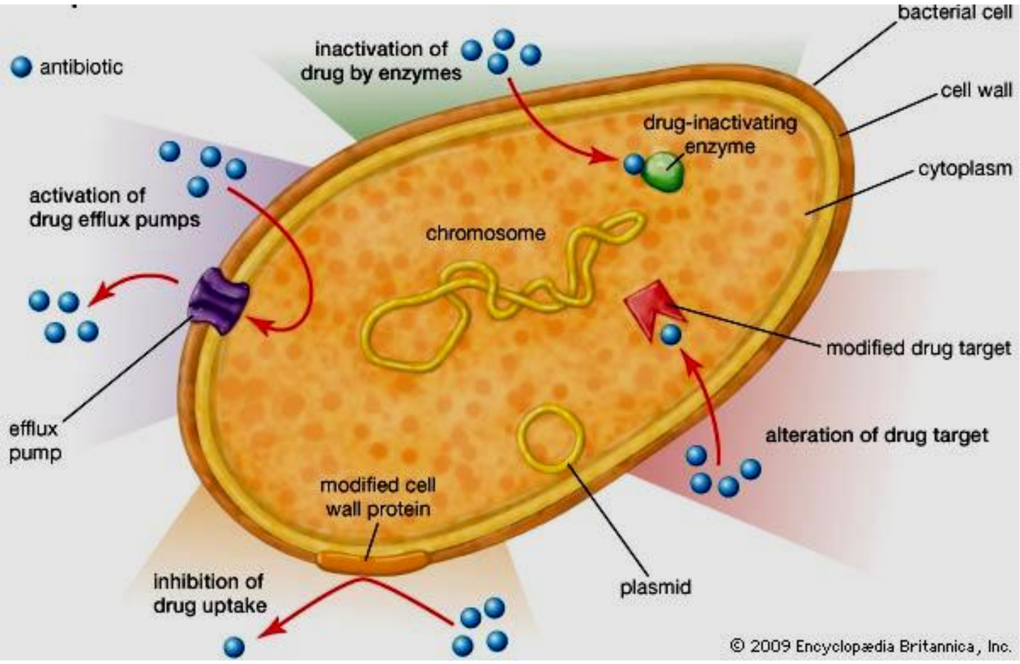

Fig. 1.3 Mechanisms of development of resistance in bacterial strains [6].

1.7 Multidrug Resistance

When a pathogenic strain is resistant to two or more than two antibiotics through unrelated mechanisms, they are said to have acquired multidrug resistance. Development of resistant strains of microorganisms that are resistant to most of the currently available antibiotics is a major challenge in health care [11]. For example, MRSA (methicillin resistant *S. aureus*) bacteria kill 5000 hospital patients a year in the UK alone [12]. These strains are resistant to more than one antibiotics, which are currently available in market and any method of attacking these resistant strains without antibiotics is becoming increasingly important [12]. Microbes possess an internal mechanism of changing their structure so that the antibiotic no longer works. They develop ways to inactivate or neutralize the antibiotic. They can transfer genes coding for antibiotic resistance amongst them, making it possible for the microorganisms never exposed to an antibiotic to acquire resistance. Hence, there is a vital and immediate need for the development of non-traditional medicines, against which microbes are unlikely to develop resistance. The new approach should be able to overcome the drawbacks of narrow targeting antibiotics [1, 8, 9].

1.8 Possible Solutions to Drug Resistant Strains

Resistance towards microorganisms is fast growing against antibiotics and there exist resistant strains, which have developed mutation against at least one of the first line antibiotics. Number of antibiotics available in the market is rapidly decreasing. Although the number of available antibiotics is quite large, development of resistant strains has created an alarming situation. This is due to the slow and expensive process of discovery of antibiotics and their commercialization. The steps involved in the discovery of a potential antibiotic compound to its commercialization are summarized in **Fig. 1.4**.

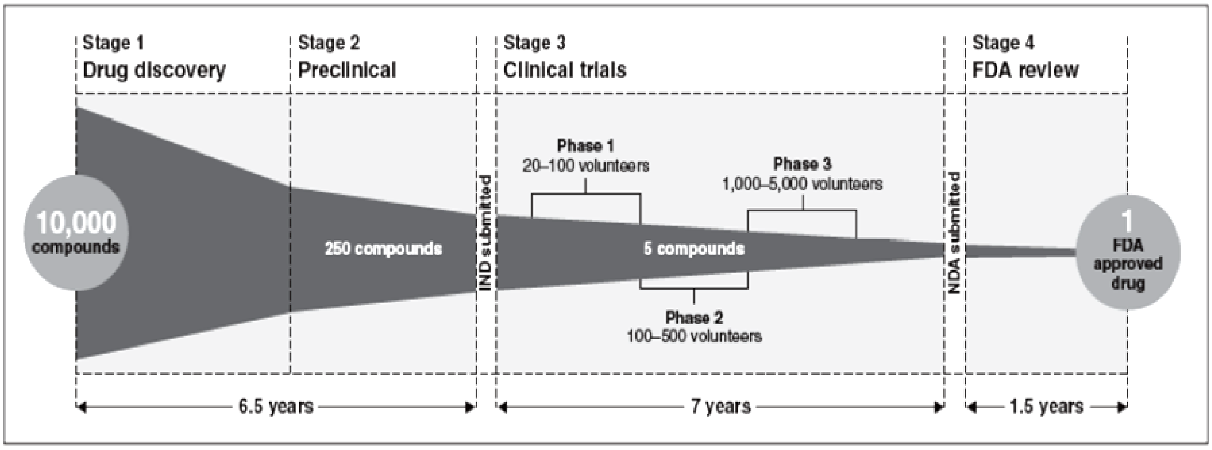

Fig. 1.4 The process of discovery to commericialization of an antibiotic [8].

Out of 10,000 compounds discovered with potential bacteriacidal activities, only one compound reaches market. The process of discovery to commericialization is very lengthy and slow. It takes almost 15 years time span and involves more than 5000 voluneteers with a total expense of 20 million USD. Fighting multidrug reisistance by discovery of new antibiotics is not a viable approach. An alternative needs to be realized, which involves non-traditional antibiotics that can overcome the limitations of narrow targeting antibiotics.

1.9 Nanomaterials: An Alternate to Antibiotics

Coinage materials like Cu, Ag, Zn, Au, etc. are known for their disinfectant properties since ancient times [15, 16]. Copper, silver and their salts are widely used to prevent infections in food and beverages during the Greek civilization. Discovery of vast variety of synthetic, semisynthetic and natural antibiotics have made antibacterial applications of these coinage metals and their compounds redundant during the 20th century [1]. In the last decade, the development of drug resistant strains and fast disappearance of antibiotics from the market due to decreased efficiency has brought the focus back on to these coinage metals [10]. It is well established fact that activity of a material increases as its size decreases, especially at nanoscale where the surface effects dominate the overall activity of the materials. Researches have studied the antimicrobial activities of nano-sized materials of these coinage metals and they have found impressive disinfectant properties in these nanostructures [17-20]. Bioactivities of nanostructured materials against multidrug resistant strains are also reported [21, 22]. Because of this, there is renewed interest in the antimicrobial activities of nanostructured materials especially of metals and metal oxide nanostructures of Ag, Cu, Au, Zn, Ti, etc. The inherent advantage, which these nanostructures carries with them is their non-toxicity towards healthy cells even at substantially higher concentration, which are at least ten times higher than their corresponding MIC values for pathogenic microorganisms.

1.10 Advantages of Nanomaterials as Antimicrobial Agents

In comparison with the traditional antibiotics, the nanomaterial based antibiotics carries certain distinct advantages. The minimum inhibitory concentration of nanomaterials is quite low as compared to traditional antibiotics [23]. Due to their small size, nanoparticles have high permeability across the cell walls and hence the effective concentration of nanoparticle based antibiotics would be very high at relatively lower doses [17-20]. Thus due to decrease in the MIC and higher permeability of nanostructures, the bactericidal concentrations required for clinical applications would be significantly lower than that required for conventional antibiotics. The mode of antibacterial action of nanomaterials is largely unclear. However, it is a well-established fact that nanomaterials interact with the pathogenic strains at random sites. Due to this, microorganisms are unlikely to acquire resistance against nano-antibiotics as they commonly do against narrow targeting traditional antibiotics [21, 22]. The broad and random targeting capabilities of nanomaterials make them the strong contender to fight against the multidrug resistant strains.

1.11 Possible Environmental Hazards of Nanomaterials

In a recent report on “Emerging Nanotechnologies” by Woodrow Wilson International Center, it is reported that more than 1600 nanomaterial based consumer products are currently in market [24]. Market share of nanotechnology based products is rapidly growing. The growth rate is as high as 379% in last ten years. By 2015, in US alone, nanomaterial business will be a trillion dollar industry [25]. Increasing use of nanostructures has raised concerns over their likely release into ecosystems. Nanoparticles leached from the consumer products are expected to enter into the terrestrial ecosystems [26, 27]. Environmental concentrations are currently unavailable for nanoparticles and potential environmental exposures are poorly constrained. Given the critical role of microbial communities in organic matter and nutrient recycling in ecosystems, environmental exposures of nanoparticles have potential to alter ecosystem productivity [28]. The environmental impacts of nanomaterials are largely unclear. Whether nanomaterials pose a threat to microbes essential for recycling in natural or engineered systems is an outstanding question of great relevance to ecosystem health and sustainable nanotechnology.

The goal of this thesis is to evaluate the bioactivity of as-synthesized metals (Ag and Cu) and metal oxide (TiO_2) nanostructures against clinically important pathogenic (*E. coli, S. aureus, P. vulgaris*) and eco-friendly strains (*B. subtilis and P. fluorescens*) that are playing vital role in bioremediation. In the next section, an overview of the state of the art of the subject is presented in terms of their nanoscale synthesis and their structure property correlation in terms of their bioactivities.

1.12 Review of Current State of Art

1.12.1 Silver Nanoparticles (SNPs)

Nanoparticles of noble metal silver have been brought to the forefront of nanoparticle research in recent years because of their unique optical, thermal and electrical properties [29-31]. Silver nanoparticles (SNPs) give strongest surface plasmon resonance in the visible region of the electromagnetic spectrum [32]. Use of SNPs as platform in surface enhance Raman spectroscopy (SERS) can increase the signal sensitivity by 10^5-10^8 [33]. Single molecular detection is now possible because of this enormous increase in sensitivity of SERS signal with SNPs [33]. They are also used as biosensors for quantitative analysis [34]. Colloidal silver is used as conducting ink in electronic printing of integrated circuits [35]. SNPs have diverse applications in medicine and health-care [36]. They display strong activity against all forms of microorganisms (bacteria, virus, algae and fungi) including the strains with multidrug resistance [37-40]. Owning to the highest antimicrobial activity (which is also comparable to the commercially available antibiotics) amongst all noble metals, SNPs are now extensively used as antimicrobial agent in wide range products like wound dressing [41], clothing [42], packing [43], home appliances [44], water purifiers [45], medical equipment [42], etc.

Performance of SNPs in these applications is largely governed by their particle size, size distribution, morphology, colloidal stability and surface chemistry. Size and size distribution of nanoparticles, their stability and properties are strongly influenced by the method of preparation and conditions of synthesis [46-66]. Various methods like thermal decomposition [46], microemulsion [47], sol-gel [48], polyol process [49], green synthesis [38], thermal, radiation and chemical reduction in the presence or absence of stabilizing agents [50-66], etc. have been attempted for the synthesis of SNPs.

Thermal decomposition has been widely used to make monodisperse SNPs. The precursors that have been employed include silver alkanoates [67, 68], silver acetate [69, 70], silver perfluorocarboxylates [71], silver oxalate [72], Ag(hfa)tetraglyme [73], silver nitrate [74], and silver carboxylates [75-77]. This method often requires high temperatures (120-250 °C), long reaction times (≈ 24 h), inert atmosphere or special chemicals such as a catalyst or toxic chemicals such as phenyl hydrazine [78]. Thermal decomposition sometimes involves complicated precursor synthesis; for example, synthesis of Ag(RCOO) from $AgNO_3$ and RCOOH [75]. In addition, nanoparticle yield is generally very low and process is very difficult to scale up. The surface of SNPs obtained by thermal decomposition method is hydrophobic and hence not suitable for medical applications where water dispersible nanostructures are essential.

SNPs prepared by microemulsion technique have smaller particle size, strict size distribution and high dispersion stability [79, 80]. In this method, size and shape of the SNPs can be controlled with ease by controlling the droplet size and shape [81]. Despite of high product quality, this technique is not much popular for the synthesis of SNPs. The major disadvantage of this technique is that it requires large amount of surfactant and organic solvents, which are difficult to remove from the final product. Nanoparticles' yield is generally low and impossible to scale up. SNPs prepared by microemulsion forms stable dispersion only at low concentrations [79, 80]. In many cases, they involved high concentrations of deleterious organic solvents. Hence, in applications where biocompatibility and dispersion stability at high concentration is critical, microemulsion is not a good choice for synthesizing SNPs.

Sol-gel technique is rarely implemented for the synthesis of SNPs [48]. This is because of the fact that nanoparticles obtained by this technique are relatively large. Further, it involves a second sintering step, which leads to the grain growth and generally polydisperse nanoparticles are obtained. The advantage of this method is its high yield. Surface functionalization of nanoparticles obtained by sol-gel technique is difficult. This method cannot be implemented when nanoparticle dispersion is required.

Polyol process is another solution-based synthesis route by which nearly monodisperse SNPs with desired morphologies can be prepared [49]. Synthesis of silver nanostructures with various anisotropic morphologies by varying the precursor concentration of the stabilizer and silver ions, reaction temperature and catalyst has been reported [82-84]. In these reports, the reaction conditions were harsh and difficult to control. Without fine control of reaction conditions and growth process, the obtained silver nanostructures have low yield with large by-products. The particle size is also relatively large and size control below 10 nm is difficult to achieve in polyol route of

SNPs synthesis. In many cases, they directly form water dispersible colloids, which are difficult to wash and purify before their use in biomedical applications.

Biosynthesis methods employing either microorganisms or plant extracts as reducing and size controlling agents have emerged as simple and viable alternative to chemical and physical synthesis procedures for SNPs [80, 85]. Particle size of SNPs prepared with green chemistry ranges from 50 to 80 nm with broad size distribution and multiple shapes. The major advantage of this technique is their ecofriendly procedure. However, the cost that one has to pay here is poor yield, large size and broad size distribution with poorly constrained particle morphology.

Amongst various synthesis routes reviewed here for SNPs preparation, chemical reduction method in the presence of stabilizing agents are the simplest and most popular because of the high quality of product they yield [61-66].There are few reports of SNPs preparation via thermal reduction route, which correlates the processing parameters with the nanostructure quality [50-53]. For example, Chen et al. [32] has proposed the reduction mechanism of $AgNO_3$ with oleylamine. In this article, they have studied the effect of growth temperature on the size and agglomeration of SNPs. Lin et al. [86] have prepared SNPs from reduction of silver trifluoroacetate with isoamyl ether. They have also evaluated the effect of precursor - surfactant molar ratio on the size of SNPs. Khan et al. [87] have made an attempt to study the effect of growth time on the formation of SNPs from the chemical reduction of silver nitrate by aniline in the presence of cetyltrimethylammonium bromide (CTAB). Nanoparticles produced by this method have size in the range of 10-30 nm with wide polydispersity. Premkumar et al. [88] have synthesized SNPs using β-cyclodextrin as reducing and capping agent under alkaline conditions at room temperature. They have reported that by altering the reaction temperature or reactant concentration, silver nanostructures of different shapes and sizes can be prepared.

From the literature survey, it has been found that the exact effect of reducing and capping agent and growth variables like nucleation temperature (N_T), nucleation time (N_t), growth temperature (G_T) and growth time (G_t) on the quantity (in terms of yield) and quality (in terms of size, polydispersity, morphology and agglomeration) of SNPs is not well understood. One of the objectives of this thesis is to establish the correlation between these growth variables on the quality and quantity of SNPs and also to optimize the synthesis protocols that yield water dispersible, biocompatible SNPs, which are usable for medical applications.

1.12.2 Copper Nanoparticles (CNPs)

Gold and silver nanoparticles owing to strong and tunable plasmonic characteristics [89, 90] are widely used in photocatalysis [91], single molecular detection via surface enhanced Raman scattering (SERS) [92], plasmonic photovoltaics [93], plasmonic solar cells [94], photothermal therapy [95] and imaging [96], etc. Despite of excellent plasmonic characteristics demonstrated by gold and silver, hunt for alternate plasmonic systems are on because of their high cost [97, 98].

Plasmonic nanostructures of copper could be an efficient and cost effective alternate to silver and gold nanostructures. The plasmonic characteristics of CNPs are not studied extensively [99, 100]. The major reason behind this is the stability of copper nanostructures against oxidation. Copper has low oxidation potential (0.34 eV) due to which it is highly prone to oxidation [101]. Plasmonic characteristics of metal can be observed only when size of the metal nanostructure is below its excitonic radius [102, 103]. The reactivity of metal particles increases with decrease in size, owing to high surface to volume ratio. Hence, CNPs are susceptible to oxidation in comparison to bulk copper [104-106]. Therefore, synthesis of ultra-small plasmonic CNPs that do not undergo oxidation is a challenge.

Various attempts have been made to synthesize colloidal plasmonic CNPs [107-111]. Most of them end up with products having multiple crystallographic phases (Cu, CuO and Cu_2O) [107-109]. Chen et al. [107] have attempted synthesis of CNPs in the presence of cetyltrimethylammonium bromide (CTAB) but could not get the pure Cu^0 phase. In 2011, Hashemipour et al. [108] have synthesized CNPs by electrochemical and chemical reduction methods. Large agglomerates of multi-phase CNPs were formed. In 2012, Usman et al. [109] have prepared CNPs using chitosan but the X-ray diffraction study shows the presence of copper oxide phase. Only few reports of single phase synthesis of metallic CNPs can be found in literature [110-114]. Most of them have relatively larger particle size (> 30 nm) and do not show plasmonic characteristics [110,111].

In 2012, Liu et al. [110] have synthesized CNPs in the presence of L-ascorbic acid at different pH, but in all cases the particle size is around 150 nm. In 2013, Yang et al. [111] have synthesized CNPs capped by alkanethiols with different carbon chain lengths in a two-phase system in the presence of stabilizer CTAB and reducing agent hydrazine hydrate. They have reported the effect of change in the ratio of surfactant to precursor on the size of nanoparticles. The synthesized product was non-uniform and particle size was large (≈ 40 nm). Hirai et al [115] have reported preparation of colloidal dispersion of CNPs. They have concluded that the first step in the formation of CNPs is the formation of a complex between Cu^{2+} and polymers. Cu^{2+} in this complex further reduces to Cu^0, whose subsequent growth leads to the formation of CNPs.

Nishimura et al. [116] have reported formation mechanism of CNPs by using in-situ time resolved XAFS analysis. They have concluded that formation of intermediates like $Cu(OH)_2$ and Cu^+ - PVP are playing critical role in the formation of CNPs. They have also concluded that PVP not only acts as capping agent but it also controls the reaction kinetics of CNPs formation. Haas et al. [117] have reported sonoelectrochemical synthesis of CNPs which are stabilized by PVP. They have expressed that formation of coordinative bonding between Cu^{2+} and PVP is essential before the reduction of Cu^{2+}. Yu et al. [118] have reported synthesis of monodispersed colloidal CNPs dispersed in polar solvents. They have demonstrated that PVP controls the nucleation of CNPs by controlling the aggregation between Cu ions and forming coordinated bonds between Cu^{2+} and PVP through oxygen and nitrogen polar groups present in the PVP skeleton.

For medical applications, CNPs has to be water dispersible. But water dispersible CNPs are prone to oxidation and aggregation. Hence, preparation of ultra-small colloidal dispersion of single phase metallic copper (Cu^0) nanoparticles which are stable in ambient conditions is a challenging task. In this thesis, we have attempted synthesis of aqueous colloidal dispersion of ultra-small single phase metallic CNPs, which are stable against both the oxidation and the aggregation. This study also explored the reduction mechanism of Cu^{2+}, formation of CNPs and their subsequent stabilization.

1.12.3 Titanium dioxide Nanoparticles (TNPs)

In 1972, Fujishima and Honda have reported photocatalytic activities of TiO_2, since then TiO_2 is widely used as catalyst in many industrial processes [119, 120]. In recent years antimicrobial properties of TNPs are gaining importance because of their broad spectrum of activities against microorganisms [121, 122]. In TNPs, the biocidal action is a result of the modulation of charge carriers upon photo excitation. The efficiency of this process is limited at present due to its poor photo excitation under visible radiation [123]. TiO_2 is a wide band-gap n-type semiconductor, which crystallizes into three polymorphic crystallographic phases, viz. anatase, rutile and brookite. Out of the three polymorphs of TiO_2, anatase is known to be catalytically more active. However, its large band gap (3.2 eV) and high rate of electron-hole recombination limits its efficiency only up to UV region [124, 125] Since the fraction of UV in the solar spectrum is less than 5%, TiO_2 cannot efficiently exploit the abundant natural resource, i.e. solar radiations, which dominantly consist of visible light. Hence, development of solar light active photocatalytic TNPs is a subject of extensive research.

Different strategies have been attempted to improve visible light response of TNPs by doping them with transition metals [126, 127], metal ions [128, 129], nonmetals [130, 131] and organic compounds [132, 133]. Doping TNPs with transition metals [134, 135] or non-metals such as Nitrogen [136], Boron [137] and Sulphur [138] is known to enhance their response in the visible light region. Few reports available in the literature also accounts for the improvement in the efficiency of TNPs towards visible light when doped with lanthanide ions/oxides [139]. In most of these studies, the visible response of TiO_2 improves upon doping but this does not necessarily increases the photocatalytic activity. This is mainly because of poor tunability of energy band gap, which may not extend the absorption edge deep into the visible region of the solar spectrum. In addition, when the doping concentration exceeds a desire level, the recombination effects dominate the visible absorption that adversely affect the photocatalytic response of TNPs [140].

Zhao et al. [141] have reported synthesis of bicrystalline TNPs with controlled anatase-brookite phase content. Results show that bicrystalline anatase-brookite is more active than single phase anatase, brookite and P25. The bicrystalline mixture with a composition of 75% anatase and 25% brookite shows the highest photocatalytic activity, which is likely due to the enhanced interfacial charge transfer between anatase and brookite nanocrystals. However, the optical response of this bicrytalline TNPs still lies in the ultraviolet region.

In the present work, an attempt has been made to synthesize visible light responsive cobalt doped anatase TNPs. Both pristine and cobalt doped TNPs were synthesized by hydrolysis and condensation of titanium isopropoxide. The objective of the study is to achieve tunable optical band gap (from ultraviolet region to deep into the visible region) by varying Co doping in the TNPs. Visible light responsive TNPs are expected to be a better bioremediation agents. Their catalytic properties under white light conditions are expected to be better than pristine TNPs whose optical response lies in the ultraviolet region.

1.13 Antimicrobial Activities of Metals and Metal Oxide Nanoparticles

Infectious diseases continue to be one of the greatest health challenges worldwide. Antibiotic resistance in microbes is becoming increasing important in public health care due to recent breakouts of microbial strains that are resistant to more than one anti-infective drug [1, 2]. WHO’s 2014 report on global surveillance of antimicrobial resistance reveals that antibiotic resistance is putting at risk the ability to treat common infections in hospitals. The world is heading towards a post-antibiotic era, in which common infections and minor injuries, which are otherwise treatable for decades, can once again kill [142]. The death rate of patients with serious infections caused by common bacteria in hospitals can be twice that of patients with infections caused by the same non-resistant bacteria. For example, patients infected with methicillin-resistant *Staphylococcus* (MRSA) are estimated to be 64% more likely to die than patients with a non-resistant form of the infection in hospitals [142].

Limited options are available with pharmacologist to tackle the threats posed by rapidly growing community of multi-drug resistant strains, which are converting common infections like diarrhea, pneumonia and urinary tract infection into deadly and life threatening conditions [3]. Antibiotics are fast disappearing from the market as they are losing sensitivity on microbes, which are developing resistance by mutations [12, 13]. Excessive and uncontrolled use of antibiotics both in preventive and curative healthcare across the globe has even worsen the situation, as microbes, which have never been exposed to a particular antibiotic drug are acquiring resistance towards that drug due to transfer of gene coding [4]. Hence, fighting multidrug resistance with traditional antibiotics is getting tougher and need is being felt for the development of non-traditional antibiotics against which microbes are unlikely to acquire resistance [143-145].

Coin-age metals like silver, copper and gold are known for their disinfectant properties since ancient time [143-145]. They were widely used in primordial medicines to treat wounds and prevent infections in food and brewages [145]. Nanostructured materials of these coin-age metals have better antibiotic properties compare to their bulk counter parts owing to their enhanced surface dominated reactivity [146, 147]. Although the mechanism of antimicrobial action of nanomaterials is largely unclear, it is a well-established fact that microbes are unlikely to develop resistant against metal nanostructures as they commonly do against conventional narrow targeting antibiotics because of their broad and random targeting capabilities [148].

Silver is known to have the highest antimicrobial activities amongst all metals and non-metals [149]. Silver ions and silver based compounds are highly toxic to microorganisms but have low toxicity to humans [37-40]. Existing literature on the antimicrobial characteristics of nanostructures of coin-age metals reveals that silver despite of its economic constraints remains to be the most popular antibiotic agent due to its highest biocidal activities [150, 151]. Irrespective of the nature and type of the microbes, SNPs show severe toxicity and this fact has made them most popular biocidal agent in the disinfection applications where traditional antibiotics cannot be useful [150, 151]. In recent time, the antibacterial activity of silver has gained profound importance due to increasing bacterial resistance to antibiotics.

Antimicrobial action of silver is different from antibiotics [152]. Antibiotics target specific sites on or within a bacterial cell and hence have narrow spectrum of activities while silver target multiple sites on or within a bacterial cell and hence have broad spectrum of activities [152]. Transfer of silver resistant genes from one piece to other is very weak [153,154], unstable and difficult to maintain [155, 156]. Hence, there are little chances of microbes developing resistance against silver as they do against narrow target antibiotics [157]. Interaction of SNPs with microorganism depends on the size, shape and surface properties [146, 147]. The antimicrobial properties of metals increase when their size is very small typically of the order of several nanometers [146, 147]. This is ascribed to large specific surface area of SNPs and enhanced activity due to the availability of more number of surface atoms.

Many researchers have studied the size dependent antibacterial activities of SNPs. Castanon et al. [37] have demonstrated that the antibacterial action of silver enhances when the size of nanoparticles is reduced. When the particle size of silver was reduced from 89 nm to 7 nm, their minimum inhibitory concentration (MIC) was decreased from 12 µg/mL to 6 µg/mL for *E. coli* and 34 µg/mL to 7 µg/mL for *S. aureus*. Gutierrez et al. [39] have shown strong antimicrobial action of silver against specific bacterial and fungal strains. They have observed MIC values as low as 0.4-1.7 µg/mL for bacterial and 3-25 µg/mL for fungal strains when treated with SNPs whose size lie between 20-25 nm. Veerasamy et al. [158] have studied antimicrobial activities of SNPs and correlated them with the antibacterial action of commercially available antibiotics such as Amikacin, Cefalotaxin, Penicillin and Sulpha Methoxazole. They have concluded that the silver demonstrate better antibacterial action as compared to these antibiotics when their size is reduced to 35 nm. In a recent article by Xiong et al., [147] an in-depth analysis of effect of physico-chemical properties of SNPs on their toxicity towards *Saccharomyces cerevisiae* yeast was carried out. They have concluded that particle size, surface chemistry, surface facets, stability and aging of sample have a great influence on the toxicity of SNPs. Despite the availability of large number of studies on the antimicrobial activities of SNPs against pathogenic strains, the effectiveness of SNPs against clinically important strains is always under shadow. Biocidal activities of SNPs are largely governed by the characteristics of SNPs which essentially depends on the synthesis protocols followed. Hence, correlating biocidal activities with the synthesis protocol is something which is essential and mostly missing from the literature.

Within the class of metal nanostructures, after silver, the next important nanoparticle system whose antimicrobial properties is of interest and has great potential is CNPs. The biocidal activities of CNPs are not much studied mainly because of their poor chemical resistance against oxidation in aqueous environment. Ruparelia et al. [159] have studied the antimicrobial activities of SNPs and CNPs against *E. coli*, *B. subtilis* and *S.*

aureus. *E. coli* and *S. aureus* show greater effectiveness to SNPs while CNPs are most active against *B. subtilis.* Yoon et al. [160] have studied the antimicrobial activity of CNPs by measuring the susceptibility constants of *E. coli* and *B. subtilis*. Highest susceptibility of CNPs against *B. subtilis* was observed. Cioffi et al. [161] have reported antimicrobial activities of silver and copper core-shell nanoparticles against *E. coli* and *Saccharomyces cerevisiae*. Results show that as-synthesized nanoparticles have greater inhibitory effect on the growth of these microorganisms. Song et al. [162] have investigated the toxicity of CNPs as a function of their particle size by exposing them to two mammalian and two piscine cell lines. The results reveal that toxicity of particles depends on morphologies, ion release and size of particles. CNPs in suspension contribute to the toxicity in all exposed cell lines while copper ions caused responses to mammalian cell lines only. Literature available on the biocidal activities of CNPs is insufficient and inconclusive. Hence, detailed investigation on the biocidal activities of ultra-small, water dispersible CNPs against clinically important strains especially the multi-drug resistant strains is essential.

TNPs are extensively used as photo-catalyst. Their photo catalytic activities are now commercially utilized in industrial environments for the pretreatment of toxic and harmful industrial waste. Owing to their high photo catalytic activities, it is expected that TNPs should display photo-induced biocidal activities. Fu et al. [163] have reported antimicrobial activities of TNPs on *E. coli* and *B. megaterium*. Good inhibition on *E. coli* and *B. megaterium* under day light was observed. They have ascribed the biocidal activities of TNPs to their small size, large band gap and catalytically active sites. Yuan et al. [164] have studied the biocidal activities of pristine and silver and nitrogen co-doped TNPs against *E. coli* and *B. subtilis*. They have concluded that Ag and N-doping improves the bio-catalytic activities of TNPs. In addition, they have also found synergistic effect of Ag-N co-doping on microbial properties of TNPs. Gupta et al. [165] have reported antibacterial activities of Ag-doped TNPs against *S. aureus, P. aeruginosa and E. coli*. They have concluded that Ag doping in the titania matrix and subsequent annealing improves its biocidal activities. Biocidal activities of TNPs are quite poor when compared with SNPs or CNPs. However, TNPs hold great potential to be a natural bioremediation photo catalytic agent if its photo response can be tuned into visible region.

SNPs are one of the most widely used engineered nanomaterials in nanotechnology based products [166]. They are now routinely incorporated into medical supplements, catheters, wound dressings and implants to inhibit the pathogen growth. SNPs are added to cosmetics as an antiseptic and used in medical textiles to eliminate the microbes in clinical environment [166]. They are also used for water purification, biosensors, bone prostheses, drug and gene delivery, bioimaging devices, etc. [167-169]. Majority of SNPs released from consumer products are expected to enter the terrestrial ecosystems through land-application of biosolids [26, 27]. While environmental concentrations are currently unavailable for SNPs and potential environmental exposures are poorly constrained, the increasing use of SNPs has raised concerns over their likely release into ecosystems. Given the critical role of microbial communities in organic matter and nutrient cycling in ecosystems, environmental exposures of SNPs have potential to alter ecosystem productivity [28]. Large number of studies has been conducted on clinical applications of SNPs [170-173], while its environmental impacts are largely unclear [174-180]. In addition, the antimicrobial properties of complexes of SNPs with conventional antibiotics that may form during their clinical usages are completely unknown. Whether SNPs pose a threat to microbes essential for recycling in natural or engineered systems is an outstanding question of great relevance to ecosystem health and sustainable nanotechnology.

This thesis makes an attempt to address the above concerns by evaluating the antimicrobial properties of as-synthesized silver, copper and titanium dioxide nanoparticles against clinically important and ecofriendly strains and correlate their biocidal activities with the characteristics of these nanoparticles. This thesis also makes an attempt to understand the synergistic effect of as-synthesized metal nanoparticles on the biocidal activities of conventional antibiotics.

References

1. G. Lancini, F. Parenti and G. G. Gallo, Antibiotics: A multidisciplinary Approach, 2nd Ed. Springer Science BV. (1993).
2. P. S. Brachman, International Journal of Epidemiology 32, 684-686 (2003).
3. A. P. Dobson and E. R. Carter, Bioscience 46, 115-126 (1996).
4. D. R. Hopkins, The Greatest Killer: Smallpox in History, The University of Chicago Press (2002).
5. H. Bynum, Spitting Blood: The history of Tuberculosis, Oxford University Press (2012).
6. D. M. Morens, J. K. Taubenberger and A. S. Fauci, Journal of Infectious Diseases 198, 962-970 (2008).
7. WHO Report on “Global Report for Research on Infectious Diseases of Poverty” (2012).
8. R. E. Reese, R. F. Betts and B. Gumustop, Handbook of Antibiotics, 3rd Ed. The Lippincott Williams & Wilkins (2000).
9. M. E. Florey, The Clinical Applications of Antibiotics: Penicillin, Oxford Medical Publications (1952).
10. O. Skold, Antibiotics and Antibiotic Resistance, John Wiley & Sons, Inc. (2011).
11. S. V. Kyriacou, W. J. Brownlow and X. H. Xu, Biochemistry 43, 140-147 (2004).
12. A. Panacek, L. Kvitek, R. Prucek, M. Kolar, R. Vecerova, N. Pizurova, V. K. Sharma, T. Nevecna and R. Zboril, The Journal of Physical Chemistry B 110, 16248-16253 (2006).
13. C. G. Smith and J. T. O’Donnell, The Process of New Drug Discovery and Development, 2nd Ed. CRC Press (2006).
14. L. Reichman and J. H. Tanne, Timebomb: The Global Epidemic of Multi-drug Resistant Tuberculosis, 1st Ed. McGraw-Hill (2003).
15. S. Prabhu and E. K. Poulose, International Nano Letters 2, 32-41 (2012).
16. H. H. A. Dollwet and J. R. J. Sorenson, Trace Elements in Medicine 2, 80-87 (1985).
17. C. Baker, A. Pradhan, L. Pakstis, P. J. Darrin and S. I. Shah, Journal of Nanoscience and Nanotechnology 5, 244-249 (2005).
18. S. Pal, Y. K. Tak and J. M. Song, Applied and Environmental Microbiology 73, 1712-1720 (2007).
19. M. Rai, A. Yadav and A. Gade, Biotechnology Advances 27, 76-83 (2009).
20. A. Azam, A. S. Ahmed, M. Oves, M. S. Khan, S. S. Habib and A. Memic, International Journal of Nanomedicine 7, 6003-6009 (2012).
21. S. Shrivastava, T. Bera, A. Roy, G. Singh, P. Ramachandrarao and D. Dash, Nanotechnology 18, 225103 (2007).
22. H. H. Lara, N. V. Ayala-Nunez, L. C. I. Turrent and C. R. Padilla, World Journal of Microbiology and Biotechnology 26, 615-621 (2010).
23. B. Chudasama, A. K. Vala, N. Andhariya, R. V. Upadhyay and R. V. Mehta, Nano Research 2, 955-965 (2009).
24. Woodrow Wilson International Center for Scholars. Nanotechnology Consumer Product Inventory; http://www.nanotechproject.org/inventories/consumer.
25. R. J. Aitken, M. Q. Chaudhry, A. B. A. Boxall and M. Hull, Occupational Medicine 56, 300-306 (2006).
26. S. A. Blaser, M. Scheringer, M. Macleod and K. Hungerbuhler, Science of the Total Environment 390, 396-409 (2008).

27. B. P. Colman, C. L. Arnaout, S. Anciaux, C. K. Gunsch, M. F. Hochella, B. Kim, G. V. Lowry, B. M. McGill, B. C. Reinsch, C. J. Richardson, J. M. Unrine, J. P. Wright, L. Yin and E. S. Bernhardt, PLoS ONE 8, e57189 (2013).
28. S. J. Klaine, P. J. Alvarez, G. E. Batley, T. F. Fernandes, R. D. Handy, D. Y. Lyon, S. Mahendra, M. J. McLaughlin and J. R. Lead, Environmental Toxicology and Chemistry 27, 1825-1851 (2008).
29. B. J. Wiley, Y. Chen, J. M. McLellan, Y. Xiong, Z. Y. Li, D. Ginger and Y. Xia, Nano Letters 7, 1032-1036 (2007).
30. K. S. Moon, H. Dong, R. Maric, S. Pothukuchi, A. Hunt, Y. Li and C. P. Wong, Journal of Electronic Materials 34, 168-175 (2005).
31. D. Chen, X. Qiao, X. Qiu and J. Chen, Journal of Materials Science 44, 1076-1081 (2009).
32. M. Chen, Y. G. Feng, X. Wang, T. C. Li, J. Y. Zhang and D. J. Qian, Langmuir 23, 5296-5304 (2007).
33. K. Kneipp, Y. Wang, H. Kneipp, L. T. Perelman, I. Itzkan, R. R. Dasari and M. S. Feld, Physical Review Letters 78, 1667-1670 (1997).
34. X. Ren, X. Meng, D. Chen, F. Tang and J. Jiao, Biosensors and Bioelectronics 21, 433-437 (2005).
35. A. Kamyshny, J. Steinke and S. Magdassi, The Open Applied Physics Journal 4, 19-36 (2011).
36. O. V. Salata, Journal of Nanobiotechnology 2, 1-6 (2004).
37. G. A. M. Castanon, N. N. Martinez, F. M. Gutierrez, J. R. M. Mendoza and F. J. Ruiz, Journal of Nanoparticle Research 10, 1343-1348 (2008).
38. S. Sadhasivam, P. Shanmugam and K. Yun, Colloids and Surfaces B: Biointerfaces 81, 358-362 (2010).
39. F. M. Gutierrez, P. L. Olive, A. Banuelos, E. Orrantia, N. Nino, E. M. Sanchez, F. Ruiz, H. Bach and Y. A. Gay, Nanomedicine: Nanotechnology, Biology and Medicine 6, 681-688 (2010).
40. E. Navarro, F. Piccapietra, B. Wagner, F. Marconi, R. Kaegi, N. Odzak, L. Sigg and R. Behra, Environmental Science & Technology 42, 8959-8964 (2008).
41. J. Tian, K. K. Y. Wong, C. M. Ho, C. N. Lok, W. Y. Yu, C. M. Che, J. F. Chiu and P. K. H. Tam., ChemMedChem 2, 129-136 (2007).
42. A. B. Lansdown, Current Problems in Dermatology 33, 17-34 (2006).
43. H. M. C. D. Azeredo, Food Research International 42, 1240-1253 (2009).
44. A. D. Maynard, R. J. Aitken, T. Butz, V. Colvin, K. Donaldson, G. Oberdorster, M. A. Philbert, J. Ryan, A. Seaton, V. Stone, S. S. Tinkle, L. Tran, N. J. Walker and D. B. Warheit, Nature 444, 267-269 (2006).
45. V. K. Sharma, R. A. Yngard and Y. Lin, Advances in Colloid and Interface Science 145, 83-96 (2009).
46. Z. J. Jiang, C. Y. Liu and L. W. Sun, The Journal of Physical Chemistry B 109, 1730-1735 (2005).
47. N. Toshima, T. Yonezawa and K. Kushihashi, Journal of the Chemical Society, Faraday Transactions 89, 2537-2543 (1993).
48. F. Mafune, J. Y. Kohnok, Y. Takeda and T. Kondow, The Journal of Physical Chemistry B 104, 8333-8337 (2000).
49. S. Coskun, B. Aksoy and H. E. Unalan, Crystal Growth & Design 11, 4963-4969 (2011).
50. Y. G. Sun, B. Mayers and Y. N. Xia, Nano Letters 3, 675-679 (2003).

51. K. Esumi, T. Tano, K. Torigoe and K. Meguru, Chemistry of Materials 2, 564-567 (1990).
52. L. M. L. Marzan and A. P. Philipse, The Journal of Physical Chemistry 99, 15120-15128 (1995).
53. P. Raveendran, J. Fu and S. L. Wallen, Journal of the American Chemical Society 125, 13940-13941 (2003).
54. H. H. Huang, X. P. Ni, G. L. Loy, C. H. Chew, K. L. Tan, F. C. Loh, F. C. Deng and G. Q. Xu, Langmuir 12, 909-912 (1996).
55. N. Yanagihara, Y. Tanaka and H. Okamotot, Chemistry Letters 8, 796-797 (2001).
56. A. Callegari, D. Tonti and M. Chergui, Nano Letters 3, 1565-1568 (2003).
57. F. Gao, Q. Y. Lu and S. Komarneni, Chemistry of Materials 17, 856-860 (2005).
58. Y. J. Xiong, Y. Xie, G. O. Du, X. M. Liu and X. B. Tian, Chemistry Letters 31, 98-99 (2002).
59. N. R. Jana and X. G. Peng, Journal of the American Chemical Society 125, 14280-14281 (2003).
60. A. Taleb, C. Petit and M. P. Pileni, Chemistry of Materials 9, 950-959 (1997).
61. Z. Q. Zhang, R. C. Patel, R. Kothari, C. P. Johnson, S. E. Friberg and P. A. Aikens, The Journal of Physical Chemistry B 104, 1176-1182 (2000).
62. A. Henglein and M. Giersig, The Journal of Physical Chemistry B 103, 9533-9539 (1999).
63. T. Saraidarov, V. Levchenko and R. Reisfeld, physica status solidi (c) 7, 2648-2651 (2010).
64. G. J. Lee, S. I. Shin, Y. C. Kim and S. G. Oh, Materials Chemistry and Physics 84, 197-204 (2004).
65. Y. G. Sun and Y. N. Xia, Science 298, 2176-2179 (2002).
66. Y. G. Sun, Y. D. Yin, B. T. Mayers, T. Herricks and Y. N. Xia, Chemistry of Materials 14, 4736-4745 (2002).
67. I. K. Shim, Y. I. Lee, K. J. Lee and J. Joung, Materials Chemistry and Physics 110, 316-321 (2008).
68. M. Yamamoto and M. Nakamoto, Journal of Materials Chemistry 13, 2064-2065 (2003).
69. H. Hiramatsu and F. E. Osterlok, Chemistry of Materials 16, 2509-2511 (2004).
70. K. J. Lee, B. H. Jun, J. Choi, Y. I. Lee, J. Joung and Y. S. Oh, Nanotechnology 18, 335601 (2007).
71. S. J. Lee, S. W. Han and K. Kim, Chemical Communications 442-443 (2002).
72. S. Navaladian, B. Viswanathan, R. P. Viswanath and T. K. Varadarajan, Nanoscale Research Letters 2, 44-48 (2007).
73. L. D'Urso, V. Nicolosi, G. Compagnini and O. Puglisi, Applied Surface Science 226, 131-136 (2004).
74. Z. Chen and L. Gao, Materials Research Bulletin 42, 1657-1661 (2007).
75. M. Yamamoto, Y. Kashiwagi and M. Nakamoto, Langmuir 22, 8581-8586 (2006).
76. Y. Kashiwagi, M. Yamamoto and M. Nakamoto, Journal of Colloid & Interface Science 300, 169-175 (2006).
77. N. Yang and K. Aoki, The Journal of Physical Chemistry B 109, 23911-23917 (2005).
78. Y. Li, Y. Wu and B. S. Ong, Journal of the American Chemical Society 127, 3266-3267 (2005).
79. C. Petit, P. Lixon and M. P. Pileni, The Journal of Physical Chemistry 97, 12974-12983 (1993).

80. Y. Xie, R. Ye and H. Liu, Colloids and Surfaces A: Physicochemical and Engineering Aspects 279, 175-178 (2006).
81. S. May and A. Ben-Shaul, The Journal of Physical Chemistry B 105, 630-640 (2001).
82. Y. Sun, B. Mayers, T. Herricks and Y. Xia, Nano Letters 3, 955-960 (2003).
83. D. Kim, S. Jeong and J. Moon, Nanotechnology 17, 4019-4024 (2006).
84. T. M. D. Dang, T. T. T. Le, E. F. Blanc and M. C. Dang, Advances in Natural Sciences: Nanoscience and Nanotechnology 3, 035004 (4pp) (2012).
85. C. Wu, B. P. Mosher and T. Zeng, Journal of Nanoparticle Research 8, 965-969 (2006).
86. X. Z. Lin, X. Teng and H. Yang, Langmuir 19, 10081-10085 (2003).
87. Z. Khan, S. A. Al-Thabaiti, A. Y. Obaid and A. O. Al-Youbi, Colloids and Surfaces B: Biointerfaces 82, 513-517 (2011).
88. T. Premkumar and K. E. Geckeler, New Journal of Chemistry 38, 2847-2855 (2014).
89. W. Lewandowski, D. Constantin, K. Walicka, D. Pociecha, J. Mieczkowski and E. Gorecka, Chemical Communications 49, 7845-7847 (2013).
90. M. A. Mahmoud and M. A. El-Sayed, The Journal of Physical Chemistry Letters 4, 1541-1545 (2013).
91. M. J. Kale, T. Avanesian and P. Christopher, ACS Catalysis 4, 116-128 (2014).
92. P. L. Stiles, J. A. Dieringer, N. C. Shah and R. P. V. Duyne, Annual Review of Analytical Chemistry 1, 601-626 (2008).
93. V. E. Ferry, J. N. Munday and H. A. Atwater, Advanced Materials 22, 4794-4808 (2010).
94. J. N. Munday and H. A. Atwater, Nano Letters 11, 2195-2201 (2011).
95. A. M. Alkilany, L. B. Thompson, S. P. Boulos, P. N. Sisco and C. J. Murphy, Advanced Drug Delivery Reviews 64, 190-199 (2012).
96. W. I. Choi, A. Sahu, Y. H. Kim and G. Tae, Annals of Biomedical Engineering 40, 534-546 (2012).
97. R. Becker, B. Liedberg and P. O. Kall, Journal of Colloid & Interface Science 343, 25-30 (2010).
98. Y. Shi, B. Sun, Z. Zhou, Y. T. Wu and M. F. Zhu, Progress in Natural Science: Materials International 21, 447-454 (2011).
99. G. H. Chan, J. Zhao, E. M. Hicks, G. C. Schatz and R. P. V. Duyne, Nano Letters 7, 1947-1952 (2007).
100. I. Kriegel, C. Jiang, J. R. Fernandez, R. D. Schaller, D. V. Talapin, E. D. Como and J. Feldmann, Journal of the American Chemical Society 134, 1583-1590 (2012).
101. S. Magdassi, M. Grouchko and A. Kamyshny, Materials 3, 4626-4638 (2010).
102. M. Hu, J. Chen, Z. Y. Li, L. Au, G. V. Hartland, X. Li, M. Marquez and Y. Xia, Chemical Society Reviews 35, 1084-1094 (2006).
103. S. W. Verbruggen, M. Keulemans, J. A. Martens and S. Lenaerts, The Journal of Physical Chemistry B 117, 19142-19145 (2013).
104. J. Zhang, J. Liu, Q. Peng, X. Wang and Y. Li, Chemistry of Materials 18, 867-871 (2006).
105. V. Vellora, T. Padil and M. Cernik, International Journal of Nanomedicine 8, 889-898 (2013).
106. A. Shuin, W. Zhu, L. Xu, D. Qin and Y. Wang, Ceramics International 39, 8715-8722 (2013).
107. H. Chen, J. H. Lee, Y. H. Kim, D. W. Shin, S. C. Park, X. Meng and J. B. Yoo, Journal of Nanoscience and Nanotechnology 10, 629-636 (2010).

108. H. Hashemipour, M. E. Zadeh, R. Pourakbari and P. Rahimi, International Journal of Physical Sciences 6, 4331-4336 (2011).
109. M. S. Usman, N. A. Ibrahim, K. Shameli, N. Zainuddin, W. M. W. Yunus, Molecules 17, 14928-14936 (2012).
110. Q. M. Liu, T. Yasunami, K. Kuruda and M. Okido, Transactions of Nonferrous Metals Society of China 22, 2198-2203 (2012).
111. G. Yang, Z. Zhang, S. Zhang, L. Yu, P. Zhang and Y. Hou, Surface and Interface Analysis 45, 1695-1701 (2013).
112. J. L. C. Huaman, K. Sato, S. Kurita, T. Matsumoto and B. Jeyadevan, Journal of Materials Chemistry 21, 7062-7069 (2011).
113. L. Q. Ming, Z. De-bi, Y. Yamamoto, R. Ichino and M. Okido, Transactions of Nonferrous Metals Society of China 22, 117-123 (2012).
114. J. Xiong, Y. Wang, Q. Xue and X. Wu, Green Chemistry 13, 900-904 (2011).
115. H. Hirai, H. Wakabayashi and M. Komiyama, Bulletin of the Chemical Society of Japan 59, 367-372 (1986).
116. S. Nishimura, A. Takagaki, S. Maenosono and K. Ebitani, Langmuir 26, 4473-4479 (2010).
117. I. Haas, S. Shanmugam and A. Gedanken, The Journal of Physical Chemistry B 110, 16947-16952 (2006).
118. W. Yu, H. Xie, L. Chen, Y. Li and C. Zhang, Nanoscale Research Letters 4, 465-470 (2009).
119. A. Fujishima and K. Honda, Nature 238, 37-38 (1972).
120. M. Iwasaki, M. Hara, H. Kawada, H. Tada and S. Ito, Journal of Colloid and Interface Science 224, 202-204 (2000).
121. J. Wiener, J. P. Quinn, P. A. Bradford, R. V. Goering, C. Nathan, K. Bush and R. A. Weinstein, The Journal of the American Medical Association 281, 517-523 (1999).
122. S. Josset, N. Keller, M. C. Lett, M. J. Ledoux and V. Keller, Chemical Society Reviews 37, 744-755 (2008).
123. T. S. Wu, K. X. Wang, G. D. Li, S. Y. Sun, J. Sun and J. S. Chen, Applied Materials and Interfaces 2, 544-550 (2010).
124. R. K. Wahi, W. W. Yu, Y. Liu, M. L. Mejia, J. C. Falkner, W. Nolte and V. L. Colvin, Journal of Molecular Catalysis A: Chemical 242, 48-56 (2005).
125. H. Tada and M. Tanaka, Langmuir 13, 360-364 (1997).
126. T. Umebayashi, T. Yamaki, H. Itoh and K. Asai, Journal of Physics and Chemistry of Solids 63, 1909-1920 (2002).
127. B. Liu, H. M. Chen, C. Liu, S. C. Andrews, C. Hahn and P. Yang, Journal of the American Chemical Society 135, 9995-9998 (2013).
128. W. Choi, A. Termin and M. R. Hoffmann, The Journal of Physical Chemistry 98, 13669-13679 (1994).
129. P. C. Ricci, C. M. Carbonaro, A. G. Lehmann, F. Congiu, B. Puxeddu, G. Cappelletti and F. Spadavecchia, Journal of Alloys and Compounds 561, 109-113 (2013).
130. J. Dua, G. Zhao, Y. Shi, H. Yang, Y. Li and G. Zhu, Applied Surface Science 273, 278-286 (2013).
131. L. Zhang, M. S. Tse, O. K. Tan, Y. X. Wang and M. Han, Journal of Material Chemistry A 1, 4497-4507 (2013).
132. A. Biswas, A. Corani, A. Kathiravan, Y. Infahsaeng, A. Yartsev, V. Sundstrom and S. De, Nanotechnology 24, 195601 (2013).
133. M. Radoicic, Z. Saponjic, I. A. Jankovic, G. Ciric -Marjanovic, S. P. Ahrenkiel and M. I. Comor, Applied Catalysis B: Environmental 136-137, 133-139 (2013).

134. H. Kato and A. Kudo, The Journal of Physical Chemistry B 106, 5029-5034 (2002).
135. J. G. Yu, J. C. Yu, B. Cheng and X. J. Zhao, Journal of Sol-Gel Science and Technology 24, 39-48 (2002).
136. J. L.Gole, J. D. Stout, C. Burda, Y. Lou and X. Chen, The Journal of Physical Chemistry B 108, 1230-1240 (2004).
137. N. S. Begum, H. M. F. Ahemad and O. M. Hussain, Bulletin of Materials Science 31, 741-745 (2008).
138. E. M. Rockafellow, L. K. Stewart and W. S. Jenks, Applied Catalysis B: Environmental 91, 554-562 (2009).
139. K. M. Parida and N. Sahu, Journal of Molecular Catalysis A: Chemical 287, 151-158 (2009).
140. U. G. Akpan and B. H. Hameed, Applied Catalysis A: General 375, 1-11 (2010).
141. H. Zhao, L. Liu, J. M. Andino and Y. Li, Journal of Materials Chemistry A 1, 8209-8216 (2013).
142. WHO Report on “Antimicrobial resistance: global report on surveillance” (2014).
143. K. Kon and M. Rai, Journal of Comparative Clinical Pathology Research 2, 160-174 (2013).
144. A. M. Allahverdiyev, E. S. Abamor, M. Bagirova and M. Rafailovich, Future Microbiology 6, 933-940 (2011).
145. J. A. Lemire, J. J. Harrison and R. J. Turner, Nature Reviews Microbiology 11, 371-384 (2013).
146. K. Shameli, M. B. Ahmad, M. Zargar, W. M. Z. W. Yunus, A. Rustaiyan and N. A. Ibrahim, International Journal of Nanomedicine 6, 581-590 (2011).
147. Y. Xiong, M. Brunson, J. Huh, A. Huang, A. Coster, K. Wendt, J. Fay and D. Qin, Small 9, 2628-2638 (2013).
148. C. Khurana, A. K. Vala, N. Andhariya, O. P. Pandey and B. Chudasama, Environmental Science: Processes & Impacts 16, 2191-2198 (2014).
149. W. R. Li, X. B. Xie, Q. S. Shi, H. Y. Zeng, Y. S. O. Yang and Y. B. Chen, Applied Micrbiology and Biotechnology 85, 1115-1122 (2010).
150. B. Chudasama, A. K. Vala, N. Andhariya, R. V. Upadhyay and R. V. Mehta, Journal of Nanoparticle Research 12, 1677-1685 (2010).
151. C. Khurana, A. K. Vala, N. Andhariya, O. P. Pandey and B. Chudasama, Journal of Biomedical Materials Research Part A (2013) doi: 10.1002/jbm.a.35005.
152. S. L. Percival, P. G. Bowler and D. Russell, Journal of Hospital Infection 60, 1-7 (2005).
153. G. L. McHugh, R. C. Moellering, C. C. Hopkins and M. N. Swartz, The Lancet 305, 235-240 (1975).
154. D. I. Annear, N. J. Mee and M. Bailey, Journal of Clinical Pathology 29,441-443 (1976).
155. A. T. Hendry and I. O. Stewart, Canadian Journal of Microbiology 25, 916-921 (1979).
156. L. M. Deshpande and B. A. Chopade, Biometals 7, 49-56 (1994).
157. A. Gupta, K. Matsui, J. F. Lo and S. Silver, Nature Medicine 5,183-188 (1999).
158. R. Veerasamy, T. Z. Xin, S. Gunasagaran, T. F. W. Xiang, E. F. C. Yang, N. Jeyakumar and S. A. Dhanaraj, Journal of Saudi Chemical Society 15, 113-120 (2011).
159. J. P. Ruparelia, A. K. Chatterjee, S. P. Duttagupta and S. Mukherji, Acta Biomaterialia 4, 707-716 (2008).

160. K. Y. Yoon, J. H. Byeon, J. H. Park and J. Hwang, Science of the Total Environment 373, 572-575 (2007).
161. N. Cioffi, N. Ditaranto, L. Torsi, R. A. Picca, E. D. Giglio, L. Sabbatini, L. Novello, G. Tantillo, T. Bleve-Zacheo and P. G. Zambonin, Analytical and Bioanalytical Chemistry 382, 1912-1918 (2005).
162. L. Song, M. Connolly, M. L. Fernandez-Cruz, M. G. Vijver, M. Fernandez, E. Conde, G. R. Snoo, W. J. G. M. Peijnenburg and J. M. Navas, Nanotoxicology 8, 383-393 (2014).
163. G. Fu, P. S. Vary and C. T. Lin, The Journal of Physical Chemistry B 109, 8889-8898 (2005).
164. Y. Yuan, J. Ding, J. Xu, J. Deng and J. Guo, Journal of Nanoscience and Nanotechnology 10, 4868-4874 (2010).
165. K. Gupta, R. P. Singh, A. Pandey and A. Pandey, Beilstein Journal of Nanotechnology 4, 345-351 (2013).
166. M. Ahamed, M. S. AlSalhi and M. K. J. Siddiqui, Clinica Chimica Acta 411, 1841-1848 (2010).
167. T. M. Tolaymat, A. M. El Badawy, A. Genaidy, K. G. Scheckel, T. P. Luxton and M. Suidan, Science of the Total Environment 408, 999-1006 (2010).
168. A. K. Karumuri, D. P. Oswal, H. A. Hostetler and S. M. Mukhopadhyay, Materials Letters 109, 83-87 (2013).
169. A. M. Schrand, L. K. Braydich-Stolle, J. J. Schlager, L. M. Dai and S. M. Hussain, Nanotechnology 19, 235104 (2008).
170. A. R. Shahverdi, A. Fakhimi, H. R. Shahverdi and S. Minaian, Nanomedicine: Nanotechnology, Biology, and Medicine 3, 168-171 (2005).
171. J. R. Morones, J. L. Elechiguerra, A. Camacho, K. Holt, J. B. Kouri, J. T. Ramirez and M. J. Yacaman, Nanotechnology 16, 2346-2353 (2005).
172. P. V. Dong, C. H. Ha, L. T. Binh and J. Kasboham, International Nano Letters 2, 9-17 (2012).
173. F. Okafor, A. Janen, T. Kukhtareva, V. Edwards and M. Curley, International Journal of Environmental Research and Public Health 10, 5221-5238 (2013).
174. B. P. Colman, S. Y. Wang, M. Auffan, M. R. Wiesner and E. S. Bernhardt, Ecotoxicology 21, 1867-1877 (2012).
175. C. Levard, E. M. Hotze, G. V. Lowry and G. E. Brown, Environmental Science & Technology 46, 6900-6914 (2012).
176. A. J. Bone, B. P. Colman, A. P. Gondikas, K. M. Newton, K. H. Harrold, R. M. Cory, J. M. Unrine, S. J. Klaine, C. W. Matson and R. T. Di Giulio, Environmental Science & Technology 46, 6925-6933 (2012).
177. A. Gitipour, A. E. Badawy, M. Arambewela, B. Miller, K. Scheckel, M. Elk, H. Ryu, V. G. Alvarez, J. S. Domingo, S. Thiel and T. Tolaymat, Environmental Science & Technology 47, 14385-14393 (2013).
178. L. M. Stevenson, H. Dickson, T. Klanjscek, A. A. Keller, E. McCauley and R. M. Nisbet, PLoS ONE 8, e74456 (2013).
179. B. Reidy, A. Haase, A. Luch, K. A. Dawson and I. Lynch, Materials 6, 2295-2350 (2013).
180. S. J. Yu, Y. G. Yin and J. F. Liu, Environmental Science: Processes & Impacts 15, 78-92 (2013).

CHAPTER 2

EXPERIMENTAL TECHNIQUES

2.1 Introduction

Utility of nanoparticles in a particular application is largely governed by their size, size distribution and morphology. At bulk scale, the properties of matter do not influence much by their particle size, size distribution and morphology [1]. In contrast to this, at nanoscale, materials exhibit drastically different size dependent electronic, thermal, mechanical and biological properties in reference to their bulk counterparts [2]. At nanoscale, properties of materials dramatically vary with their size, size distribution and morphology [3]. These parameters of nanostructures are mainly dependent on the method of synthesis and protocols followed there in. Very small size of nanoparticles causes complications in their characterizations. Therefore, the challenge lies in finding the right characterization techniques that have the optimum capabilities for studying the characteristics of materials at nanometer scale. In this chapter details of various experimental and characterization techniques used throughout this study are provided. Explanation includes purpose of the specific study, technical details of analytical tool/instrument used, sample preparation requirements for each measurement and exact experimental conditions / parameters of measurements.

2.2 X-ray Diffraction

Material’s properties are strongly influenced by their crystallographic structure. Hence, the crystal structure of the nanomaterials needs to be investigated first. X-ray diffraction (XRD) is generally used to study the crystal structure of fine powdered samples. It is used for the phase identification of a crystalline material. It also provides information on unit cell dimensions, lattice strain and crystallite size [4]. This technique is based on the principle of constructive interference of radiation.

In the present study, X-ray diffraction experiments were performed on PANalyticalX’Pert Pro diffractometer operated at 45 kV and 40 mA in the 2θ range of 20° to 80°. It uses a monochromatic beam of X-rays having CuK_α radiation of 1.5406 Å with Ni filter. The scan speed of the detector was 0.0139° per second. All X-ray diffraction were performed at room temperature. The fine powder of nanoparticles was densely packed on a cavity type sample holder. The sample surface was large enough to ensure that the incident beam impinges over the sample in the full angular range and thick enough to ensure that the whole incident X-ray beam interacts with the sample and does not pass through. The phase identification was performed on X'Pert High Score Plus by comparing the X-ray diffraction pattern of materials under investigation with the standard library of Joint Committee on Powder Diffraction Standards (JCPDS). The crystallographic parameters were determined from the refined X-ray diffraction pattern. The Rietveld refinement was performed on Fullprof suite program.

2.2.1 Rietveld Refinement

In Rietveld method, XRD patterns decompose by using Pawley and/or Le Bail algorithms [5]. Rietveld refinement employs the nonlinear least squares method, which requires a reasonable initial approximation of many free variables. These usually include peak-shape parameters, unit cell dimensions and coordinates of all atoms in the model of the crystal structure. Other unknowns e.g., constant background, scale factor, overall atomic displacement parameter, etc. may be simply guessed at the beginning and then effectively refined as the least squares fit converges to a global minimum. Rietveld refinement uses a least square approach to refine a theoretical line profile until it matches the measured profile. The minimized function, Φ, is therefore, given by:

$$\Phi = \sum_{i=1}^{n} W_i \left\{Y_i^{obs} - Y_i^{calc}\right\}^2 \tag{2.1}$$

where W_i is the weight assigned to the i^{th} data point.

In Rietveld refinement, both the pattern *i.e.* Y_i^{obs} and Y_i^{calc} are plotted in same window, to see the difference between them. For good fitting, both pattern should overlap completely i.e. $Y_i^{obs} - Y_i^{calc} = 0$. Visual examination of the difference usually provides important clues about which additional parameter(s) must be refined. The following numerical factors are normally used to characterize Rietveld refinement quality. The profile residual (or reliability) factor, Rp:

$$R_p = \frac{\sum_{i=1}^{n} \left|Y_i^{obs} - Y_i^{calc}\right|}{\sum_{i=1}^{n} Y_i^{obs}} \times 100\% \tag{2.2}$$

The weighted profile residual, R_{wp}:

$$R_{wp} = \left[\frac{\sum_{i=1}^{n} W_i\left\{Y_i^{obs} - Y_i^{calc}\right\}^2}{\sum_{i=1}^{n} W_i\left(Y_i^{obs}\right)^2}\right]^{1/2} \times 100\% \tag{2.3}$$

The expected profile residual, R_{exp}:

$$R_{exp} = \left[\frac{n - p}{\sum_{i=1}^{n} W_i\left(Y_i^{obs}\right)^2}\right]^2 \times 100\% \tag{2.4}$$

where p is the number of free least squares parameters.

And the goodness of fit, χ^2:

$$\chi^2 = \frac{\sum_{i=1}^{n} W_i\left\{Y_i^{obs} - Y_i^{calc}\right\}^2}{n - p} = \left[\frac{R_{wp}}{R_{exp}}\right]^2 \tag{2.5}$$

For the best fitted data, χ^2 should be minimum.

2.2.2 Determination of Crystallite Size and lattice strain by Williamson-Hall analysis

The width of an X-ray diffraction peak depends on [4]

a. Instrumental factors
b. lattice strain and
c. the size of the crystallites

It is possible to separate the effects of size and strain on the broadening of an X-ray diffraction peak. Strain broadening increases with increasing θ, when size broadening is independent of θ. Generally both the size and the strain broadenings are present in X-ray diffractograms. They are related by the Williamson-Hall expression:

$$\beta\cos\theta = \frac{k\lambda}{t} + \eta\sin\theta \tag{2.6}$$

Here β is experimentally observed integral breadth of X-ray diffraction peak, θ is diffraction angle, λ is the wavelength of X-ray source, t is crystallite size, η is lattice strain and k is geometrical constant. For nanoparticles, it is equal 0.9. By plotting βcosθ vs sinθ, the crystallite size and lattice strain can be obtained.

2.3 Thermal Analysis

In order to evaluate thermal stability and temperature induced structural transitions in nanoparticles, thermogravimetry (TG) and differential scanning calorimetry (DSC) techniques have been used in the current study. Thermogravimetric analysis (TGA) is a thermodynamic technique, in which the change in the weight of sample as a function of temperature in a preselected environment is measured. It works on the principle that heat flow into a substance induces physical and chemical changes, which can help in identifying and characterizing the identity of the substance [6]. This technique is quite useful in evaluating the thermal stability and reaction kinetics under various atmospheric conditions.

In the present study, TGA analysis was carried out on Netzsch STA449 F3 Jupiter simultaneous thermal analyzer. All measurements were carried out in alumina pan without any preheating. An identical empty alumina pan was used as reference pan. Before each measurement, the instrument was kept in ideal mode overnight to stabilize the thermo-balance. Powder sample (few mg) was weighed with the help of microbalance just prior to the beginning of thermal cycle. Thermograms were recorded from 25 °C - 1000 °C at a heating rate of 5 °C/min in N_2 atmosphere. The flow rate of inert gas was controlled by mass flow controller. The flow was maintained at 50 mL/min for sample chamber (purge gas) and 20 mL/min for balance chamber (protective gas). The results were analyzed on Netzsch Proteus 6.1 thermal analysis software.

Differential scanning calorimetry (DSC) is another thermodynamic approach where isothermal differential power of sample and reference is measured with temperature [6]. In DSC, temperatures of both sample and reference are kept equal throughout the analysis and it is expected that the reference sample (empty pan) has a distinct heat capacity over the temperature range at which scanning is to be carried out. In the present study, DSC is used to determine structural phase transitions (amorphous → crystallization) of nanoparticles. DSC thermograms of nanoparticles were recorded on Netzsch STA449 F3 Jupiter simultaneous thermal analyzer under identical experimental conditions as mentioned for TG measurements. Obtained results were analyzed on Netzsch Proteus 6.1 thermal analysis software and crystallization temperatures were determined for samples under investigation.

2.4 UV-visible Spectroscopy

To investigate the optical response of as-synthesized nanoparticles, samples were subjected to UV-visible (UV-Vis) spectroscopy. The UV-Visible spectra of colloidal dispersion of nanoparticles were recorded in the absorption mode while powder samples were investigated in the reflection mode by diffusion reflectance spectroscopy [7]. A quartz cuvette is used to prepare colloidal sample for UV-visible spectroscopy as it is transparent to UV and visible radiations. A colloidal nanoparticle dispersion was poured into quartz cuvette and its UV-visible spectrum was recorded on Hitachi U-3900H double beam spectrophotometer. The spectrometer is capable of recording optical response of the sample in the 190-900 nm spectral range. All the measurements were performed at 25 °C. Colloidal samples were diluted as and when required prior to measurement. Diffuse reflections of powdered samples were also measured on Hitachi U-3900H spectrometer equipped with 60° integrating sphere accessory and powder sample holder. The baseline correction of Barium Sulphate pallets was employed before reflectance measurement. The optical energy band gap of the nanoparticles was determined by analysing the reflectance spectra with the Kubelka-Munk function [8]

$$F(R) = (100\text{-}R)^2/200R \tag{2.7}$$

where R is the (%) reflectance of the sample and F(R) is the corresponding absorbance.

2.5 Photon Correlation Spectroscopy

Photon correlation spectroscopy (PCS) also known as dynamic light scattering (DLS) or elastic light scattering is a widely used experimental technical to determine the hydrodynamic size of nanoparticles in their colloidal state [9]. The method is based on the determination of the diffusion coefficient of the nanoparticles in their colloidal state by means of studying the intensity fluctuations due to the Brownian motion of the nanoparticles. These intensity fluctuations yield an autocorrelation function, which is linked to the diffusion coefficient of the nanoparticles. By using Stokes-Einstein relation [9], the hydrodynamic diameter of the nanoparticles can be determined. In the present study, the hydrodynamic sizes of as-synthesized nanoparticles were determined on Brookhaven 90 plus particle size analyser. The particle size analyser is equipped with DPSS laser with emission wavelength of 658 nm. The scattering angle was fixed at 90°.

All measurements were carried out at 25 °C by using Peltier controlled thermostat. For the measurement, colloidal sample of nanoparticles was placed in a glass cuvette. The colloidal dispersion was adequately diluted before measurement. The volume fraction of nanoparticles in suspension was < 10 %. The measured autocorrelation function is analysed on MAS OPTION software by fitting the data in a lognormal particle size distribution function [10]. From the best fit, the hydrodynamic size and polydispersity of the nanoparticles were determined.

2.6 Fourier Transform Infrared Spectroscopy

Fourier Transform Infrared Spectroscopy (FTIR) is an effective analytical technique for detecting the functional groups and characterizing covalent bonds in the sample. When exposed to infrared radiation, sample molecules selectively absorb radiation of specific wavelengths which causes the change in the dipole moment of the molecules. Consequently, the vibrational energy levels of molecules transfer from ground state to the excited state. Functional groups attached to the surface of metal nanoparticles show different FTIR pattern than those of free groups; hence FTIR gives information about the surface chemistry of nanomaterials [11]. In the present study, FTIR spectroscopy was employed to study the nanoparticle - surfactant interaction [11]. FTIR spectra of solid samples were measured by KBr method. 1-3 mg of the nanoparticles is thoroughly mixed with 350 mg KBr. The mixture was transferred to a die and pelletized. Re-crystallization of the KBr results in a clear glassy disk about 1 mm thick. FTIR spectra were recorded on Cary 660 FTIR spectrophotometer in the mid infrared region (4000-400 cm^{-1}). For Liquid samples, diamond attenuated total reflection (ATR) accessory was used and measurements were performed in reflectance mode. All measurements were performed at room temperature.

2.7 Inductively Coupled Plasma Atomic Emission Spectroscopy

Inductively Coupled Plasma Atomic Emission Spectroscopy (ICP-AES) is used to determine the metal concentration in nanoparticle suspension [12]. It is an emission spectroscopy in which metal under investigation is atomized by high temperature plasma. The electrons in metal atoms excite to higher energy levels and during their deexcitation they emit various emission lines, which are characteristic of a particular metal atom. From the intensity profile of these characteristic emission lines, metal concentration can be determined. In the present study, ICP-AES technique was employed to determine the elemental concentrations of metals in their colloidal state. Prior to each measurement, nanoparticles were digested in aqueous nitric acid solution. Well digested samples were adequately diluted prior to measurement. The measurements were performed on Spectro make ARCOS Inductively coupled plasma atomic emission spectrophotometer at room temperature.

2.8 Scanning Electron Microscopy and Energy Dispersive Spectroscopy

Scanning Electron Microscopy (SEM) is used to investigate surface features of materials at high resolution [13]. The typical resolution that can be obtained with Scanning Electron Microscope is $\times 10^6$. At this resolution, morphological features of nanomaterials can be visualized. In the present study Scanning Electron Microscopy was used to capture micrographs of nanoparticles. The sample for Scanning Electron Microscopy was prepared by dispersing nanoparticles on a copper grid. Prior to microscopy, nanoparticles were coated with a fine layer of platinum to avoid the charging effect of electrons. The SEM micrographs were captured on JEOL JSM 7600F field emission scanning electron microscope operated at 5 keV. This scanning electron microscope is also equipped with energy dispersive spectrometer (EDS) accessory. Quantitative elemental analysis of nanoparticles was also performed by energy dispersive spectroscopy on the same scanning electron microscope.

2.9 Transmission Electron Microscopy and Selected Area Electron Diffraction

Transmission electron microscopy (TEM) is a powerful technique to study size, shape and crystal structure of nanomaterials [14]. Field emission gun is used to generate accelerated electrons of 100-400 keV. Typical magnification of TEM is 10^6 with a resolution of ~1 A°. In this study, TEM micrographs of as-synthesized nanoparticles were recorded on Philips CM200 transmission electron microscope which is operating at an accelerating voltage of 200 kV. TEM images of nanoparticles were captured under bright field conditions. Selected area electron diffraction (SAED) is another mode of electron microscopy in which diffraction patterns are produced by the electrons scattered from the sample lattice. Obeying the Bragg’s law, electrons are scattered elastically by the lattice. Therefore, the diffraction spots in the pattern can be indexed and from the indexing the phase(s) in the sample and their crystal structure has been identified. Every spot in the SAED pattern corresponds to lattice planes of a certain miller index in single crystal while a ring in the SAED pattern corresponds to a group of lattice planes of the same miller index family in the polycrystalline sample. Samples for TEM study was prepared by placing a drop of nanoparticles dispersed in solvent (either water or n-hexane) onto an amorphous carbon-coated copper grid and the solvent was allowed to evaporate slowly by placing the grid under IR radiation.

References

1. A. R. Tao, S. Habas and P. Yang, Small 4, 310-325 (2008).
2. M. S. Usman, M. E. E. Zowalaty, K. Shameli, N. Zainuddin, M. Salama and N. A. Ibrahim, International Journal of Nanomedicine 8, 4467-4479 (2013).
3. N. V. Surmawar, S. R. Thakare and N. T. Khaty, International Journal of Green Nanotechnology 3, 302-308 (2011).
4. B. D. Cullity and S. R. Stock, Elements of X-ray Diffraction, 3rd Ed. Addison-Wesley Publishing Company, Inc. (2002).
5. L. B. McCusker, R. B. V. Dreele, D. E. Cox, D. Louer and P. Scardi, Journal of Applied Crystallography 32, 36-50 (1999).
6. P. Gabbott, Principles and Applications of Thermal Analysis, Wiley-Blackwell (2007).
7. H. H. Perkampus, UV-Vis Spectroscopy and Its Applications, Springer (1992).
8. F. M. Mirabella, Modern Techniques in Applied Molecular Spectroscopy, Wiley (1998).
9. R. Pecora, Dynamic Light Scattering: Applications of Photon Correlation Spectroscopy, Springer (1985).
10. K. Parekh, R. V. Upadhyay and R. V. Mehta, Bulletin of Materials Science 23, 91-95 (2000).
11. B. C. Smith, Fundamentals of Fourier Transform Infrared Spectroscopy, 2nd Ed. CRC Press (2011).
12. E. H. Evans, An Introduction to Analytical Atomic Spectrometry, Wiley (1998).
13. J. J. Bozzola and L. D. Russell, Electron Microscopy, 2nd Ed. Jones & Bartlett Publishers (1998).
14. D. B. Williams and C. B. Carter, Transmission Electron Microscopy: A Textbook for Materials Science, 2nd Ed. Springer (2009).

CHAPTER 3

SYNTHESIS OF METALS AND METAL OXIDE NANOSTRUCTURES AND THEIR PROPERTIES

3.1 Introduction

Development of reliable protocols for the synthesis of materials at nanoscale is an important aspect of nanotechnology. The progress in nanotechnology is largely governed by the availability of perfect nanoscale structures. Nanomaterials possess unique chemical, physical, mechanical, thermal, optical, magnetic, electrical and biological properties [1]. These properties of nanomaterials are tunable and depend on their physical size [2], size distribution [3], surface features [4], functionalization [5], and dispersion stability [6]. These features of nanomaterials can be controlled to desired limit by choosing an appropriate technique for nanomaterials synthesis and fine tuning variables of synthesis protocols. This chapter describes the development of appropriate protocols for the synthesis of metals (silver and copper) and metal oxide (titanium dioxide) nanoparticles with desired physical, chemical, structural, optical and surface properties.

Synthesis of silver nanoparticles (SNPs) by chemical reduction method in the presence of mild reducing agent is a promising approach to achieve high yield SNPs without deteriorating their physical and surface properties [7]. This method has an advantage of yielding nanoparticles with no or little aggregation. In the present study, synthesis of uniform, monodisperse SNPs is carried out by simple one-pot method using oleylamine as reducing and capping agent [8]. It is a two-step process. In the first step, oleylamine capped hydrophobic SNPs are prepared by reducing $AgNO_3$ with oleylamine. Effect of concentration of reducing cum capping agent and growth kinetic parameters i.e. nucleation temperature, growth temperature, nucleation time and growth time on the product quantity and quality is evaluated in terms of colloidal yield, physical size, morphology and dispersity. In the second step, hydrophobic SNPs are phase transferred into water by ligand exchange reaction using block co-polymer, pluronic F- 127 [9]. From the detailed investigation of as-synthesized nanoparticles by various characterization techniques, optimized conditions are being laid down for high yield, monodisperse; water dispersible SNPs that can be directly used as antimicrobial agents in nanomedicine.

Plasmonic nanostructures are gaining increasing attention due to their wide range of applications ranging from plasmonic photovoltaic to photothermal therapy [10-12]. Amongst the plasmonic nanostructures, copper nanoparticles (CNPs) could be a potential alternative to silver and gold but it is largely undermined because of the difficulties in synthesizing high quality, stable, ultra-small CNPs as they are prone to oxidation [13]. The second important aspect dealt-with in this chapter is the development of protocols for the synthesis of ultra-small, plasmonic copper nanostructures, which are resistant to oxidation and stable in ambient environment. In the present study, CNPs are synthesized by chemical reduction of copper chloride under mild reaction conditions by using a unique combination of reducing (sodium borohydride and L-ascorbic acid) and capping (Polyvinylpyrrolidone and L-ascorbic acid) agents. Synthesized CNPs are stable in its native metallic phase (Cu^0) under the dynamic equilibrium established between the surface of CNPs and the capping agents. Synthesized product is stable against both the oxidation and the aggregation and suitable for biomedical applications.

Titanium dioxide nanoparticles (TNPs) are another important system, which are widely researched for their photocatalytic and disinfectant properties [14-16]. The major limitation with TNPs is their photo-response, which lies in the ultraviolet region. Improved photo response in the visible region is the chief target for researchers. This chapter also deals with the development of synthesis protocols for sol-gel synthesis of pristine and Co-doped TNPs. Effect of dopant concentration has been studied on the optical band edge of the TNPs, and the processing parameters and dopant concentration have been optimized for the synthesis of visible light responsive TNPs with uniform size and shape. Subsequent sections of this chapter describe detailed protocols followed for the synthesis of SNPs, CNPs and TNPs and their subsequent characterizations to find their suitability as biocidal agents, which is the subject matter of chapter - 4.

3.2 Synthesis of Silver Nanoparticles (SNPs)

3.2.1 Materials

Silver nitrate ($AgNO_3$) (99.8%) and diphenyl ether were procured from S.D. Fine-Chem. Ltd. Oleylamine (70%) and pluronic F-127 were obtained from Sigma-Aldrich. Absolute ethanol, n-hexane (95%) and HPLC grade water were purchased from Merck. All the chemicals were used as received without any further purification. For all experiments, aqueous solutions are prepared in Millipore ultrapure water (ρ = 18.2 MΩ).

3.2.2 Synthesis Process

SNPs were prepared by reducing $AgNO_3$ with oleylamine (OA) in a simple one pot method. It was reported by Chen et al. [17] that for homogeneous nucleation of silver from $AgNO_3$ by OA, nucleation temperature should be $\geq$ 150 °C. For fast and homogenous nucleation, $AgNO_3$ was added into the oleylamine - diphenylether mixture, which was preheated at 160-240 °C. Ripening of nanoparticles at a lower temperature is critical for homogeneous growth [18]. To achieve better control on the growth of individual crystallites, the reaction temperature was lowered to 150-200 °C [19]. Synthesis protocols followed for the preparation of SNPs are summarized as a flow chart in **Fig. 3.1**. Effect of following process variables has been evaluated on the quality and quantity of SNPs.

1) Concentration of surfactant cum reducing agent (oleylamine)
2) Nucleation temperature
3) Nucleation time
4) Growth temperature
5) Growth time

3.2.2.1 Effect of Oleylamine (OA) Concentration

To investigate the effect of OA concentration on the quality and quantity of SNPs, the concentration of OA was varied from 0.5 mM - 30 mM. In brief, 20 mL diphenyl ether was mixed with desired volume of OA in a three neck 250 mL round bottom flask, equipped with a magnetic stirrer, condenser and a thermometer. The mixture was heated to 200 °C at a rate of 3 °C min^{-1}. 3 mM $AgNO_3$ was added into this preheated mixture under continuous magnetic stirring. Upon addition of $AgNO_3$, the colour of the mixture immediately turned blue. Strong surface plasmon resonance (SPR) was observed, indicating the nucleation of SNPs. The mixture was refluxed for 30 min and then rapidly cooled down to 150 °C. It was then ripened at 150 °C for another 4 h and subsequently cooled to 25 °C.

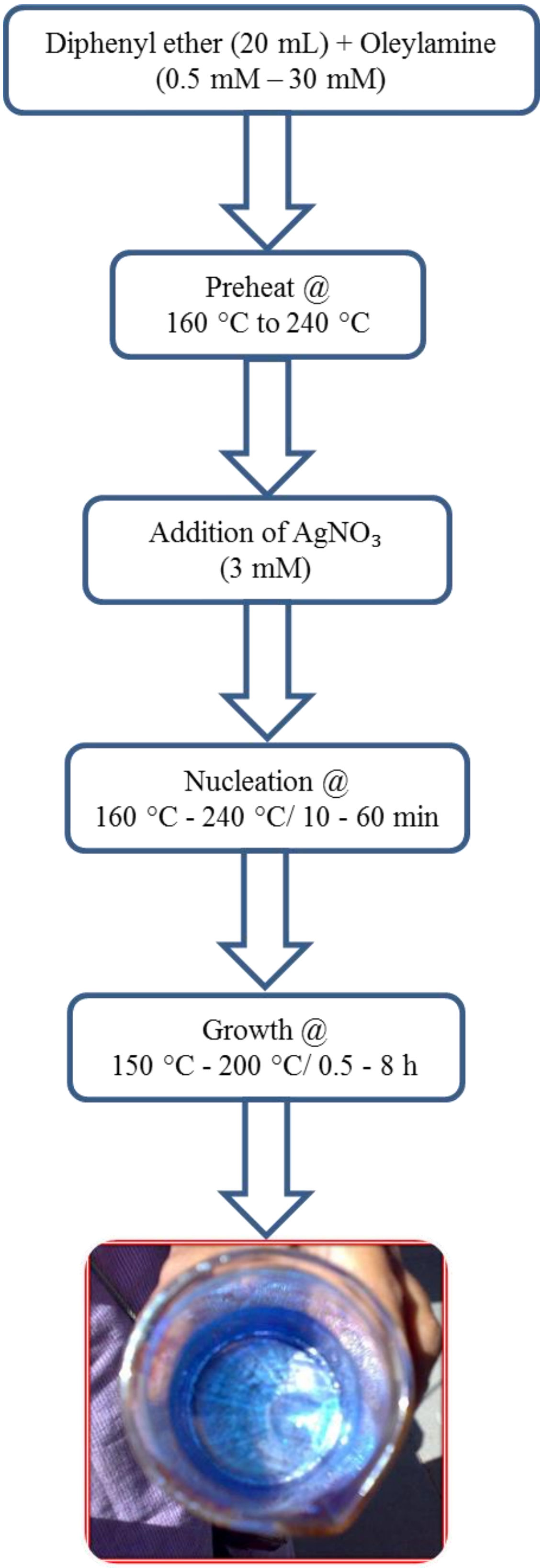

Fig. 3.1 Flowchart of synthesis protocols followed for the preparation of colloidal SNPs. Image (at the end of the flow chart) shows strong surface plasmon resonance in the colloid confirming the formation of SNPs.

The product was purified by the precipitation-redispersion. Equal volume of absolute ethanol was added into the mixture. Alcohol addition precipitates the SNPs which were isolated from the suspension by centrifugation at a relative centrifugal force (RCF) of 10744 x g (10000 rpm) for 10 min. Nanoparticles were then dispersed in 20 mL n-hexane. The dispersion was again centrifuged at 3868 x g (6000 rpm) for 10 min and undispersed residues, if any, were removed. 5 mL SNPs suspension in n-hexane was preserved at 4 °C and rest of the solution was again precipitated with absolute ethanol. The precipitates were collected by centrifugation at 10744 x g (10000 rpm) for 10 min and preserved at room temperature.

Effect of concentration of reducing agent on the quality and quantity of nanostructures has been evaluated in terms of product yield, size and size distribution, crystal phase and morphology. It was observed that irrespective of OA concentration, it always reduces $AgNO_3$ into SNPs with spherical morphology. To understand the effect of concentration of reducing agent on the quantity, % yield of SNPs obtained after precipitation-redispersion was determined. **Fig. 3.2** shows the plot of % yield of SNPs obtained at different OA concentration.

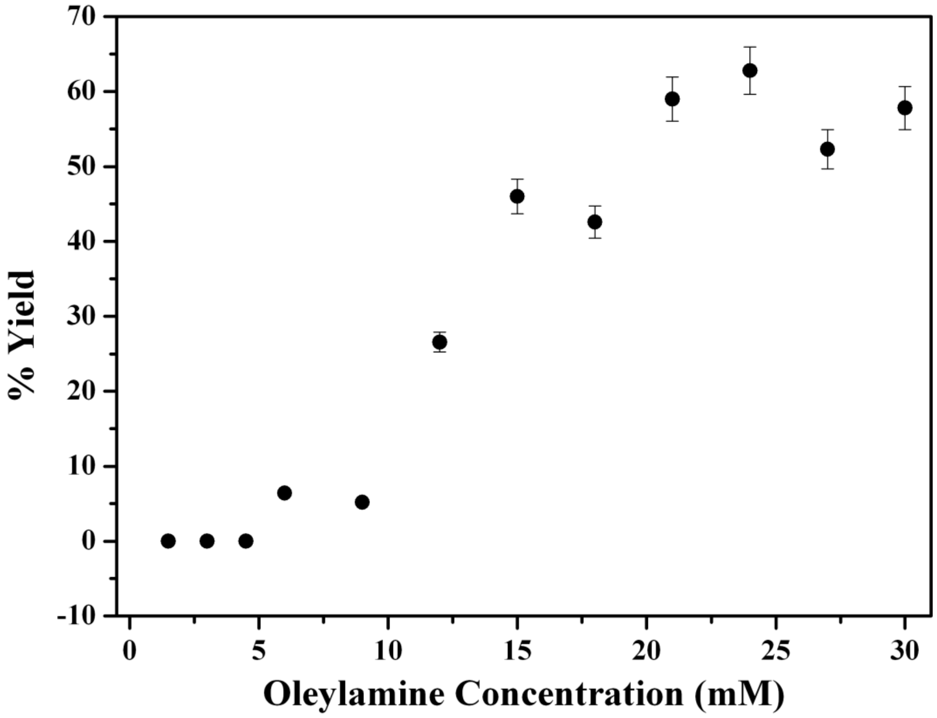

Fig. 3.2 Variation in % yield of SNPs with oleylamine concentration. % yield is measured for the product obtained after the precipitation-redispersion.

SNPs' yield is 0% until OA concentration is > 4.5 mM. This is because no SNPs could be collected from the n-hexane phase after the precipitation - redispersion until the OA concentration is > 4.5 mM. These might be due to coagulation of nanoparticles in the absence of sufficient quantity of OA, which is also acting as capping agent. When the OA concentration is > 4.5 mM, % yield of SNPs increases following an exponential behaviour and saturates at 21 mM of OA. At this concentration, approximately 60% of the initial mass of Ag gets converted into SNPs. Low yield of SNPs might be because of incomplete reduction of $AgNO_3$ and partial losses during the purification.

To evaluate the effect of OA concentration on particle size, X-ray diffraction, transmission electron microscopy and photon correlation spectroscopy techniques were employed. The X-ray diffraction patterns of as-synthesized SNPs show four diffraction peaks (**Fig. 3.3**) corresponding to the FCC structure.

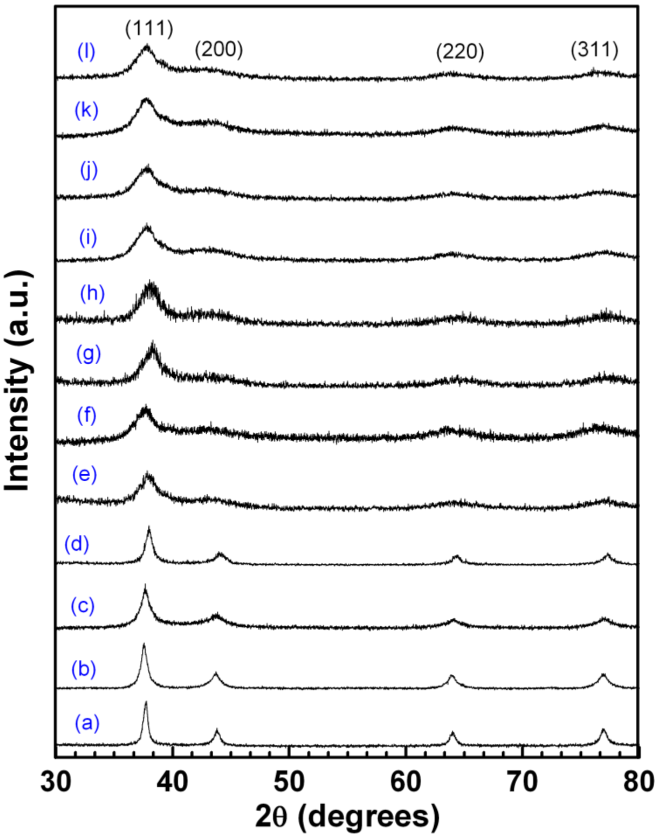

Fig. 3.3 XRD diffractograms of SNPs prepared at different oleylamine concentration. (a) 1.5 mM, (b) 3 mM, (c) 4.5 mM, (d) 6 mM, (e) 9 mM, (f) 12 mM, (g) 15 mM, (h) 18 mM, (i) 21 mM, (j) 24 mM, (k) 27 mM and (l) 30 mM. Samples corresponding to 1.5 - 4.5 mM oleylamine are the undispersed residues obtained during precipitation-redispersion. No dispersed particles could be extracted due to heavy clustering in these samples. The broadening of diffraction peaks increases with oleylamine concentration till 12 mM and is constant above this concentration.

The peaks matched well with the standard PCPDF database (card no. 040783) of silver. Diffraction peaks are quite broad indicating that the particle size of SNPs is very small. A slight variation in the Bragg positions of various reflections has also been observed. This variation might be due to the change in the lattice strain of the nanoparticles. To understand the effect of crystallite size and lattice strain on the size broadening of SNPs, Williamson-Hall analysis was used [20].

Experimentally observed peak broadening (β) is related to crystallite size, t and lattice strain, η by following expression:

$$\beta\cos\theta = \frac{k\lambda}{t} + \eta\sin\theta \tag{3.1}$$

where β is experimentally observed integral breadth of X-ray diffraction peak, θ is diffraction angle, λ is the wavelength of X-ray source (λ = 1.5406 Å), t is crystallite size, η is lattice strain and k (= 0.9) is geometrical constant. By plotting βcosθ vs sinθ, crystallite size and lattice stain has been determined. The plot of crystallite size as a function of OA concentration is shown in **Fig. 3.4**.

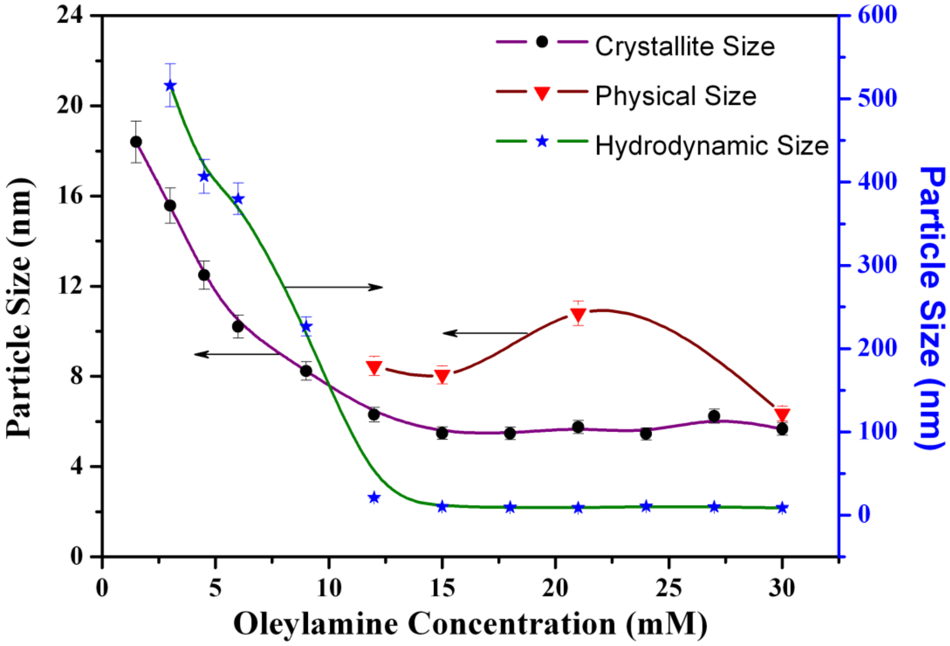

Fig. 3.4 Variation in the crystallite, physical and hydrodynamic particle size of SNPs with oleylamine concentration. Trend lines are drawn for the sake of clear viewing.

The crystallite size decreases exponentially with increasing OA concentration and saturates at ≈ 5.5 nm for 15 mM of OA. This result indicates that the OA traditionally known as a reducing and capping agent also acts as grain growth inhibitor. 15 mM OA is sufficient to produce uniform grains in SNPs. Further increase in OA concentration does not alter the crystallite size but increases the product yield until the OA concentration is 21 mM (**Fig. 3.2**).

The variation of lattice strain of SNPs as a function of OA concentration is shown in **Fig. 3.5(a)**. When OA concentration increases, the lattice strain also increases till the OA concentration is 12 mM. This increase in lattice strain could be due to the corresponding decrease in the crystallite size of SNPs. The lattice strain is independent of OA concentration beyond 12 mM of OA, which is in direct correlation with the crystallite size trend observed in **Fig. 3.4**.

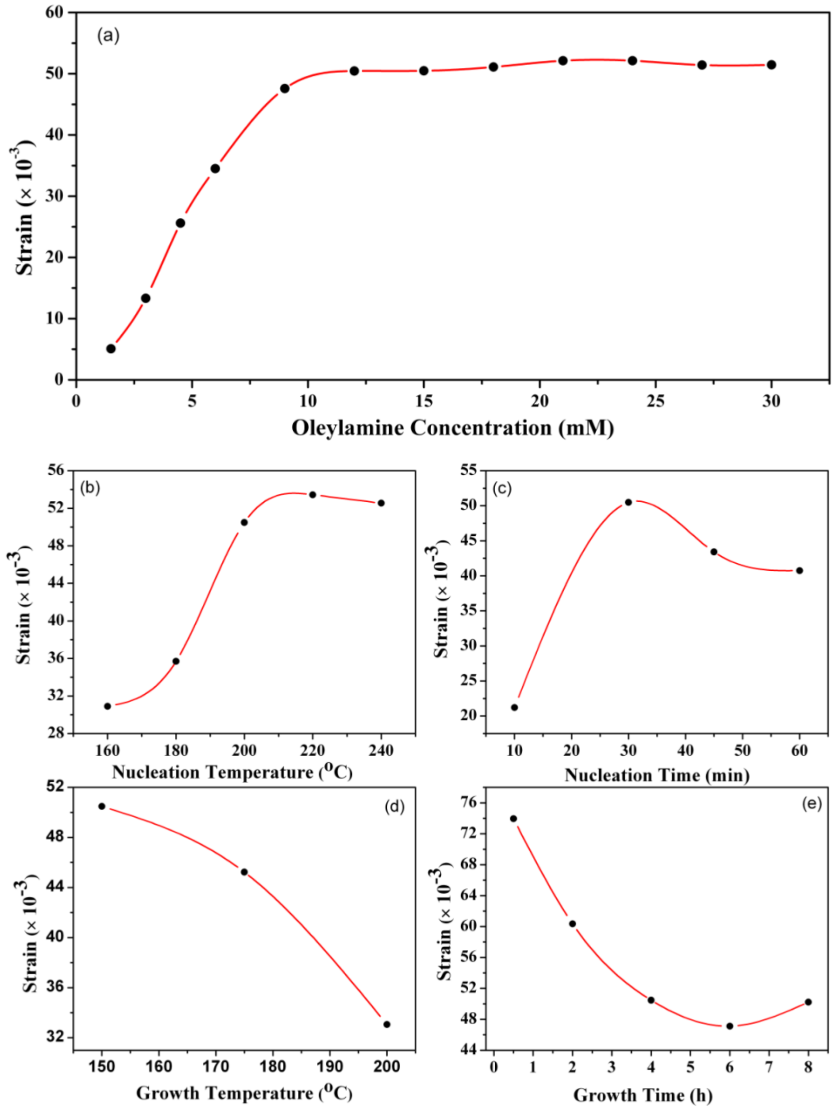

Fig. 3.5 Variation in the lattice strain of SNPs with (a) oleylamine concentration, (b) nucleation temperature, (c) nucleation time, (d) growth temperature and (e) growth time.

To further understand the effect of OA on the physical size and morphology of SNPs, transmission electron microscopy was employed. **Fig. 3.6** shows the representative TEM images of SNPs prepared with different OA concentrations. Each silver nanoparticle has a spherical morphology. Nanocrystals of silver self-assembled into hexagonal closed pack lattice. No agglomeration was observed when OA concentration is ≥ 15 mM.

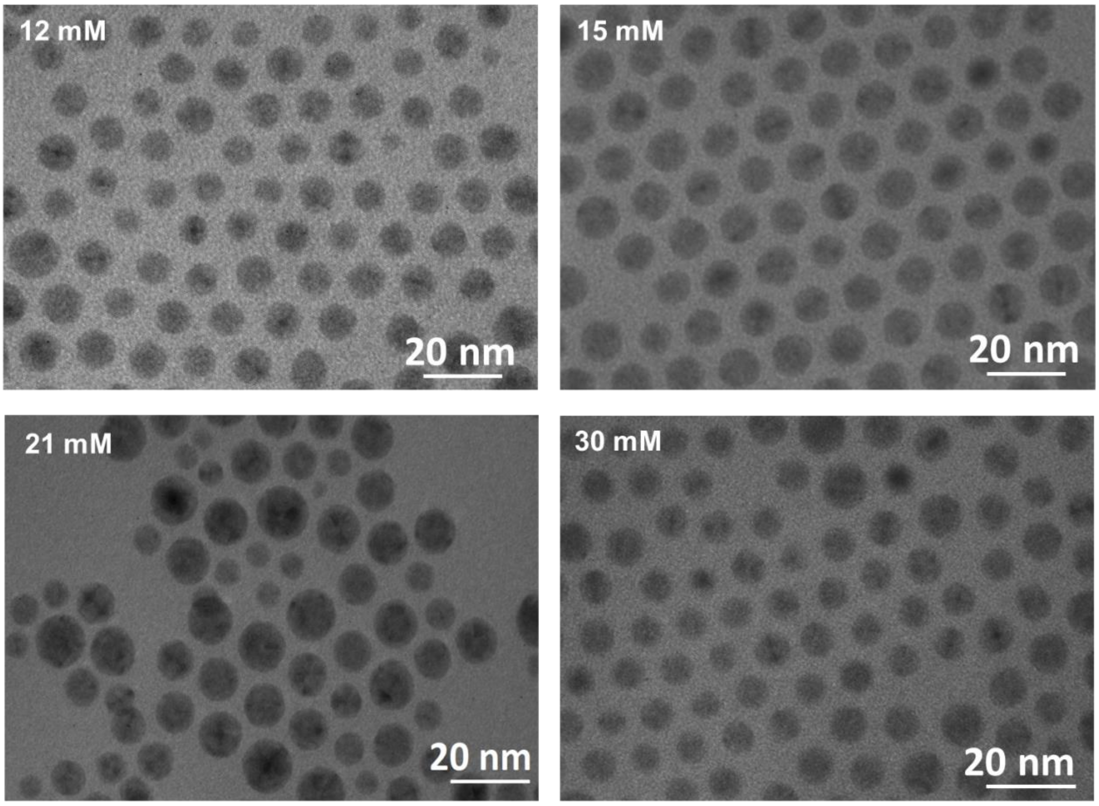

Fig. 3.6 TEM micrographs of as-synthesized SNPs obtained at different oleylamine concentration. Self-assembled hexagonal closed pack structure of SNPs could be observed.

To further understand the effect of OA concentration on the physical size and its distribution, the size distribution histograms were prepared by measuring the diameter of at least 100 particles for each sample. Histograms are fitted with lognormal particle size distribution function [21].

$$P(D) = \frac{1}{(D\sigma\sqrt{2\pi})}\exp\left[-\frac{\left(\ln\left(\frac{D}{D_o}\right)\right)^2}{2\sigma^2}\right] \tag{3.2}$$

where σ is the standard deviation, D the particle diameter and ln D_o is mean of ln D. Histograms are shown in **Fig. 3.7**. The average physical size obtained from the fit are plotted as a function of OA (**Fig. 3.4**). For 15 mM OA, the polydispersity index is 0.17 and for 30 mM OA, it is 0.2. This confirms our belief that the as-synthesized SNPs are nearly monodisperse in size. SNPs prepared with 12 mM and 21 mM OA has higher polydispersity of 0.24 and 0.26, respectively. This might be because of few larger size particles (**Fig. 3.6**). The average inter-particle distance is 3.2 nm. Chain length of an OA molecule is 1.9 nm [22]. It means OA chains attached to the surface of two neighbouring SNPs are entangled by 0.3 nm. Ferrer et al. [22] have also made similar observation.

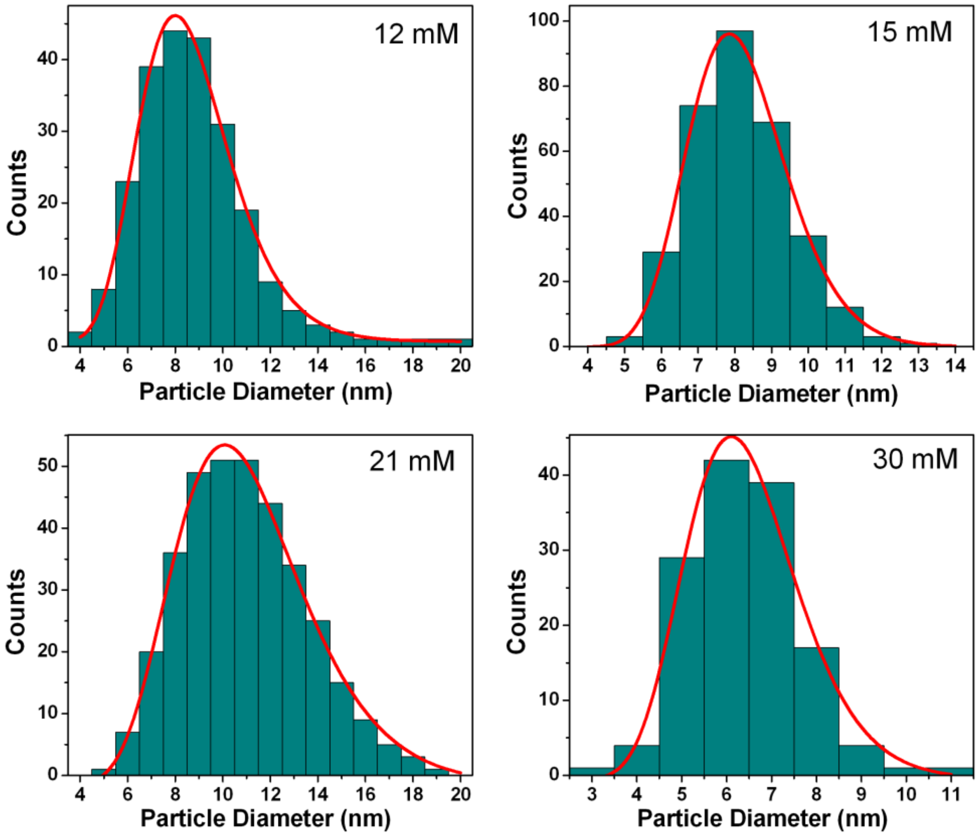

Fig. 3.7 Size distribution histograms fitted with lognormal particle size distribution of SNPs as a function of oleylamine concentration obtained from transmission electron microscopy.

UV-Visible absorption spectra of as-synthesized SNPs are shown in **Fig. 3.8**. Depending on the morphology of nanoparticles, two or more plasmon bands are expected for non-spherical SNPs [23]. In the present study, irrespective of the OA concentration, a single surface plasmon resonance (SPR) band is observed, indicating that the as-synthesized nanostructures have spherical morphology [23]. This observation is also in agreement with the conclusions drawn from the TEM microscopy.

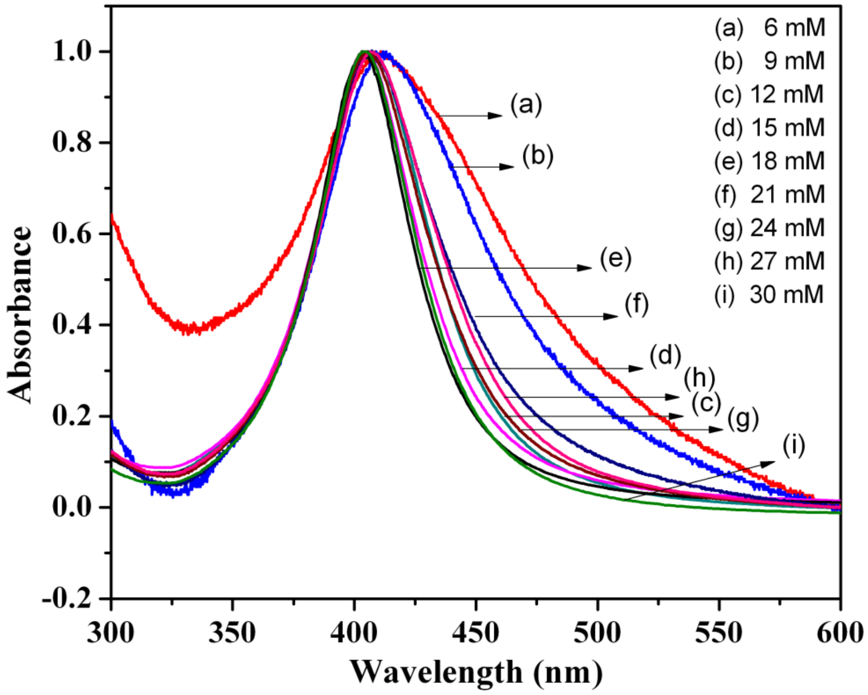

Fig. 3.8 UV-visible spectra of SNPs dispersed in n-hexane as a function of oleylamine concentration. A single SPR band is observed in each spectrum which is centred at 404 nm, confirming the spherical morphology of nanostructures.

The hydrodynamic size distribution of SNPs dispersed in n-hexane was determined by photon correlation spectroscopy. Size distribution histograms were fitted with lognormal particle size distribution function [21] and the mean hydrodynamic size was determined. The hydrodynamic size as a function of OA concentration is also shown in **Fig. 3.4**. As can be seen, the hydrodynamic size of SNPs decreases exponentially as the OA concentration increases and levels off when the OA concentration is ≥15 mM. Lower OA concentration in the medium during the synthesis of SNPs was not able to control the agglomeration and hence resulted in the clusters of SNPs with larger size. As the OA concentration increases, it reduces the tendency of agglomeration of nanoparticles by increasing the electrostatic repulsion between the nanoparticles. The hydrodynamic size levels off at 10.2 nm for OA concentration ≥15 mM. At this concentration, each nanoparticle is coated with a monolayer of OA. This was also confirmed by thermogravimetric analysis. In TG thermogram (**Fig. 3.9**), 13% weight loss was observed, which is corresponding to a monolayer coating of oleylamine on the surface of SNPs.

The mean hydrodynamic size obtained for each concentration of OA is greater than that of crystallite size and physical size obtained from X-ray diffraction and transmission electron microscopy, respectively. This is quite obvious as hydrodynamic size also takes OA coating into the account while the other two methods only consider the bare nanoparticles. The difference between the physical size determined by TEM and the hydrodynamic size obtained from photon correlation spectroscopy gives an estimation of the organic shell around the nanoparticles, which is 2.1 nm when OA concentration is >15 mM. This also agrees well with the earlier observation of monolayer coating of OA on the surface of SNPs [22]. The same conclusion has also been drawn from the measurement of inter-particle distance in the self-assembly of SNPs in TEM micrographs and from the weight loss observed in TG thermogram.

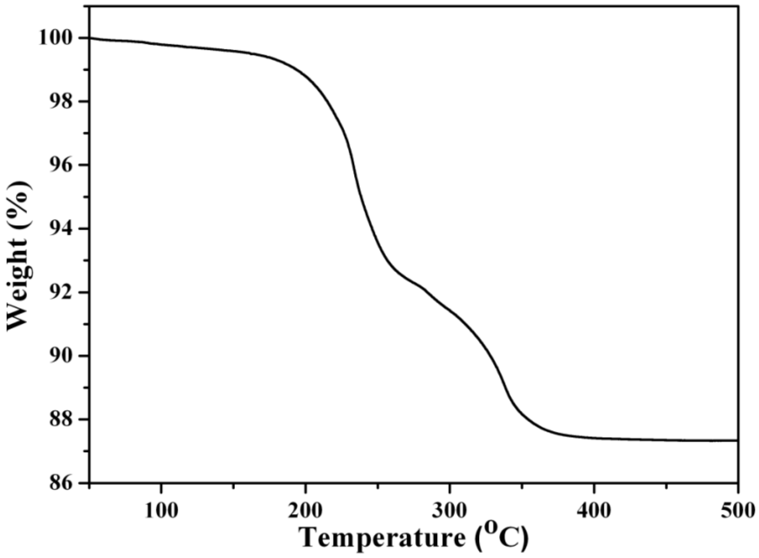

Fig. 3.9 TG thermogram of as-synthesized SNPs prepared with 15 mM oleylamine concentration. 13% weight loss is observed in a two-step process corresponding to the decomposition and carburization of oleylamine.

3.2.2.2 Effect of Nucleation Temperature (N_T)

To understand the effect of nucleation temperature on the quality and quantity of SNPs, the nucleation temperature (N_T) was varied from 160 °C to 240 °C in the regular intervals of 20 °C, while keeping the OA concentration constant at 15 mM. Rest of the parameters i.e. nucleation time (30 min), growth temperature (150 °C) and growth time (4 h) were same as used in the experiments of section 3.2.2.1. Both dispersion and precipitates of SNPs were obtained by following the identical protocols as explained in section 3.2.2.1 and purified samples were preserved at 4 °C for subsequent studies.

SNPs synthesis is a two-step process. In the first step, homogenous nucleation is achieved by minimizing the free energy of the system and in the second step; growth of these nuclei is realized by providing favourable conditions for growth. High activation energy is involved in nucleation, while the growth requires low energy. In the crystal growth, nucleation and growth mechanisms overlap and it is impossible to suppress the two. The final size and the shape of the nanoparticles also depend on the relative rates of these two competitive processes that could be controlled by reaction parameters like concentration, temperature, pH, reducing ability, etc. [24]. It is observed that for homogeneous nucleation of SNPs from $AgNO_3$ by OA, it is necessary to have N_T between 160 °C-240 °C.

Fig. 3.10 shows the effect of variation of N_T on the yield of SNPs. With increase in N_T, SNPs yield increases. When N_T = 200 °C, the yield is maximum at 46%. Further increase in N_T decreases the yield of SNPs. This observation suggests that N_T has major effect on the yield of SNPs. It is expected that nanoparticles' yield should increase with N_T because of the high reduction rate of $AgNO_3$ at elevated temperatures. It should saturate at a temperature where the rate of reduction is maximum. Instead the yield picks at 200 °C followed by a sharp decrease. This can be understood if we consider controlled aggregation of nanoparticles followed by ripening at lower temperatures.

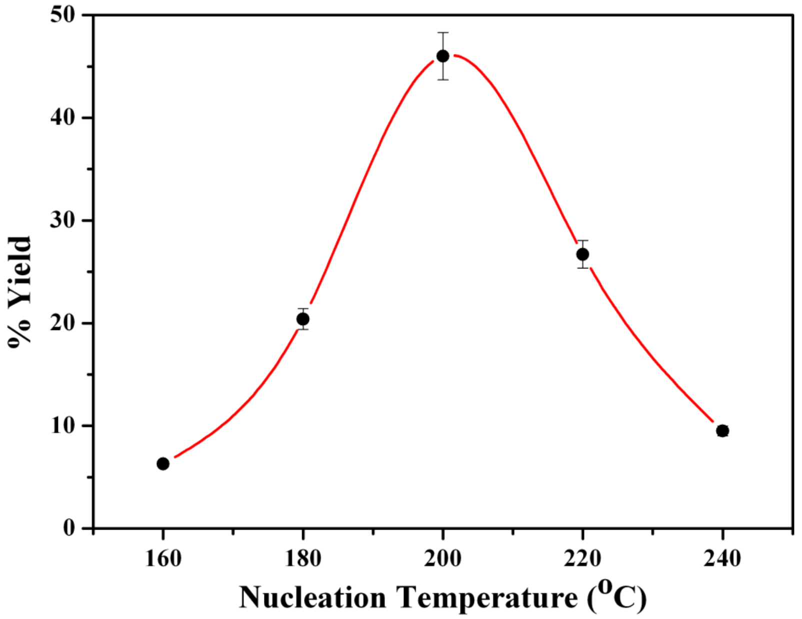

Fig. 3.10 Variation in % Yield of SNPs with nucleation temperature. Trend line is drawn for the sake of clear viewing.

During the growth of nanoparticles, two competitive processes affect the yield of nanoparticles: (i) N_T and (ii) $\Delta T = N_T - G_T$. When N_T is 160 °C i.e. just 10 °C above the G_T (= 150 °C), the yield is very low. This is because of the poor reducibility of $AgNO_3$ by OA at this temperature. As N_T increases, the yield also increases until N_T = 200 °C. At this temperature, the nanoparticle yield is maximum due to the highest rate of reduction at 200 °C. It is expected that further increases in N_T should not affect the yield as the reduction rate is already in saturation, but contradictory to that the yield falls above 200 °C. This decrease in yield might be due to a large ΔT ($\geq$ 50 °C). During the synthesis when the mixture was abruptly cooled to the G_T (= 150 °C) from N_T > 200 °C, the embryo will start dissolving in the growth medium. When ΔT is large, only few nuclei could survive before the beginning of the growth stage. This would result in decrease in the yield of SNPs for N_T is > 200 °C. Hence, the controlled aggregation followed by sintering is essential for homogeneous growth and the difference between nucleation and growth temperature should not exceed 50 °C to achieve a high yield of SNPs.

Irrespective of N_T, SNPs crystallizes into FCC lattice. The X-ray diffraction pattern of SNPs presented at different nucleation temperature is shown in **Fig. 3.11**. It matches well with the X-ray diffraction pattern of bulk silver reported in PCPDF no. 040783. The variation in crystallite size as a function of N_T obtained from the Williamson-Hall analysis of X-ray diffractograms (**Fig. 3.11**) is shown in **Fig. 3.12**. The crystallite size of SNPs ranges between 5.5-7.15 nm. This means that nucleation temperature does not affect the crystallite size much. The variation of lattice strain as a function of N_T is shown in **Fig. 3.5(b)**. Lattice strain gradually increases from 31×10^{-3} to 50×10^{-3} when N_T was raised from 160 °C to 200 °C. Beyond this temperature, lattice strain is independent of N_T. This observation is in agreement with very small change observed for crystallite size of SNPs in **Fig. 3.12**.

The representative TEM micrographs of SNPs prepared at different N_T is shown in **Fig. 3.13**. When the N_T is 160 °C, non-spherical SNPs were obtained whose mean size is 10.14 ± 0.04 nm. When the N_T is 200 or 240 °C, self-assembly of spherical SNPs were obtained. The average physical size of SNPs is 8.07 ± 0.02 nm for N_T = 200 °C and 9.65 ± 0.05 nm for N_T = 240 °C. The mean sizes are obtained from the best fit of the size distribution histograms with lognormal size distribution function [21]. The random morphology of SNPs in case of N_T = 160 °C may be due to the poor control over aggregation during ripening. Both particle size and polydispersity index were minimum for N_T = 200 °C. This might be due to optimum conditions for controlled aggregation and sintering at this temperature. A similar trend was also observed for yield data (**Fig. 3.10**).

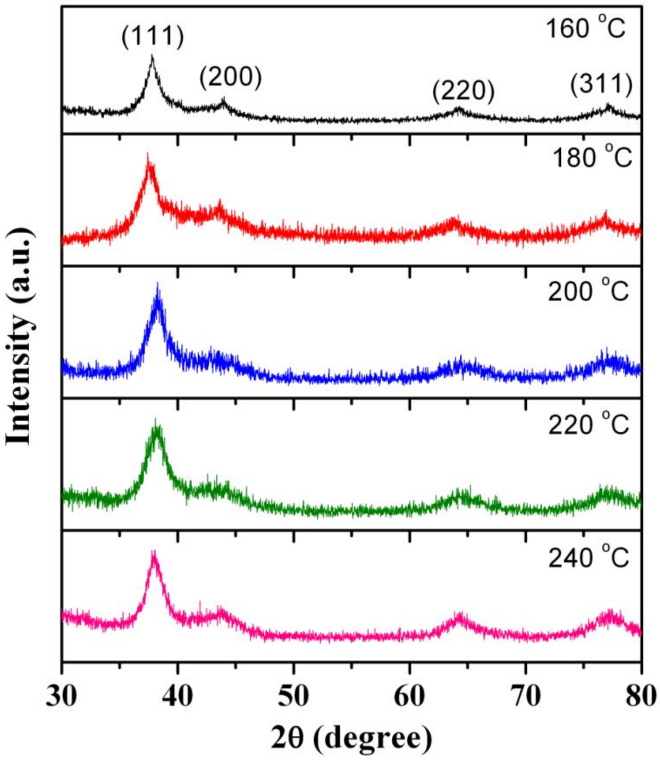

Fig. 3.11 XRD diffractograms of SNPs prepared at different nucleation temperatures.

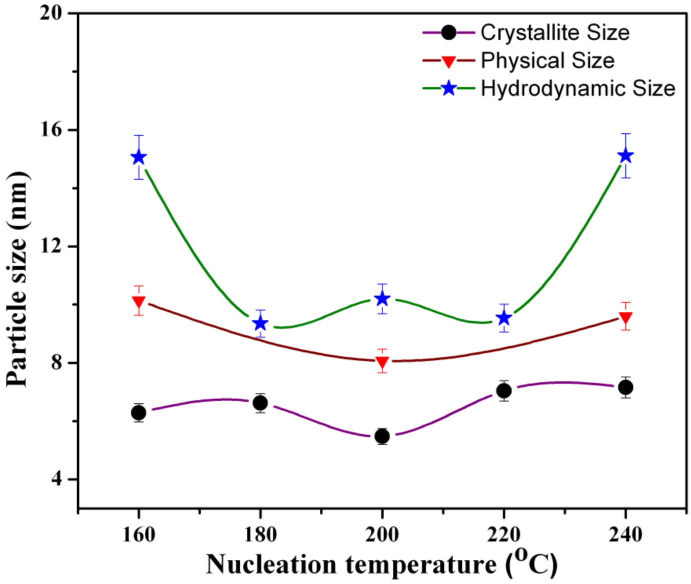

Fig. 3.12 Variation in the crystallite, physical and hydrodynamic particle size of SNPs as a function of nucleation temperature. Trend lines are drawn for the sake of clear viewing.

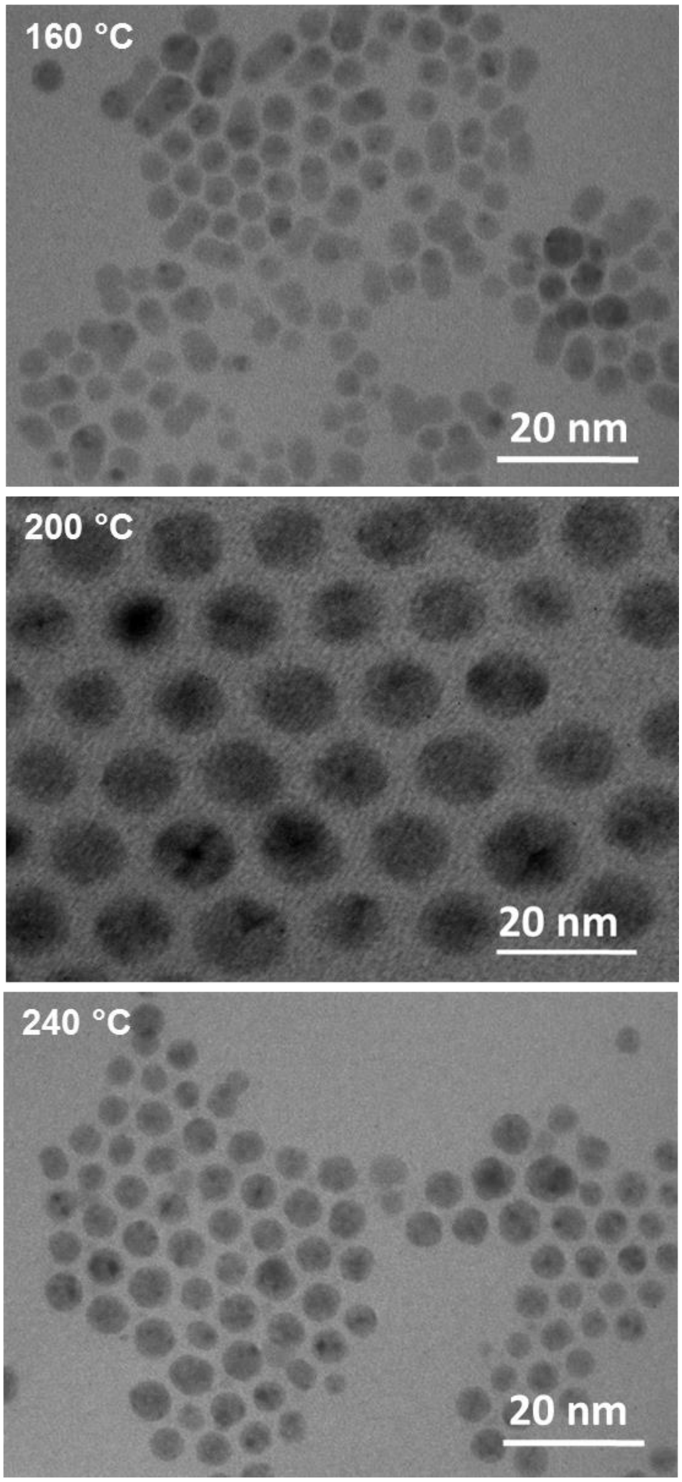

Fig. 3.13 TEM micrographs of as-synthesized SNPs prepared at different nucleation temperatures.

Fig. 3.12 shows the variation in the hydrodynamic size of SNPs as a function of N_T. The same trend as observed in physical size measured by TEM microscopy is followed here. The earlier explanation for the physical size variation as a function of nucleation temperature is applicable for hydrodynamic size too, as the N_T does not affect the interaction of surfactant molecules with nanoparticles. The hydrodynamic size is constant at 9.7 ± 0.4 nm for N_T = 180-220 °C while it increases to 15 nm when N_T is either 160 °C or 240 °C. This might be due to very small and very large difference between N_T and G_T at these temperatures.

UV-visible spectra of SNPs prepared at different nucleation temperatures are shown in **Fig. 3.14**. Irrespective of nucleation temperature, a single SPR band is observed. It is centred at 404 nm. No change in the position and shape of SPR band shows that the morphology of the SNPs did not depend on the nucleation temperature.

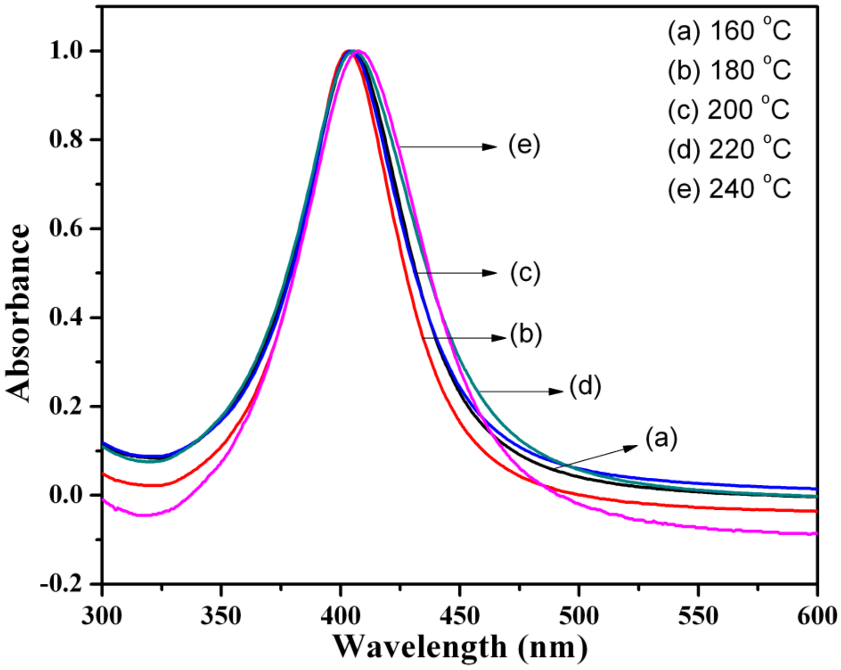

Fig. 3.14 UV-visible spectra of SNPs dispersed in n-hexane as a function of nucleation temperature. A single SPR band is observed in each spectrum which is centred at 404 nm, confirming the spherical morphology of nanostructures.

3.2.2.3 Effect of Nucleation Time (N_t)

To investigate the effect of nucleation time on the product quality and quantity, oleylamine - diphenylether mixture was refluxed at 200 °C for desired nucleation time to promote uniform nucleation. N_t was varied from 0-60 min by keeping rest of the growth variables identical to that used in section 3.2.2.1. OA concentration was constant at 15 mM. Four samples were prepared with N_t of 0, 30, 45 and 60 min. SNPs are purified and preserved by following the same protocols as explained in section 3.2.2.1.

Variation in the % yield of SNPs as a function of N_t is shown in **Fig. 3.15**. The highest yield (≈ 46%) is obtained when N_t is 30 min. When N_t is > 30 min, the yield abruptly decreases to below 20%. This is unusual, generally an increase in N_t should increase the product yield followed by saturation. The contradictory trend observed here might be due to the smaller size of nuclei, which might have nucleated during the last phase of the nucleation compared to those which were nucleated during the early stage of nucleation. These delayed nuclei are susceptible to dissolution during the rapid cooling. N_t = 30 min is optimum. Increasing N_t beyond this decreases the yield of the SNPs.

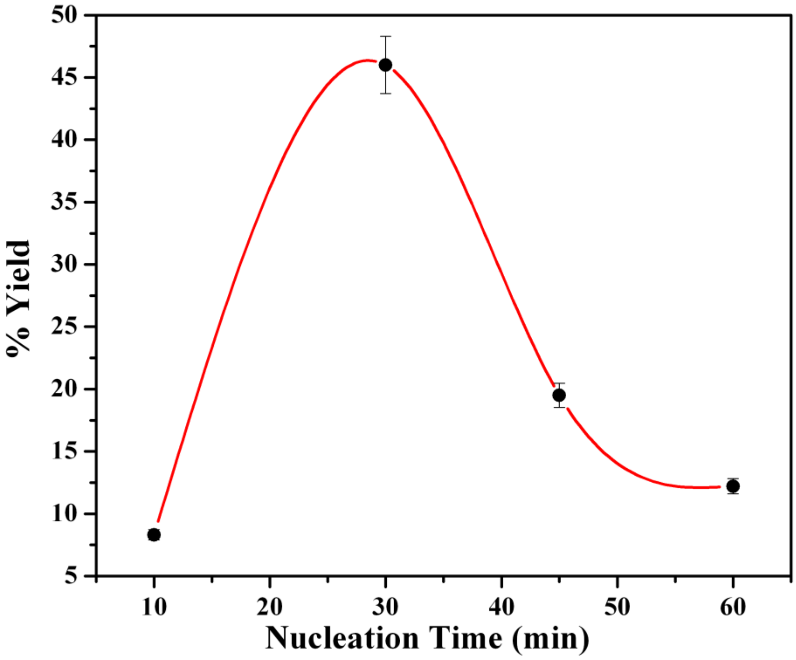

Fig. 3.15 Variation in % Yield of SNPs with nucleation time. Trend line is drawn for the sake of clear viewing.

To further understand the effect of N_t on the particle size and its distribution, X-ray diffraction, transmission electron microscopy and photon correlation spectroscopy were employed. The X-ray diffraction pattern of as-synthesized SNPs is presented in **Fig. 3.16**. In each diffractogram, four well resolved diffraction peaks corresponding to the standard FCC lattice of silver is observed. **Fig. 3.17** shows variation of crystallite size obtained from Williamson-Hall analysis of XRD, physical size obtained from TEM and hydrodynamic size from PCS measurements. The nature of particle size variation with N_t is similar for all the three particle size types. The minimum size in each case was observed when N_t is 30 min. On either side of this i.e. when N_t is higher or lower than 30 min, the particle size is larger than obtained at 30 min.

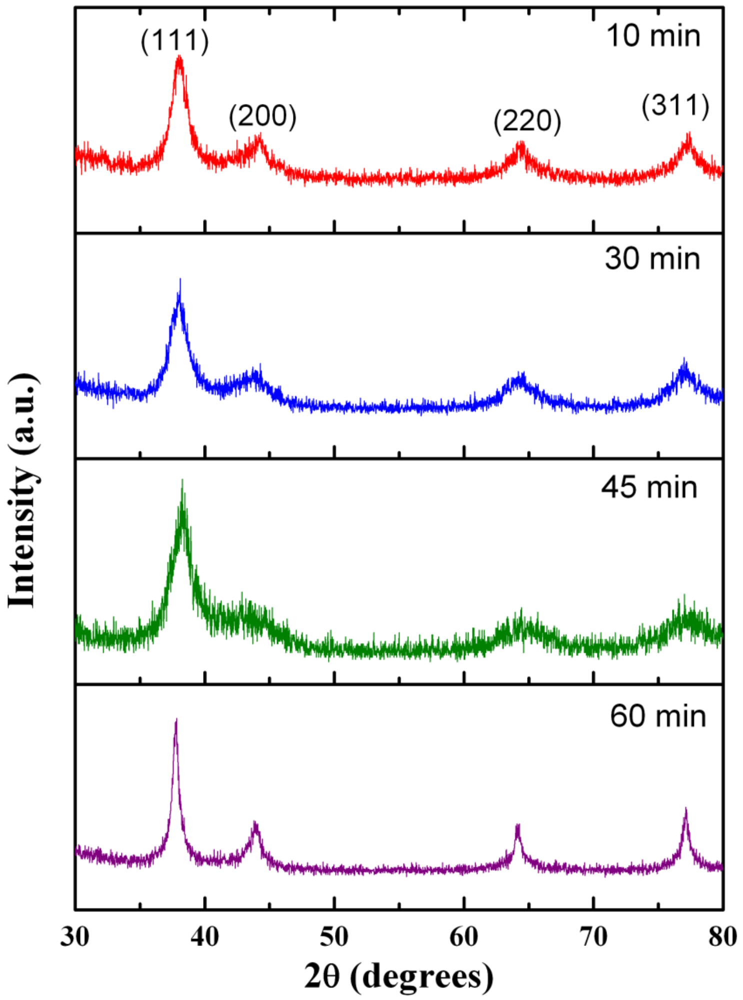

Fig. 3.16 XRD diffractograms of SNPs prepared at different nucleation time.

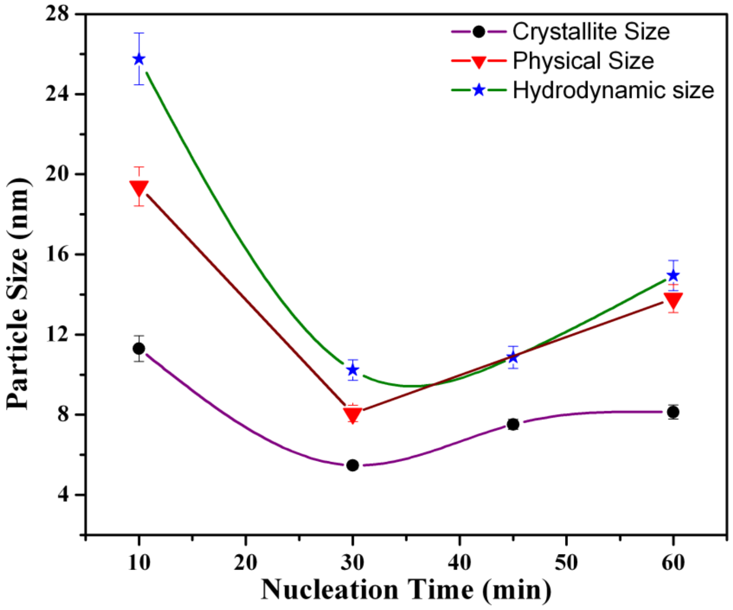

Fig. 3.17 Variation in the crystallite, physical and hydrodynamic particle size of SNPs as a function of nucleation time. Trend lines are drawn for the sake of clear viewing.

When N_t is small, i.e. 10 min, very few nuclei could nucleate. During the growth stage, these fewer nuclei would grow rapidly as the concentration of silver ions per nuclei in the growth medium is quite high. On the other hand, when the N_t is high i.e. 45 min or 60 min, large number of nucleation took place initially that result in the decrease in the concentration of silver ions per nuclei available in the solution. Each nuclei would grow to a small size. N_t = 30 min is the optimum time to prepare smaller size, good quality SNPs with a moderately high yield (46%). This claim is also validated by TEM micrographs in the **Fig. 3.18**.

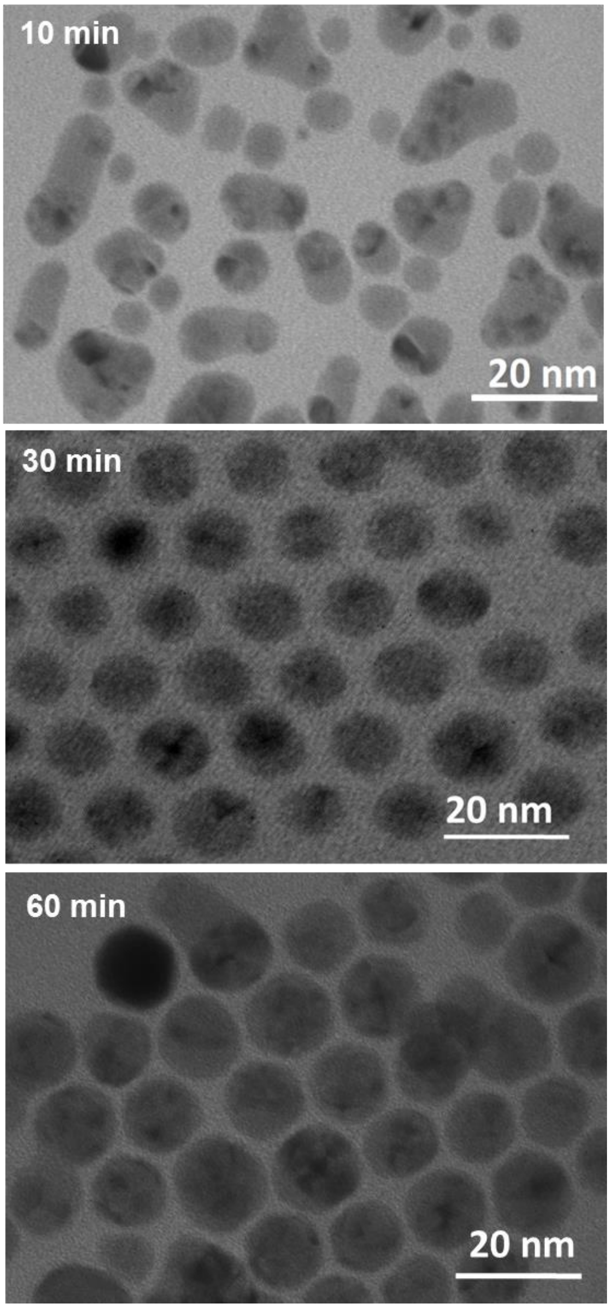

Fig. 3.18 TEM micrographs for SNPs prepared with different nucleation time.

SNPs prepared with N_t = 10 min have stronger tendency to agglomerate. These particles have irregular shape, larger size and broad size distribution. While SNPs prepared with N_t = 30 min are of uniform shape, smaller size and narrower size distribution. They self-assembled into HCP structure. The mean size of nanoparticles is 8.07 ± 0.02 nm. The TEM image of nanoparticles with N_t = 60 min also shows the high quality of the product. The only difference between the SNPs of two samples is their physical sizes. The mean size of SNPs for N_t = 60 min is 13.8 ± 0.03 nm. The hydrodynamic size also follows the same trend as observed for crystallite and physical sizes. The nucleation time does not affect the chemical interaction of OA with the surface of SNPs. Because of smaller size, strict size distribution and greater yield of SNPs obtained with N_t = 30 min, it is preferred over N_t = 60 min.

Fig. 3.5(c) shows variation of lattice strain as a function of N_t. The lattice strain is minimum when N_t = 10 min. As N_t increases to 30 min, the lattice strain peaks at 50×10^{-3}. This might be because of corresponding decrease in crystallite size at this N_t. Further increase in N_t marginally decreases the lattice strain. This observation is in consistent with gradual increase in crystallite size for N_t > 30 min. UV-visible absorption spectra of SNPs prepared at different N_t are shown in **Fig. 3.19**. A single SPR band is observed which is centred at 404 nm. The presence of only SPR band in the UV-visible spectra means that irrespective of their nucleation time, nanoparticles grow with spherical morphology.

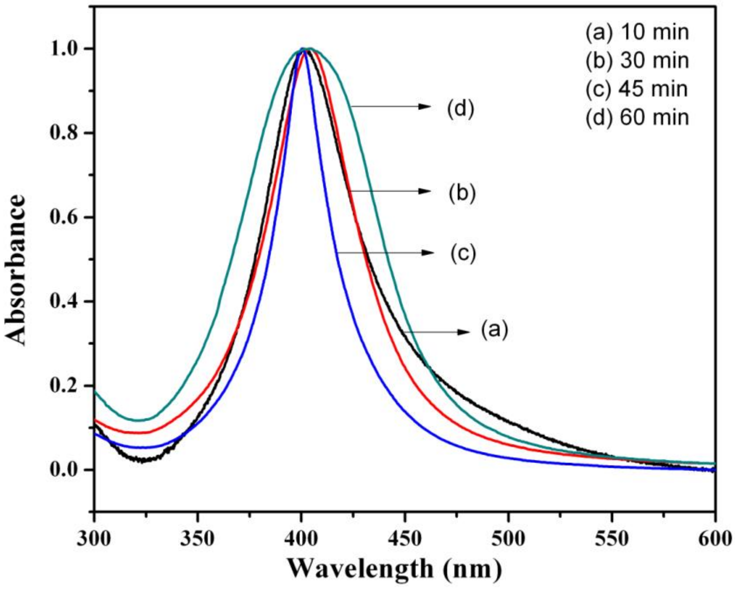

Fig. 3.19 UV-visible spectra of SNPs dispersed in n-hexane as a function of nucleation time. A single SPR band is observed in each spectrum which is centred at 404 nm, confirming the spherical morphology of nanostructures.

3.2.2.4 Effect of Growth Temperature (G_T)

To investigate the effect of G_T on the quality and quantity of the SNPs, the G_T was varied from 150 °C to 200 °C at intervals of 25 °C. Rest of the experimental conditions were kept unchanged as per section 3.2.2.1 with OA concentration fixed at 15 mM.

The correlation between the growth temperature and product quantity is established in terms of the % yield of SNPs. It is shown in **Fig. 3.20**. The yield of SNPs decreases with increase in G_T. The maximum yield (46%) was obtained when G_T = 150 °C. Increase in G_T reduces the temperature difference between the nucleation and growth temperatures. As observed previously when ΔT (= $N_T - G_T$) decreases, the yield also decreases because of the obvious reasons as explained in section 3.2.2.3.

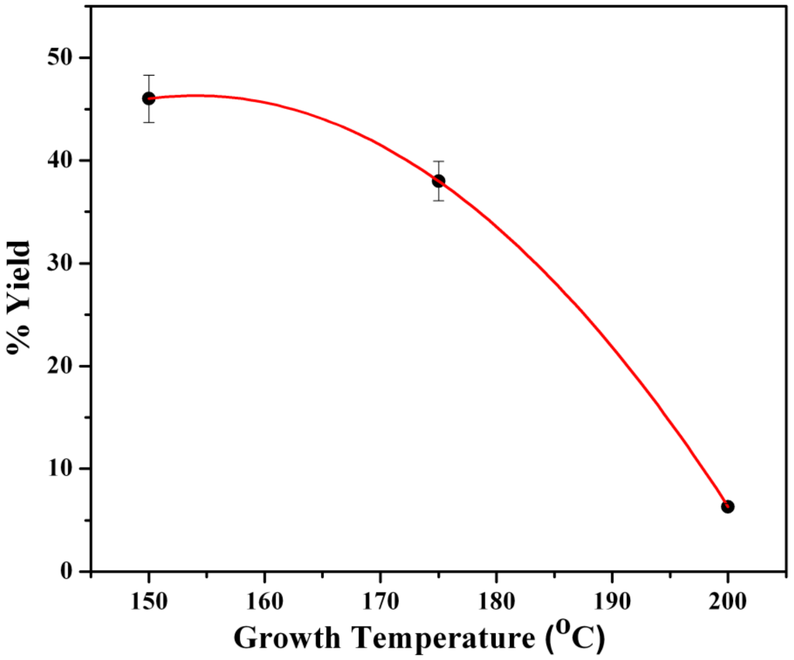

Fig. 3.20 Variation in % Yield of SNPs with growth temperature. % yield is measured from the product obtained after the precipitation-redispersion. Trend line is drawn for the sake of clear viewing.

Effect of G_T on the particle size of SNPs was evaluated by measuring their crystallite, physical and hydrodynamic sizes. Variation of each of these sizes as a function of G_T is shown in **Fig. 3.21**. The crystallite size calculated from X-ray diffractograms of SNPs (**Fig. 3.22**) is constant at 6 nm when G_T is 150 °C and 175 °C, while it increases to 15 nm when the G_T is same as N_T i.e. 200 °C. The lattice strain gradually decreases when G_T is raised from 150 °C to 175 °C (**Fig. 3.5(d)**). Further increase in G_T to 200 °C sharply decreases the lattice strain in SNPs. This might be because of sharp increase in the crystallite size at this G_T.

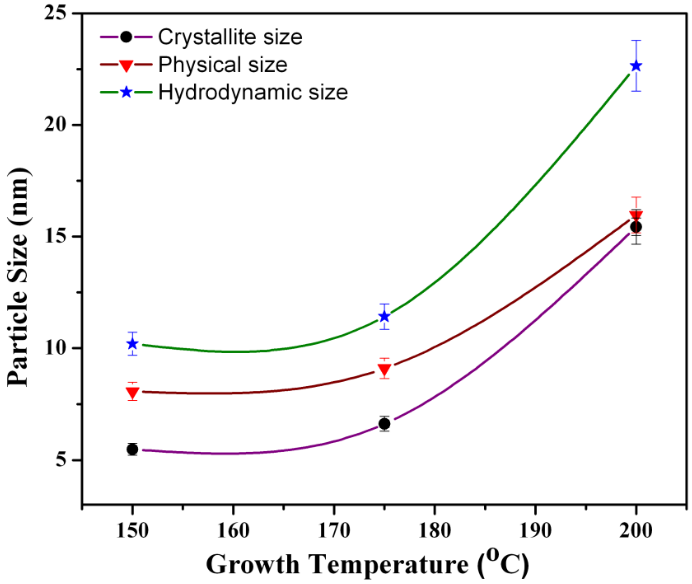

Fig. 3.21 Variation in the crystallite, physical and hydrodynamic particle size of SNPs as a function of growth temperature. Trend lines are drawn for the sake of clear viewing.

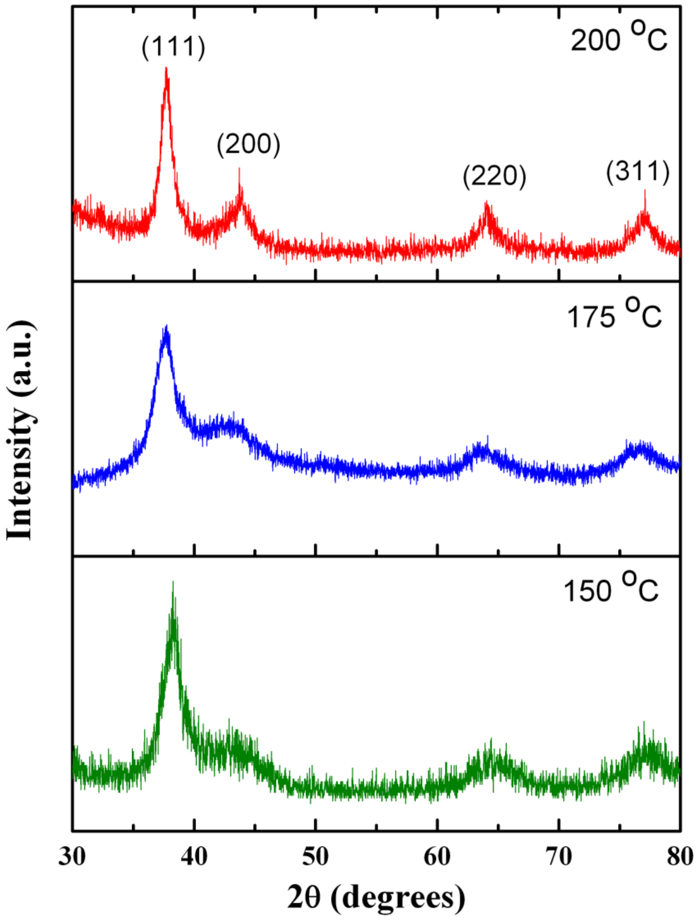

Fig. 3.22 XRD diffractograms of SNPs prepared at different growth temperature.

To further understand the effect of G_T on physical size of nanoparticles, TEM was employed. TEM micrographs of SNPs prepared with different G_T are shown in **Fig. 3.23**. SNPs self-assembled into HCP structure when prepared with G_T = 150 °C. Increase in G_T deteriorated the morphology of SNPs. For G_T = 175 °C and 200 °C, polydispersed non-uniform nanoparticles were formed.

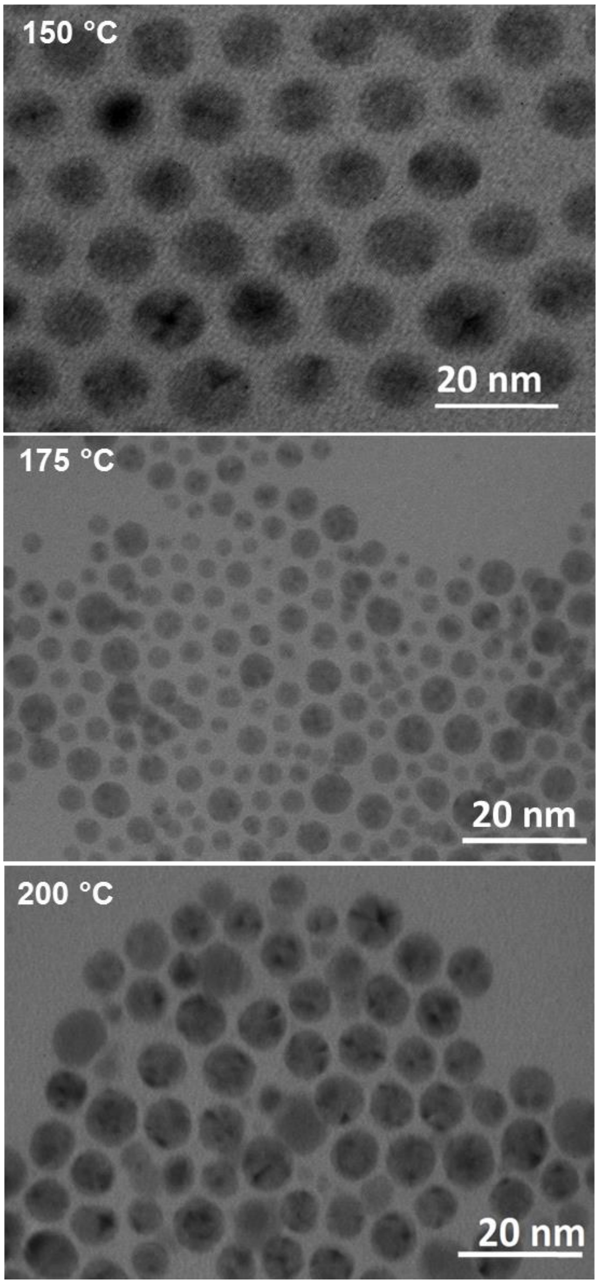

Fig. 3.23 TEM micrographs of SNPs prepared at different growth temperatures.

Hydrodynamic size of SNPs as a function of G_T is plotted in **Fig. 3.21**. It follows the similar trend as observed for crystallite and physical sizes. All the three particle sizes of SNPs i.e. crystallite, physical and hydrodynamic have their maximum values for G_T =

200 °C. This might be due to the copious agglomeration caused by the rapid growth of nanoparticles. The minimum for each of these sizes is observed at G_T = 150 °C. There is a little difference between the particle size obtained at 150 °C and 175 °C. But when considering the yield (**Fig. 3.20**) and quality of nanostructures (**Fig. 3.23**), G_T = 150 °C gives better result in comparison to G_T = 175 °C. Hence, G_T = 150 °C is the optimum growth temperature for the synthesis of good quality SNPs.

The UV-visible spectra of SNPs prepared with different growth temperatures (150-200 °C) are shown in **Fig. 3.24**. As expected, a single SPR band is again observed which is attributed to the spherical morphology of SNPs.

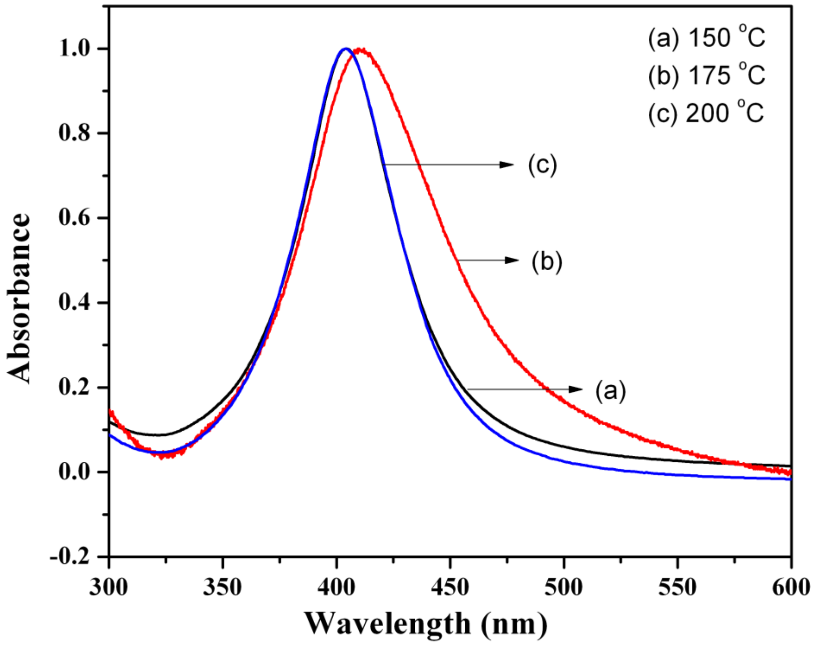

Fig. 3.24 UV-visible spectra of SNPs dispersed in n-hexane as a function of growth temperature. A single SPR band is observed in each spectrum which is centred at 404 nm, confirming the spherical morphology of nanostructures.

3.2.2.5 Effect of Growth Time (G_t)

Another important parameter that could affect the quality and quantity of SNPs is the growth time. To evaluate the effect of G_t on the product, it was varied from 0.5 h - 8 h. No changes were made in the experimental protocols, which are described in section 3.2.2.1. Effect of G_t on the yield of SNPs is shown in **Fig. 3.25**. SNPs yield increases linearly with G_t. The highest yield (76%) was observed when G_t = 8 h. When G_t = 6 h, the yield of SNPs drastically decreases to 12.5%. Despite of several repetitions of this experiment, same result was observed. The reasons behind low yield for G_t = 6 h is unclear.

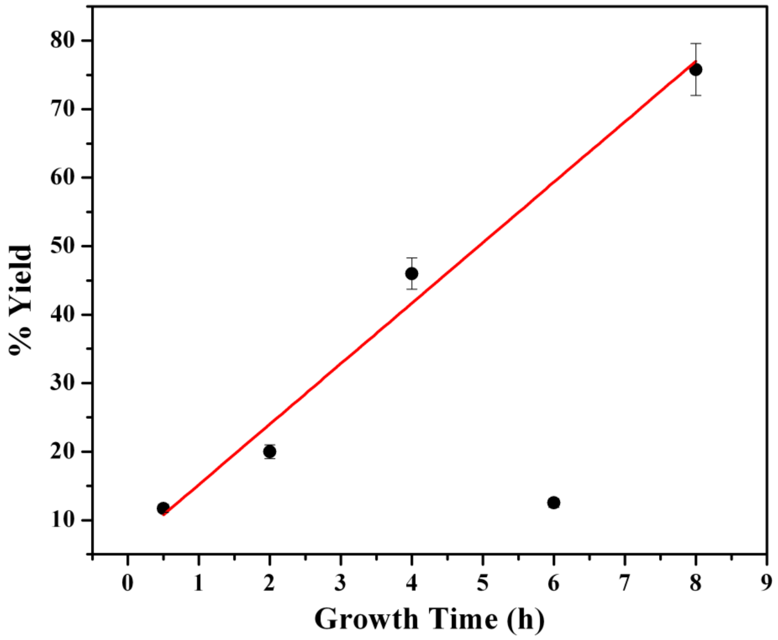

Fig. 3.25 Variation in % yield of SNPs with growth time. Trend line is drawn for the sake of clear viewing.

Fig. 3.26 shows the effect of G_t on the crystallite size of nanostructures calculated from the X-ray diffraction data presented in **Fig. 3.27**. The crystallite size varies between 3 nm - 6 nm when G_t is varied from 0.5 h - 8 h. The crystallite size jumps to 8 nm when G_t is 6 h. Except for G_t = 6 h, the crystallite size does not vary much with G_t and hence can be considered as independent of G_t.

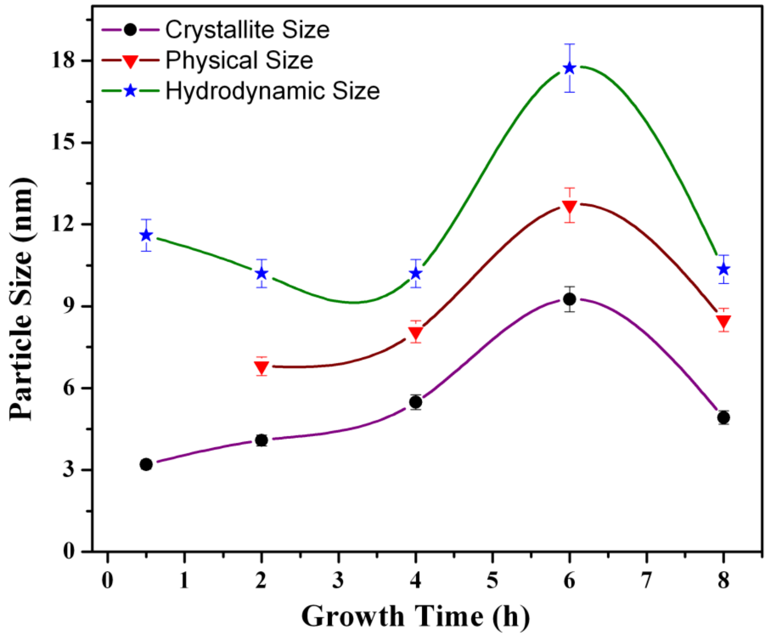

Fig. 3.26 Variation in the crystallite, physical and hydrodynamic particle size of SNPs as a function of growth time. Trend lines are drawn for the sake of clear viewing.

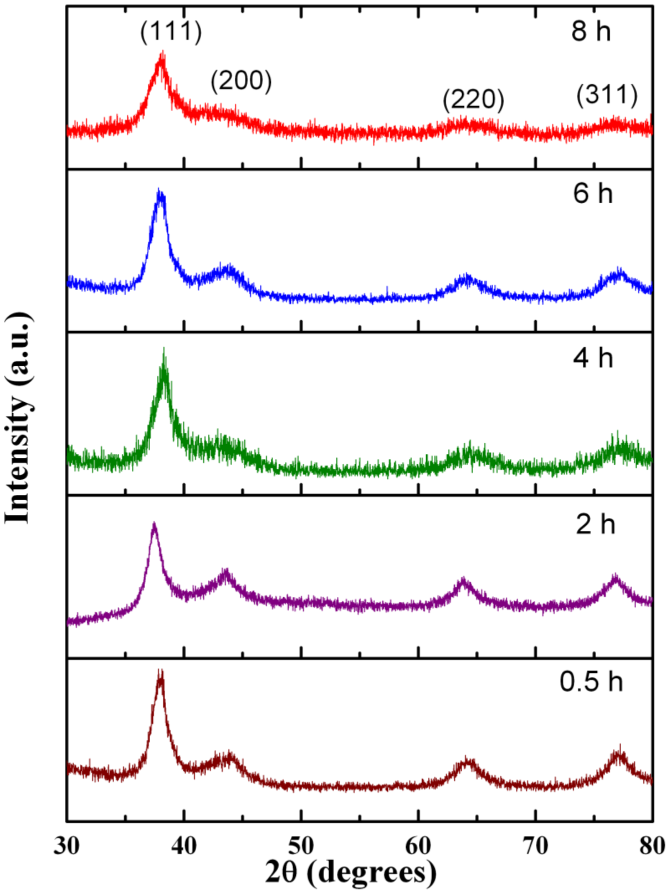

Fig. 3.27 X-ray diffractograms of SNPs prepared at different growth time.

The variation of lattice strain as a function of growth time is shown in **Fig. 3.5(e)**. It decreases exponentially when G_t increases from 0.5 h - 6 h. Beyond this, there is a little increase in the lattice strain of SNPs. This might be because of change in crystallite size trend (increases upto G_t = 6 h followed by a decrease) at G_t = 6 h. The TEM micrographs of SNPs corresponding to different G_t are shown in **Fig. 3.28**. Irrespective of G_t, self-assembled HCP structures are observed; indicating that the tight size dispersion of SNPs can be obtained in the studied range of G_t. Variation in the physical size of SNPs obtained from TEM is also plotted in **Fig. 3.26**. The particle size ranges between 7-10 nm. The large difference between the crystallite and physical size of nanoparticles for G_t = 6 h and G_t = 8 h might be due to the polycrystalline nature of SNPs. The hydrodynamic size is independent of G_t (**Fig. 3.26**). Irrespective of G_t, the mean hydrodynamic size is between 10-12 nm except for G_t = 6 h where the size is 17.73 nm. This could be due to the large physical size (12.7 nm) of the SNPs for G_t = 6 h. The conclusion drawn from these experiments is that the coating process is independent of G_t, while it strongly depends on the nucleation and growth temperatures.

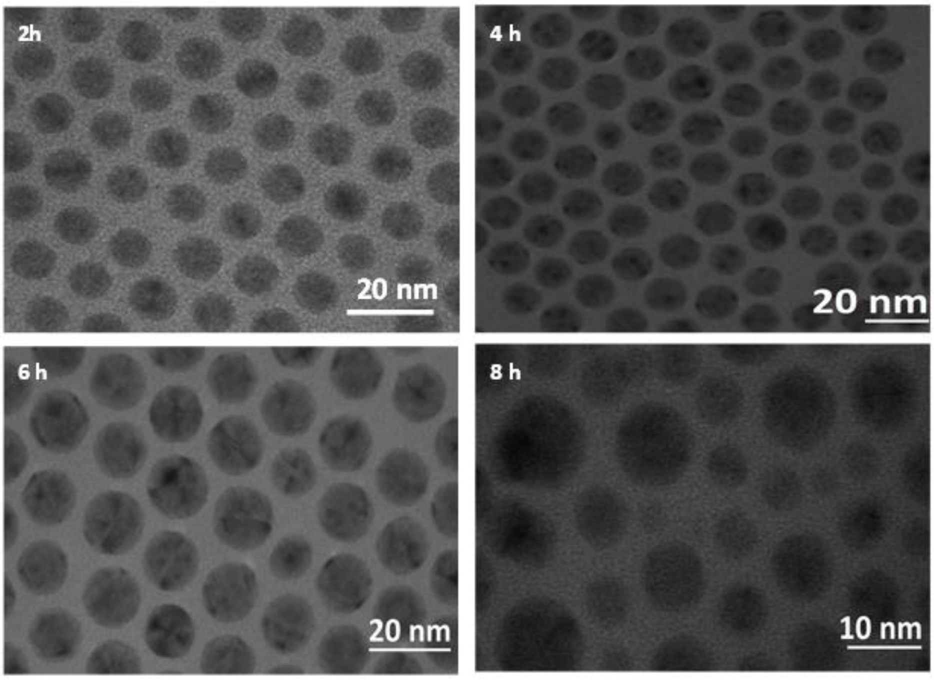

Fig. 3.28 TEM micrographs of SNPs prepared at different growth time.

The UV-visible absorption spectra of SNPs prepared with different growth time (0.5 h - 8 h) is shown in **Fig. 3.29**. A single plasmon resonance band is observed which is centred at 397 nm - 408 nm. No other spectral signatures are found in the UV-visible spectra. It means that the morphology of SNPs, which is spherical in this case, is independent of growth time.

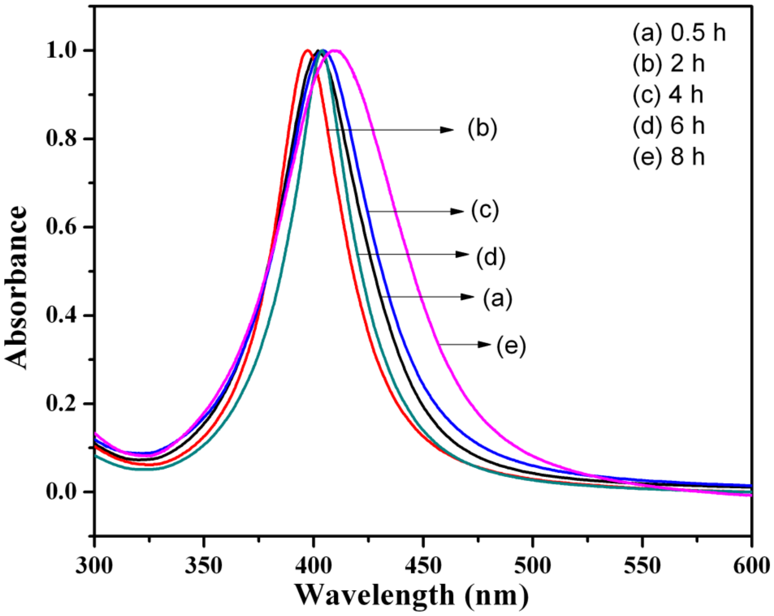

Fig. 3.29 UV-visible spectra of SNPs dispersed in n-hexane as a function of growth time. A single SPR band is observed in each spectrum which is centred at 404 nm, confirming the spherical morphology of nanostructures.

High resolution transmission electron microscopy image of the SNPs prepared with optimized conditions, (i.e. concentration of reducing cum capping agent-oleylamine = 15 mM, nucleation temperature = 200 °C, nucleation time = 30 min, growth temperature = 150 °C and growth time = 4 h) is shown in **Fig. 3.30**. Monodispersed nanoparticles with well-defined spherical morphology can be observed in **Fig. 3.30**. The top inset shows the specific area electron diffraction (SAED) image of SNPs. Four well distinguish rings can be observed in the SAED pattern, which confirms the polycrystalline nature of the nanoparticles. The bottom inset is the high resolution lattice fringe image of a silver nanoparticle. The average inter-planner spacing is 0.162 nm corresponding to (220) lattice plane. Silver nanoparticle is made up of six domains, which also confirms the polycrystalline nature of the particle.

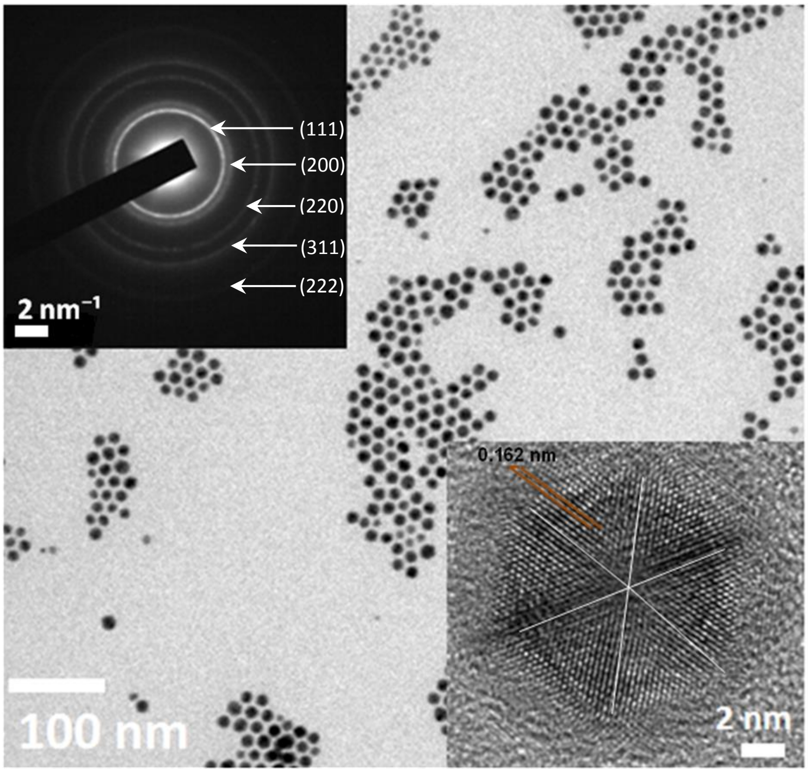

Fig. 3.30 HRTEM micrograph of SNPs. Inset (top) shows the specific area electron diffraction pattern (SAED) and inset (bottom) shows the lattice fringe image of a single silver nanoparticle.

The inhibition of delayed nucleation during growth, in other words, the complete separation of nucleation and growth, is critical for the successful synthesis of monodispersed nanoparticles [18]. Although the mechanism leading to monodispersed SNPs presented here is not completely clear but the experimental observations suggest that the formation of SNPs follows the classical condensation mechanism during the growth process [18]. SNPs were built up by the stacking of atomic species of Ag. These atomic species were derived from the chemical reduction of $AgNO_3$ by OA. The clustering of the Ag atoms gives numerous nuclei that are saturated in the reaction medium and aggregated into SNPs. The solubility of the nuclei in the dispersion decides the stage at which the nucleation stops and the aggregation of the nuclei dominates the growth process [18]. The particles cannot be formed if the nuclei are not saturated in the dispersion medium. Above the saturation threshold, the aggregation of the nuclei becomes spontaneous until the particles sinter from the dispersion.

3.2.3 Phase Transfer

OA coating on SNPs renders them hydrophobic. To investigate the antimicrobial properties of SNPs, they need to be dispersible in water/biological media. Hence as-synthesized hydrophobic SNPs were phase transferred from n-hexane to water by the facile phase transfer protocols [19]. Pluronic F-127 was used as phase transfer ligand. Pluronic F-127 has two hydrophilic A chains of poly ethylene oxide (PEO) and one hydrophobic B chain of poly propylene oxide (PPO) in an ABA configuration. For the phase transfer of SNPs; 20 mL, 0.2 M aqueous solution of pluronic F-127 was mixed with equal volume of stock solution of SNPs in n-hexane in a 100 mL beaker. It was covered with a perforated aluminium foil to control the evaporation of n-hexane. The mixture was magnetically stirred until the n-hexane evaporates completely. To confirm the phase transfer of SNPs, fresh n-hexane was poured on the aqueous solution of SNPs. On successful phase transfer, both aqueous and organic phases would remain immiscible (**Fig. 3.31**). The added organic phase was isolated from the aqueous phase by centrifugation. The phase transferred aqueous dispersion of silver was preserved at 4 °C.

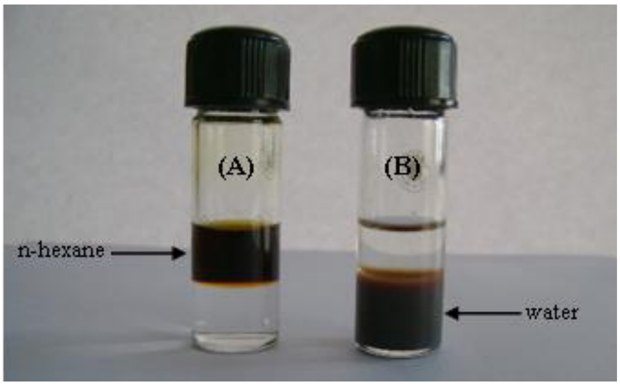

Fig. 3.31 SNPs (A) before phase transfer (dispersion in hexane) and (B) after phase transfer (dispersion in water).

Reduction of $AgNO_3$ by OA produces SNPs with hydrophobic surfaces. OA is chemically bound on the surface of silver due to the formation of Ag – N bond [25], which keeps them hydrophobic and dispersible in hexane. Pluronic F-127 is used to transfer hydrophobic SNPs into aqueous medium. Pluronic F-127 is made up of two hydrophilic A chains of poly ethylene oxide (PEO) and one hydrophobic B chain of poly propylene oxide (PPO). The transfer mechanism (**Fig. 3.32**) shows pluronic replaces the original OA ligand on the surface of nanoparticles and become the new ligand. Hydrophilic nature of PEO segments of pluronic-capped nanoparticles transfer them into the aqueous medium and keeps them dispersible in water. By exchanging the original ligands (oleylamine) with block-co-polymer pluronic F-127, the transferred nanoparticles exhibited good stability in water, even after being washed with hexane.

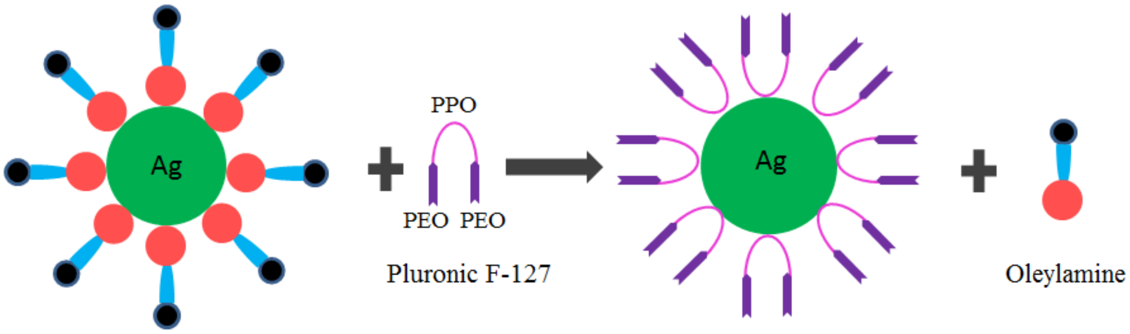

Fig. 3.32 Schematic representation of phase transfer of hydrophobic SNPs into hydrophilic using pluronic F-127.

UV-visible spectra of as-synthesized (in n-hexane) and phase transferred SNPs are shown in **Fig. 3.33**. A single SPR peak was observed both before and after the phase transfer. The spectral band after the phase transfer shifts to higher wavelength, i.e. a red shift is observed after the phase transfer. This might be because of difference in surface adsorbed species on SNPs before and after the phase transfer. The presence of single SPR band after the phase transfer indicates that the particle morphology is not affected by phase transfer. According to the Mie’s theory, only a single SPR band is expected in the absorption spectra of spherical metal nanoparticles, whereas anisotropic particles could give two or more SPR bands depending on the shape of the particles [26]. In this case, a single SPR band is observed, indicating that SNPs are spherical. Further, phase transfer does not alter the shape of the SPR band, which excludes the possibility of formation of agglomerates during the phase transfer. Reduction in the intensity of SPR band for the phase transferred SNPs is due to their lower concentration.

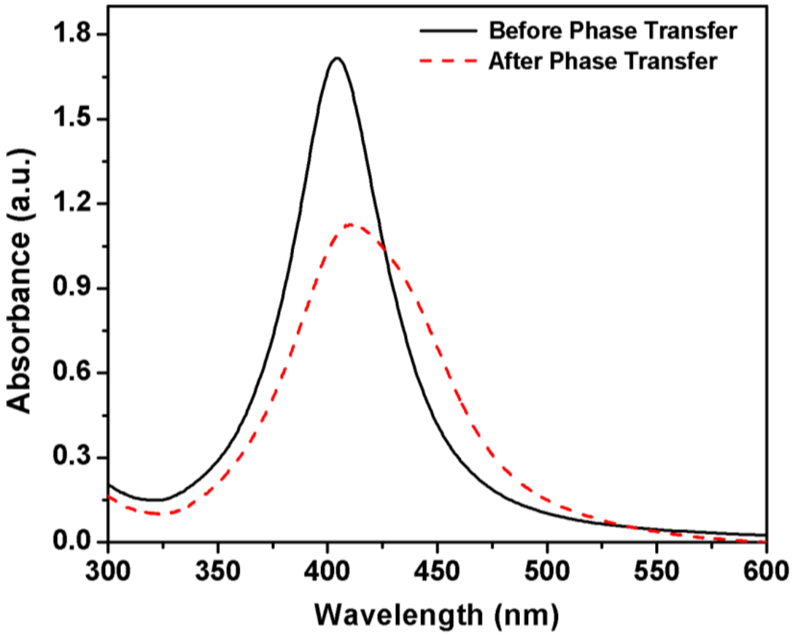

Fig. 3.33 UV-visible spectra of SNPs (—) before and (- - -) after the phase transfer. A single SPR peak centred at 404 nm indicating the spherical geometry of nanoparticles. The SPR band is red shifted to 413 nm after the phase transfer.

Hydrodynamic particle size distribution histograms of SNPs before and after the phase transfer are shown in **Fig. 3.34**. Each histogram is fitted with lognormal particle size distribution function and from the fitting, the mean hydrodynamic size and polydispersity indices are determined. The hydrodynamic size of SNPs before the phase transfer is 9.2 ± 0.06 nm and after the phase transfer, it is 59.1 ± 0.14 nm. The size difference of ≈ 50 nm between as-synthesized and phase-transferred nanoparticles is doubled compared to the micellar size (23 nm) of pluronic [27].

Fourier transform infrared spectroscopy was employed to understand the surface functionalization of SNPs before and after the phase transfer. FTIR spectra of SNPs before and after the phase transfer are shown in **Fig. 3.35** and analysed in **Table 3.1**. Only the salient features of each spectrum are described here. In case of oleylamine capped SNPs (before phase transfer), the bands at 2850 and 2915 cm^{-1} originate from the symmetric and asymmetric stretching vibrations of C – H [28]. The broad absorption band centred at 3432 cm^{-1} is attributed to the N – H stretching vibrations [28]. An additional band appeared at 1591 cm^{-1} is due to the asymmetric stretching of the Ag – N, suggesting that – NH_2 group of OA coordinates with the Ag on the surface of the SNPs [9]. In the FTIR spectra of phase transferred SNPs, bands at 949 and 1113 cm^{-1} are observed. These bands correspond to the CH_2 rocking and C – O – C stretching vibrations of pluronic F-127 [29]. The bands at 1543 and 1638 cm^{-1} are due to the aromatic rings in pluronic F-127. Absorption bands corresponding N – H vibrations and Ag – N present in the FTIR spectra of SNPs before the phase transfer are missing in the FTIR spectrum of SNPs after the phase transfer. This observation strengthens our claim that OA is replaced by block copolymer, pluronic F- 127 during the legend exchange reaction [9].

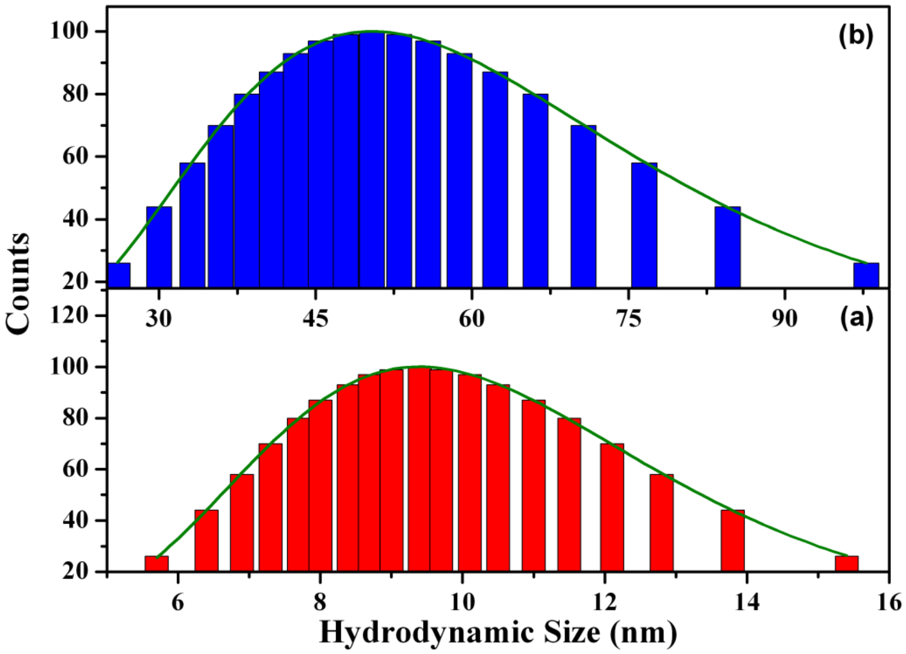

Fig. 3.34 Hydrodynamic size distribution histograms of SNPs (a) before and (b) after the phase transfer. Each histogram is fitted with lognormal particle size distribution function.

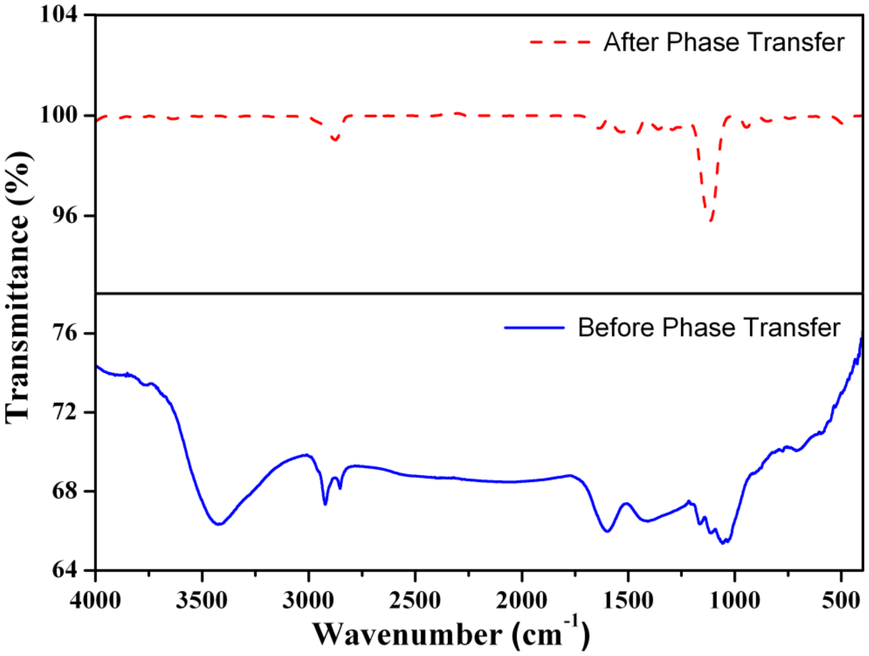

Fig. 3.35 FTIR spectra of SNPs before and after phase transfer.

Table 3.1 Band Assignments of FTIR spectra (**Fig. 3.35**) of SNPs before and after phase transfer.

SNPs	Band position (cm^{-1})	Description
Before phase transfer	1591	Asymmetric stretching of the Ag – N
	2850	Symmetric stretching vibrations of C – H bonds
	2915	Asymmetric stretching vibrations of C – H bonds
	3432	N – H stretching vibrations
After phase transfer	949	CH_2 rocking vibration
	1113	C – O – C stretching vibration
	1249	CH_2 twist
	1294	CH_2 twist
	1362	CH_2 wag
	1464	$= CH_2$ bending
	1543	Aromatic C = C stretching
	1638	Aromatic C = C stretching
	2874	Symmetric stretching of C – H

3.3 Synthesis of Copper Nanoparticles (CNPs)

3.3.1 Materials

Copper (II) chloride dihydrate (≥ 99%), polyvinylpyrrolidone (PVP) (average mol. wt. 10,000) and sodium borohydride ($NaBH_4$) (≥ 98%) were obtained from Sigma Aldrich. L-ascorbic acid (AA) was procured from Merck. Aqueous solutions were prepared in Millipore ultrapure water ($\rho = 18.2$ MΩ). All chemicals were used as-received without purification.

3.3.2 Synthesis Process

Synthesis of CNPs was carried out by chemical reduction at elevated temperatures. CNPs were prepared by reducing copper (II) chloride with strong ($NaBH_4$) and weak (L-ascorbic acid) reducing agents. To achieve fast and homogenous nucleation of CNPs, aqueous solution of copper (II) chloride was added into the preheated mixture of reducing ($NaBH_4$ + L-ascorbic acid) and capping (PVP) agents. The role of reducing and capping agent on the product quality of CNPs has been evaluated in terms of their size and size distribution, crystal phase and morphology. It has been found that all the three components, i.e. PVP, $NaBH_4$ and L-ascorbic acid were essential for the synthesis of stable CNPs. In the absence of one of these components, either CNPs did not form or were not stable. Schematic representation of protocols followed for the synthesis of CNPs is presented in **Fig. 3.36**.

3.3.2.1 Effect of Weak Reducing Agent (L-ascorbic acid)

Effect of weak reducing agent (L-ascorbic acid) on the formation of CNPs, their stability and quality in terms of size and size distribution have been investigated by preparing series of samples with 0-15 mM L-ascorbic acid. In brief, 25 mL aqueous solution of PVP (10 mM) was prepared. To this, 15 mL aqueous solution of NaBH$_4$ (10 mM) and AA (0 mM-15 mM) was added under continuous magnetic stirring. The mixture was heated to 80 °C at a rate of 3 °C/min. 10 mL aqueous solution of copper chloride (1.16 mM) was added drop-wise. The solution was heated at 80 °C till the color of mixture turned bright red. This intense red color is due to the surface plasmon resonance (SPR) of CNPs. The mixture was cooled to 25 °C. The sample was collected by centrifugation for 10 min at a relative centrifugal force (RCF) of 15471 x g (12000 rpm). Well dispersed CNPs were obtained as supernal and larger cluster of CNPs, if any, are discarded as sediment.

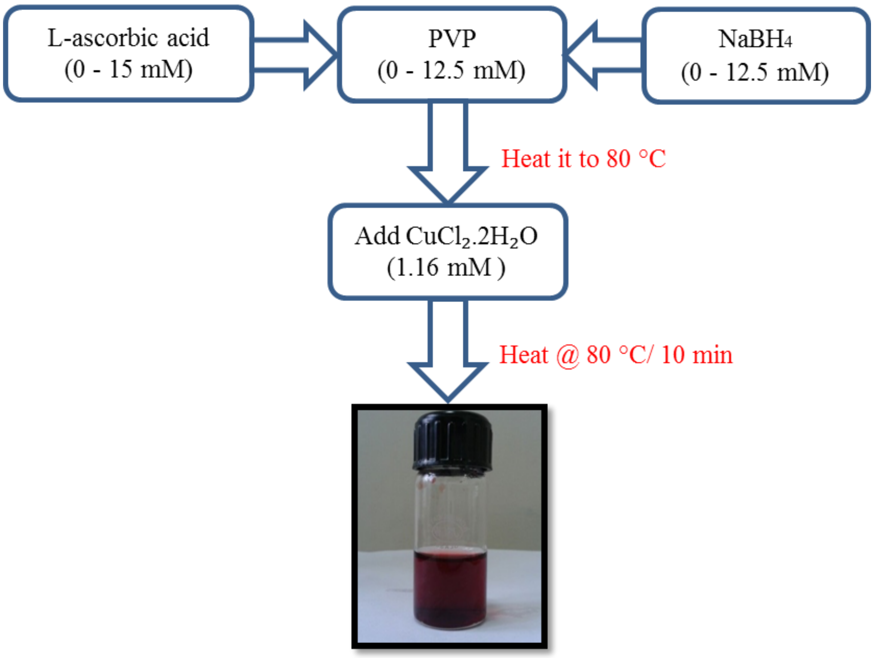

Fig. 3.36 Schematic presentation of protocols followed for the synthesis of colloidal CNPs. Image at the end of the flow chart shows intense red color due to the surface plasmon resonance in copper nanoparticles confirming their formation.

Effect of weak reducing agent (L-ascorbic acid) on the formation of CNPs was evaluated by UV-visible spectroscopy. **Fig. 3.37** shows the UV-visible spectra of CNPs prepared with different L-ascorbic acid concentration (0-15 mM).

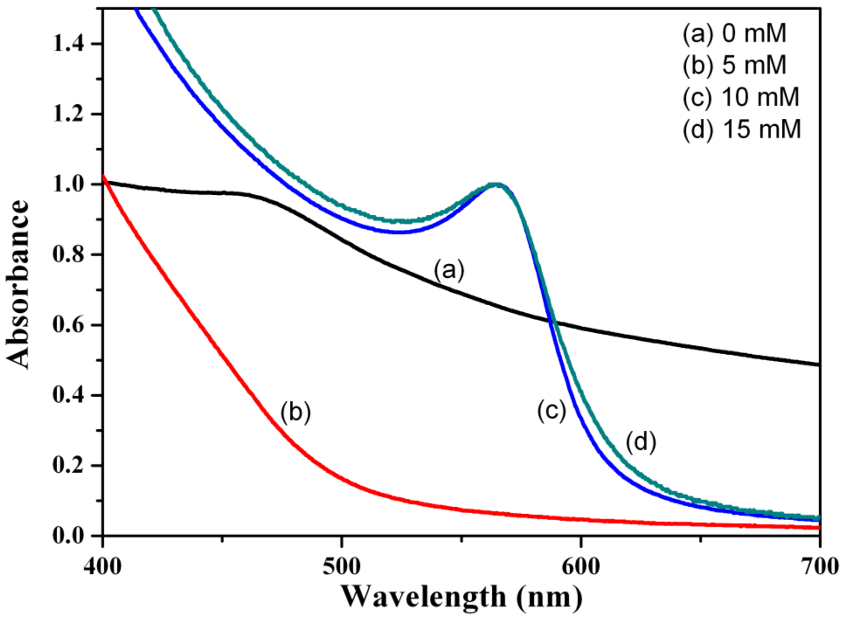

Fig. 3.37 UV-visible spectra of as-synthesized CNPs prepared with different concentrations of L-ascorbic acid ($NaBH_4$ and PVP = 10 mM).

For 0 mM AA, the SPR band is observed at 450 nm, a typical characteristic of Cu_2O nanoparticles [30]. No SPR peak corresponding to metallic phase of CNPs was observed, which is expected at 575 nm [30]. This means AA is essential for the synthesis of pure metallic phase of CNPs. In case of 5 mM AA, no SPR peak was observed in the UV-visible spectra, indicating the formation of larger size particles, as large size metallic particles do not show plasmonic characteristics [31, 32]. A single plasmon resonance band was observed at 566 nm when AA concentration is ≥ 10 mM. No SPR band below 500 nm was observed. This means as-synthesized nanoparticles did not possess any oxide phases (CuO or Cu_2O) as absorption maximum corresponding to CuO and Cu_2O phases would have been observed at 370 nm and 450 nm, respectively [30]. Observation of single SPR peak (at 566 nm) also indicates that the synthesized CNPs have spherical morphology as multiple SPR bands are expected from asymmetric metal nanoparticles [23, 33].

Hydrodynamic particle size distributions of CNPs prepared with different AA concentrations (0-15 mM) are shown in **Fig. 3.38**. Each histogram is fitted with lognormal particle size distribution function [21] and from the fit, mean hydrodynamic size and polydispersity indices are determined. For 0 mM AA, the mean hydrodynamic size and polydispersity index of as-synthesized nanoparticles are 393.7 nm and 0.44, respectively. With increase in AA concentration, the mean hydrodynamic size decreases and saturates at 17.4 nm at 10 mM AA (**Fig. 3.39**). The minimum in polydispersity index (0.13) was also observed for 10 mM AA.

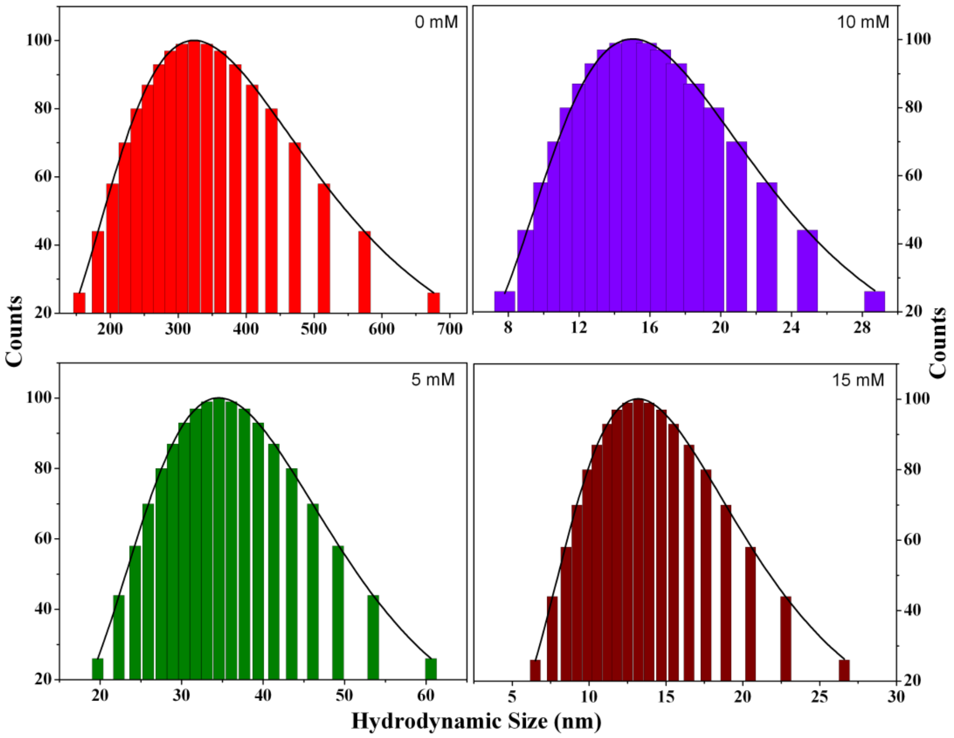

Fig. 3.38 Size distribution histograms of CNPs prepared with different concentration of L-ascorbic acid ($NaBH_4$ and PVP = 10 mM).

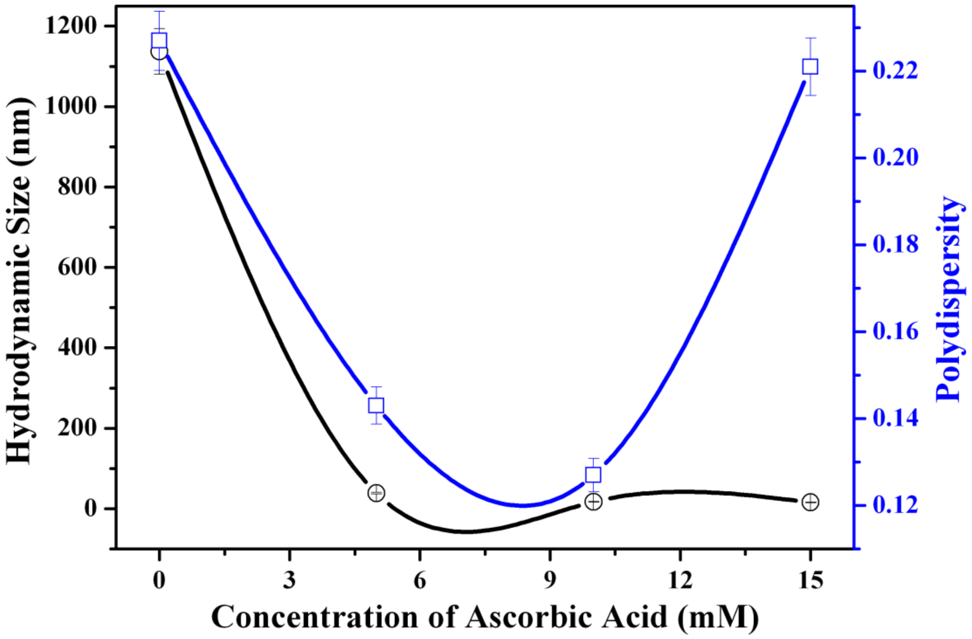

Fig. 3.39 Variation in hydrodynamic size (o) and polydispersity index (□) of CNPs as a function of L-ascorbic acid ($NaBH_4$ and PVP = 10 mM) concentration.

Ascorbic acid has a dual functionality. It is acting as reducing and capping agent, which helps in controlling the particle size and its distribution by electrostatic stabilization of nanoparticles. From the results of UV-visible and photon correlation spectroscopy, it is concluded that 10 mM of AA is the optimum concentration required to prepare ultra-small, stable, single phase CNPs.

3.3.2.2 Effect of Strong Reducing Agent ($NaBH_4$)

To understand the effect of strong reducing agent on phase formation of CNPs, their size and size distribution; five samples were prepared with 0-12.5 mM $NaBH_4$. PVP and AA concentration were kept constant at 10 mM. Rest of the synthesis protocols were same as described in section 3.3.2.

Fig. 3.40 shows the UV-visible spectra of CNPs prepared with different $NaBH_4$ concentrations (0-12.5 mM). No SPR band is observed for low $NaBH_4$ concentration (≤ 5 mM). There could be two possible reasons behind the absence of SPR bands in the UV-visible spectra of CNPs prepared with lower (≤ 5 mM) $NaBH_4$ concentration. Either no phase of copper ($Cu/CuO/Cu_2O$) is formed or their particle size is larger than the excitonic radius of copper.

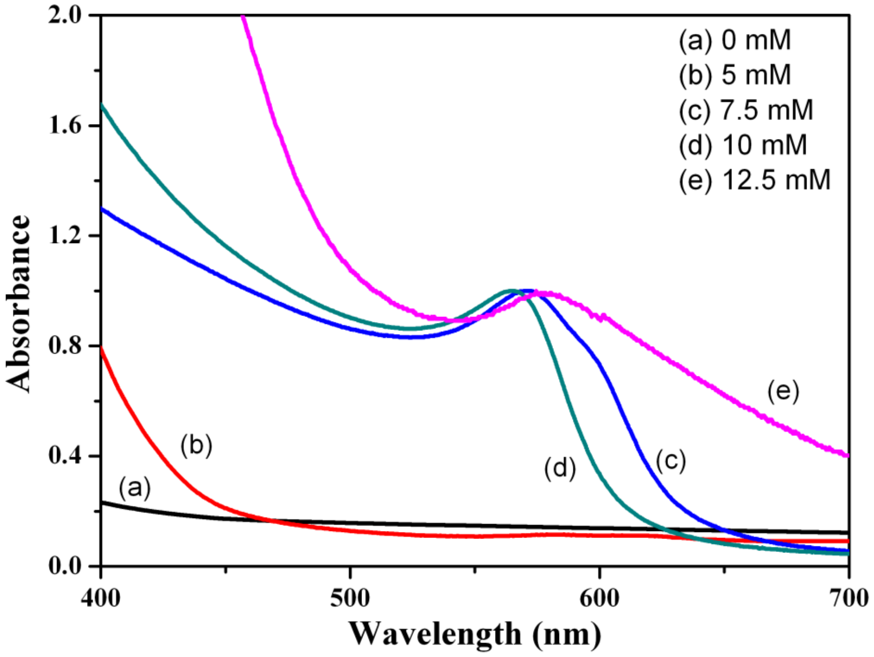

Fig. 3.40 UV-visible spectra of as-synthesized CNPs prepared with different concentrations of $NaBH_4$ (L-ascorbic acid and PVP = 10 mM).

To confirm this, photon correlation spectroscopy was employed. **Fig. 3.41** shows the hydrodynamic size distribution histograms of CNPs prepared at different $NaBH_4$ concentration (0-12.5 mM). At low $NaBH_4$ concentration (≤ 5 mM), the hydrodynamic size of CNPs is very large (> 100 nm). For 0 mM $NaBH_4$, the hydrodynamic size is 388.6 nm and at 5 mM, it is 127 nm. With increase in $NaBH_4$ concentration, the hydrodynamic size of CNPs decreases. This might be due to the change in nucleation density. At low $NaBH_4$ concentration, the nucleation density might be low, which leads to the growth of fewer number of larger size particles. As $NaBH_4$ concentration increases, the nucleation density increases and hence the hydrodynamic size decreases.

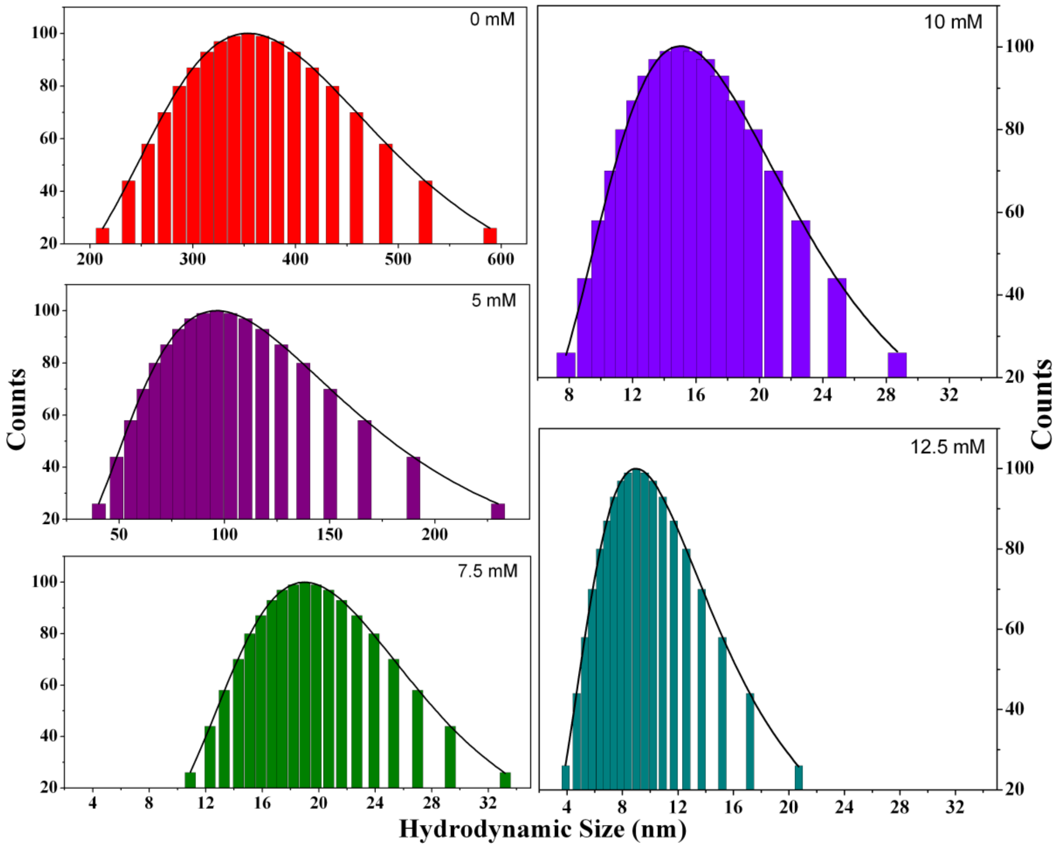

Fig. 3.41 Size distribution histograms of CNPs prepared with different concentration of $NaBH_4$ (L-ascorbic acid and PVP = 10 mM).

Fig. 3.42 shows the variation in hydrodynamic size and polydispersity index of CNPs prepared with different concentration of $NaBH_4$. Hydrodynamic size is minimum (11.6 nm) for 12.5 mM of $NaBH_4$ but the polydispersity is high (0.31). Minimum in polydispersity (0.13) of CNPs is observed when $NaBH_4$ is 10 mM. From the mean hydrodynamic size and polydispersity data of CNPs, it is concluded that 10 mM of $NaBH_4$ is the optimum concentration for the preparation of nearly monodisperse ultrafine

CNPs. Further, a single SPR band centred at 566 nm is observed when $NaBH_4$ concentration is 10 mM. Single SPR band centred at 566 nm originates from the spherical single phase metallic CNPs whose physical size is smaller than the excitonic radius of copper. For $NaBH_4$ concentration > 10 mM, the SPR band gets broaden and red shifts.

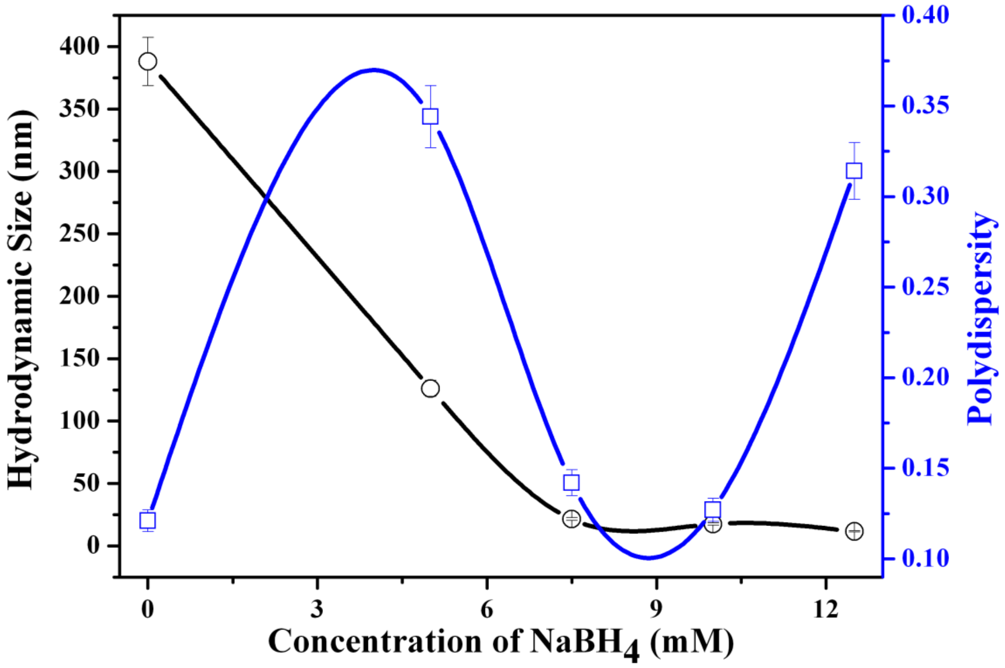

Fig. 3.42 Variation in hydrodynamic size (o) and polydispersity index (□) as a function of $NaBH_4$ (L-ascorbic acid and PVP = 10 mM) concentration.

3.3.2.3 Effect of Surfactant (PVP)

To investigate the effect of stabilizer, PVP on the quantity and quality of CNPs, a series of samples were prepared by varying the PVP concentration from 0-12.5 mM. Rest of the variables were kept constant as per the conditions of section 3.3.2. $NaBH_4$ and AA concentrations were 10 mM each.

Effect of concentration of reducing agent on the quality of nanostructures has been evaluated in terms of size and size distribution, crystal phase and morphology. It is observed that at least 2.5 mM of PVP is required to form metallic phase CNPs. UV-visible spectra of CNPs prepared with 0-12.5 mM PVP are shown in **Fig. 3.43**. No SPR is observed when nanoparticles are prepared in the absence of PVP. The SPR band is observed at 572 nm when PVP is 2.5 mM and it blue shifts to 566 nm when PVP ≥ 5 mM. The observation of single SPR band at 566 nm for PVP concentration ≥ 5 mM indicates that ultra-small single phase metallic CNPs are formed. No SPR band corresponding to oxide phases of copper are observed. This study reveals that to prepare ultra-small, spherical, plasmonic CNPs; at least 5 mM of PVP is essential.

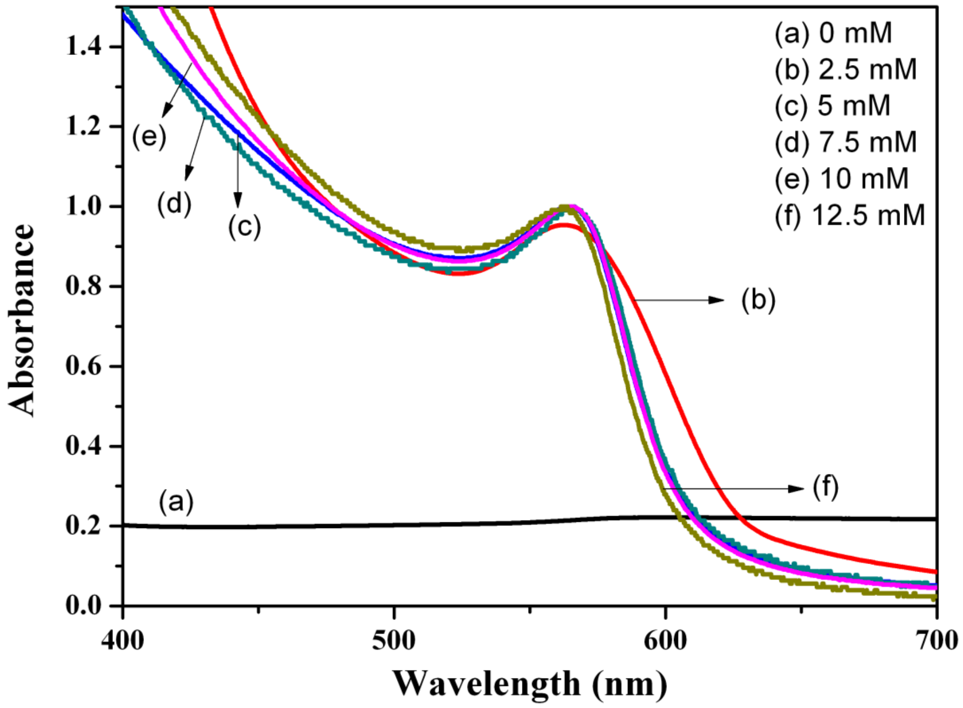

Fig. 3.43 UV-visible spectra of as-synthesized CNPs prepared with different concentrations of PVP (L-ascorbic acid and $NaBH_4$ = 10 mM).

Fig. 3.44 shows the hydrodynamic size distribution histograms of CNPs prepared with different concentration of PVP while keeping AA and $NaBH_4$ concentration constant at 10 mM. Without PVP (0 mM), the hydrodynamic size and polydispersity index of CNPs are 313 nm and 0.26, respectively. The hydrodynamic size of CNPs decreases as PVP concentration increases and levels off when the concentration is ≥ 7.5 mM (**Fig. 3.45**). Lower PVP concentration in the medium during the synthesis of CNPs cannot control the aggregation and hence results in the clusters of CNPs with higher size and broader size distribution. As the concentration of PVP increases, it decreases the tendency of agglomeration of CNPs by increasing the electrostatic repulsion between them. The average hydrodynamic size is 17.4 nm when PVP concentration is 10 mM. At this concentration, each nanoparticle is protected against aggregation by a thin layer of PVP. For CNPs prepared with 10 mM PVP, both hydrodynamic size (17.4 nm) and polydispersity (0.13) are minimum. Synthesis of CNPs with 10 mM PVP produces single phase nanoparticles with smaller size and narrow size distribution.

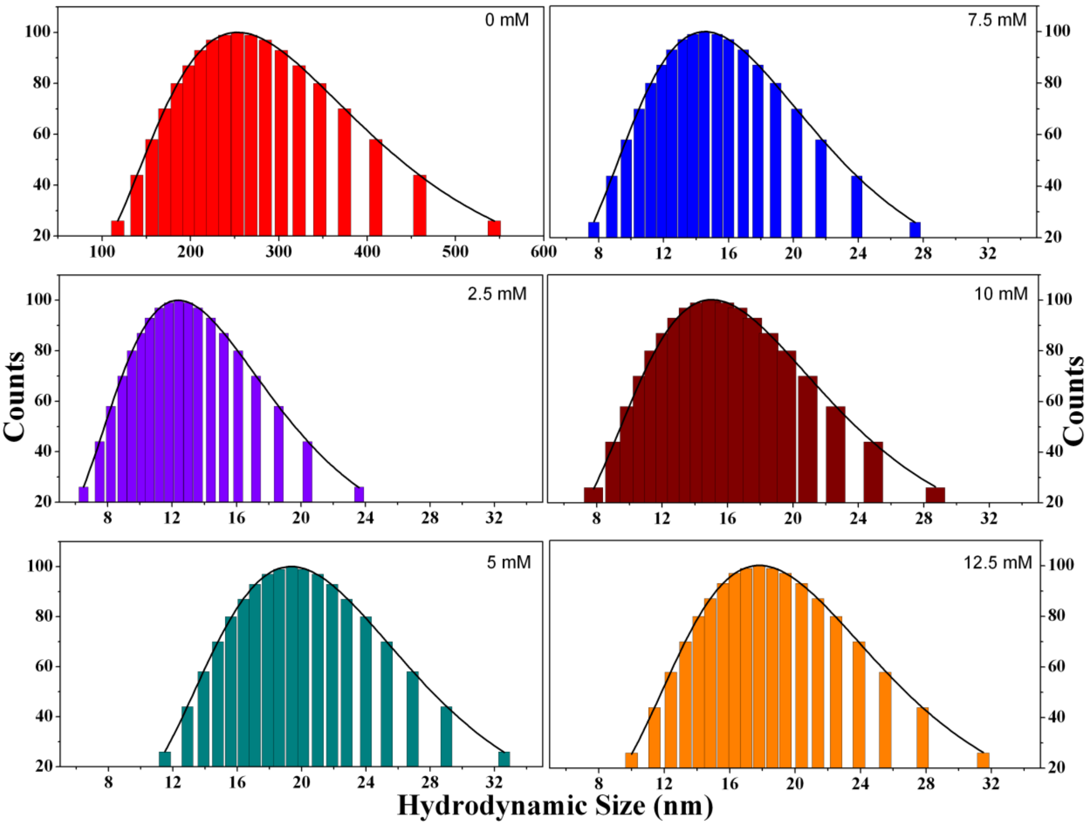

Fig. 3.44 Size distribution histograms of CNPs prepared with different concentration of PVP (L-ascorbic acid and $NABH_4$ = 10 mM). Each histogram is fitted with lognormal particle size distribution function.

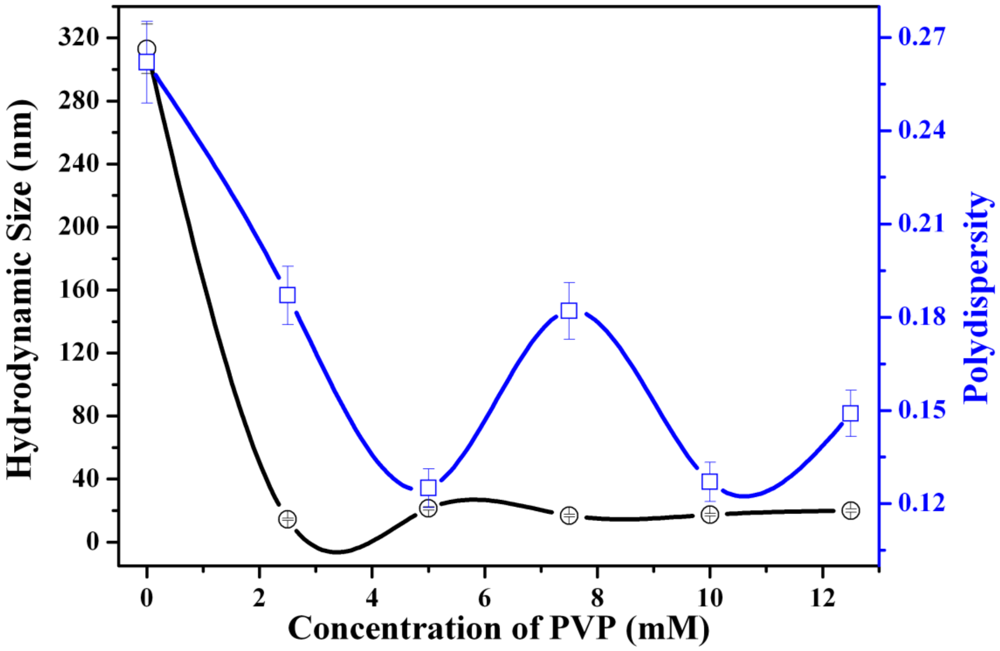

Fig. 3.45 Variation in hydrodynamic size (o) and polydispersity index (□) as a function of PVP (L-ascorbic acid = $NABH_4$ = 10 mM) concentration.

Optimized conditions to prepare uniform, ultra-small, spherical metallic single phase CNPs are summarized in **Fig. 3.36**. The optimized concentration of L-ascorbic acid, PVP and $NaBH_4$ is 10 mM, each. The X-ray diffraction pattern of as-synthesized CNPs prepared with 10 mM each of PVP, $NaBH_4$ and AA is shown in **Fig. 3.46**. X-ray diffractogram shows three distinct diffraction peaks corresponding to FCC structure of copper. The indexed peaks matched well with the PCPDF card no. 04-0836 of copper. The broadening of X-ray diffraction peaks shows that the as-synthesized CNPs are very small. No peak corresponding to oxide or any other impurity phases of copper is observed in the diffractogram. The synthesis protocols developed here produces single phase metallic CNPs directly in air without any secondary oxide phase. CNPs are stable against both the aggregation and oxidation.

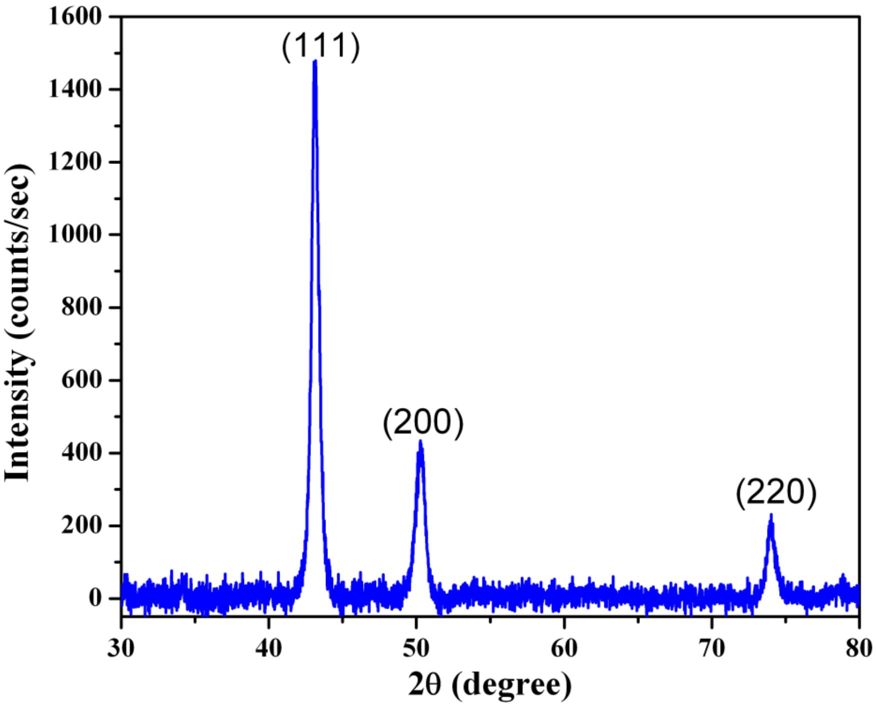

Fig. 3.46 X-ray diffraction pattern of CNPs prepared under optimized condition (i.e. concentration of PVP = $NaBH_4$ = L-ascorbic acid = 10 mM).

Fig. 3.47 shows the TEM micrographs of CNPs prepared under optimized conditions. As seen in the micrograph (**Fig. 3.47(a)**), CNPs formed a macromolecule with needle like morphology. Similar self-assembly for silver nanoparticles is reported by Li et al [34]. The macromolecule formed by the self-assembly of ultra-small CNPs is very large (≈ 500 nm in length). **Fig. 3.47(b)** shows the magnified view of the encircled region of **Fig. 3.47(a)**. HRTEM image of the same region is also shown in **Fig. 3.47(c)**. Self-assembly of ultra-small CNPs each of 2 nm into hexagonal closed pack lattice can be seen in **Fig. 3.47(c)**, indicating the high quality of the synthesized product.

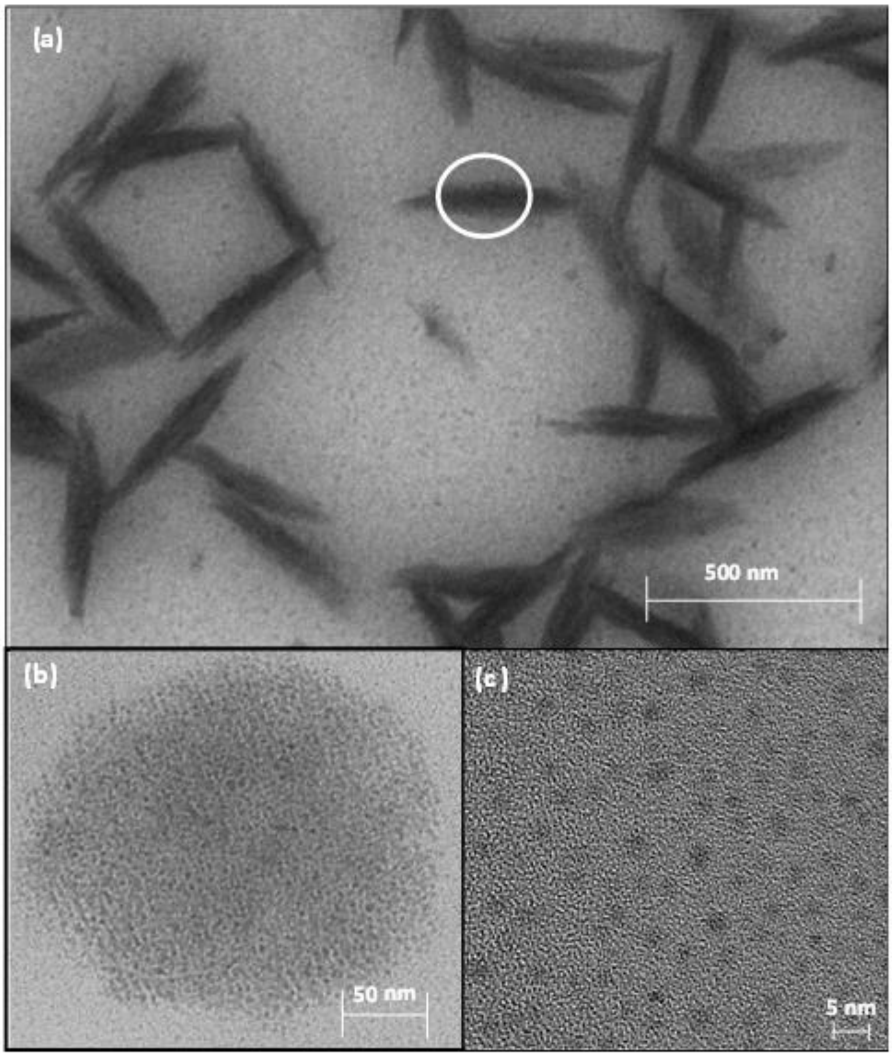

Fig. 3.47 (a) Low resolution TEM micrographs of CNPs prepared under optimized condition, (b) Magnified view of the encircled region of (a) and (c) HRTEM micrograph of CNPs.

3.3.3 Reduction Mechanism

To understand the formation of single phase metallic CNPs and its growth mechanism, large number of experiments were carried out. From these experiments, it is concluded that both the strong ($NaBH_4$) and the weak (AA) reducing agents are essential in addition to stabilizing agent (PVP) for the formation of stable, single phase metallic CNPs. This observation is contradictory to previous reports in which synthesis of stable metallic CNPs by reducing Cu^{2+} ions with either $NaBH_4$ or AA [33, 34] is reported. In the absence of any of the reducing agent (AA or $NaBH_4$), either copper oxide or unstable metallic Cu phase is formed, which is not stable and within minutes gets converted into one of the stable oxide (CuO or Cu_2O) phases.

To understand the phase formation, systematic investigation of the reduction of $CuCl_2$ was carried out. The reduction reaction was monitored in terms of color change as first indicator followed by UV-visible spectroscopy as the confirmation. It has been observed that PVP alone cannot reduce $CuCl_2$. This was evidenced from the fact that no color change was observed even if $CuCl_2$-PVP mixture was heated at 80 °C for long time (> 24 h). When 10 mM $NaBH_4$ was added into the reaction medium containing 1.16 mM $CuCl_2$ and 10 mM PVP at 80 °C; Cu^{+2} ions immediately reduced to Cu^0, which was evidenced from the red color of the solution. But within minutes, solution turned into dark green, indicating the oxidation of CNPs (tube - b in **Fig. 3.48**). The corresponding UV-visible spectrum is shown in **Fig. 3.49**. The SPR band positioned at 465 nm corresponds to the Cu_2O phase. The characteristic absorption maximum at 560 nm is missing indicating that no metallic copper is present in the sample.

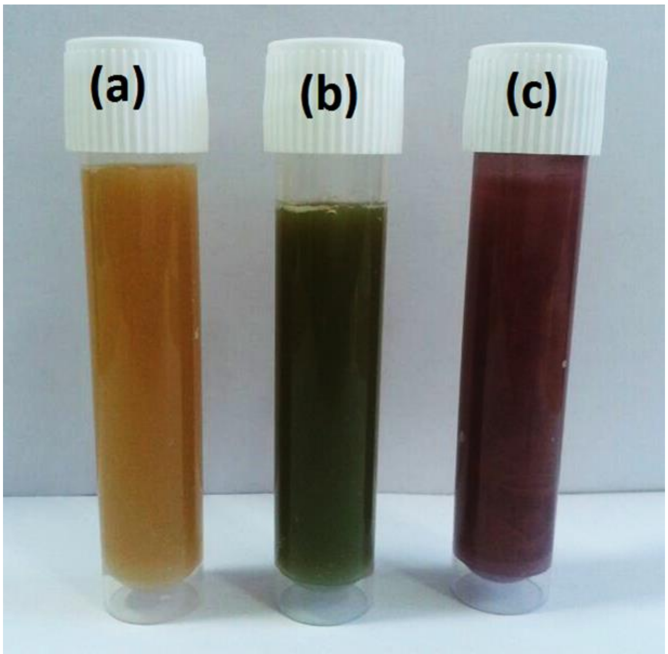

Fig. 3.48 The photographic view of as-synthesized nanoparticles with (a) 10 mM L-ascorbic acid and 0 mM $NaBH_4$; (b) 0 mM L-ascorbic acid and 10 mM $NaBH_4$ and (c) 10 mM L-ascorbic acid and 10 mM $NaBH_4$.

Now, when the same experiment was carried out with weak reducing agent, i.e. when $NaBH_4$ was replaced with 10 mM AA; in that case no evidence of formation of metallic Cu was observed as the final color of the solution remains dark yellow even after prolonged heating (tube - a in **Fig. 3.48**). The same is further confirmed from the UV-visible spectroscopy of the product (**Fig. 3.49**) where no signature of copper or any of their oxides phases are observed.

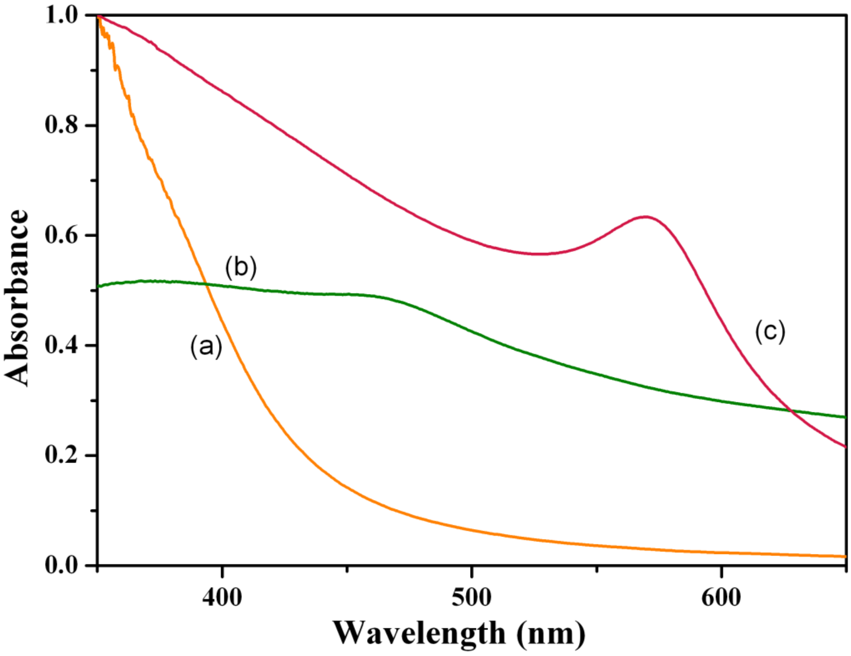

Fig. 3.49 UV-visible spectra of nanoparticles prepared with 10 mM PVP as stabilizing agent (a) 10 mM L-ascorbic acid and 0 mM $NaBH_4$; (b) 0 mM L-ascorbic acid and 10 mM $NaBH_4$; (c) 10 mM L-ascorbic acid and 10 mM $NaBH_4$.

In the next experiment, both the strong (10 mM $NaBH_4$) and weak (10 mM AA) reducing agents were added into the preheated $CuCl_2$-PVP mixture. Immediately upon addition, the solution color changes to dark red (tube - c in **Fig. 3.48**). On further heating, it did not change even if kept under oxidizing environment for long, indicating that Cu^{+2} has been reduced into stable Cu^0 phase. This is further confirmed by UV-visible spectroscopy (**Fig. 3.49**). A characteristic SPR band of CNPs centred at 560 nm is observed. No signatures of CuO or Cu_2O phases are observed in the spectra indicating that nanoparticles do not possess any oxide phase.

To understand the reduction mechanism, we did the serial addition of various components (PVP, $NaBH_4$ and AA) into the aqueous solution of $CuCl_2$. First 10 mM PVP was added into 1.16 mM $CuCl_2$ and heated to 80 °C. The UV-visible spectrum of the sample is shown in **Fig. 3.50**. For reference, the UV-visible spectrum of aqueous PVP is also shown in **Fig. 3.50**.

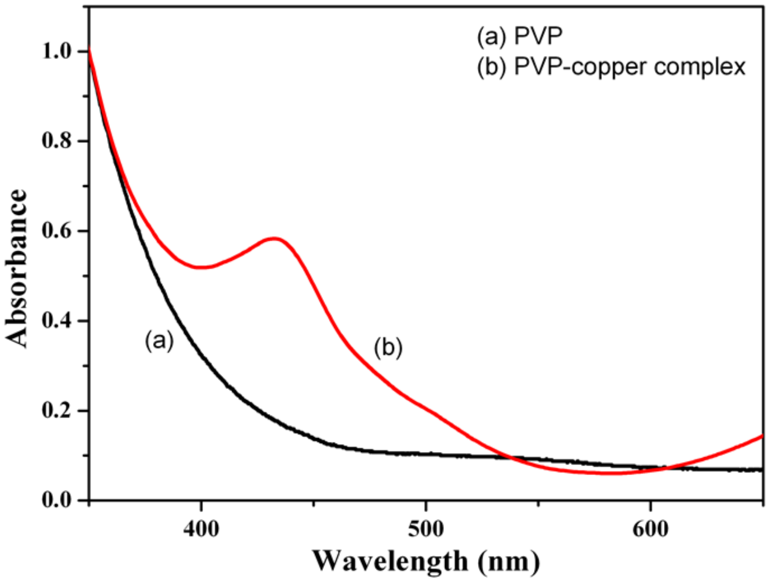

Fig. 3.50 UV-visible spectra of PVP and PVP-copper complex.

The UV-visible spectrum of $CuCl_2$ containing PVP shows a broad absorption band centred at 432 nm. This absorption band is ascribed to the formation of Cu-PVP complex. No such characteristic absorption maximum is observed for the aqueous PVP. Similar results are reported by Zhang et al. [35] when $AgNO_3$ was introduced into PVP solution. They have concluded that the observed absorption band was due to the formation of Ag-PVP complex. The formation of Ag-PVP complex reduces the reduction potential of Ag^{+1} [35]. It is proposed that Cu^{2+} ions make an organometallic complex with PVP via following chemical reaction.

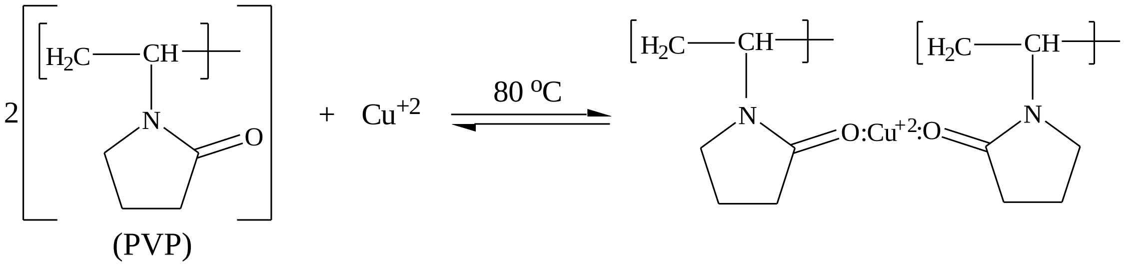

Step-I: Formation of PVP-Cu^{2+} complex.

This complex formation between PVP and Cu^{2+} is proposed on the basis of the structural features of PVP. PVP has polyvinyl skeleton with nitrogen and oxygen polar groups [36-38]. These polar groups form a coordinative interaction between PVP and Cu^{2+} ions by donating their lone pair electrons to Cu^{2+}. The organometallic complex formation between Cu^{2+} and PVP was previously reported by several groups [36-38]. The proposed mechanism of complex formation between Cu^{2+} and PVP is in line with that proposed by these groups [36-38]. When 10 mM $NaBH_4$ was added into the solution, it immediately reduced Cu^{2+} in the PVP- Cu^{2+} complex into Cu^0. $NaBH_4$ ionizes and forms a $(BH4)^-$ ligand, which then reacted with hydroxyl anions (Step-II). During this reaction, eight electrons are liberated from the hydroxyl ions. These electrons react with Cu^{2+} ions in the PVP-Cu^{2+} complex and reduce them to Cu^0.

$$NaBH_4 \longrightarrow Na^+ + (BH_4)^-$$

$$H_2O \longrightarrow H^+ + OH^-$$

$$(BH_4)^- + 8OH^- \longrightarrow B[(OH)_4]^- + 4H_2O + 8e^-$$

Step-II: Ionization of $NaBH_4$ and release of electrons from hydroxyl ions.

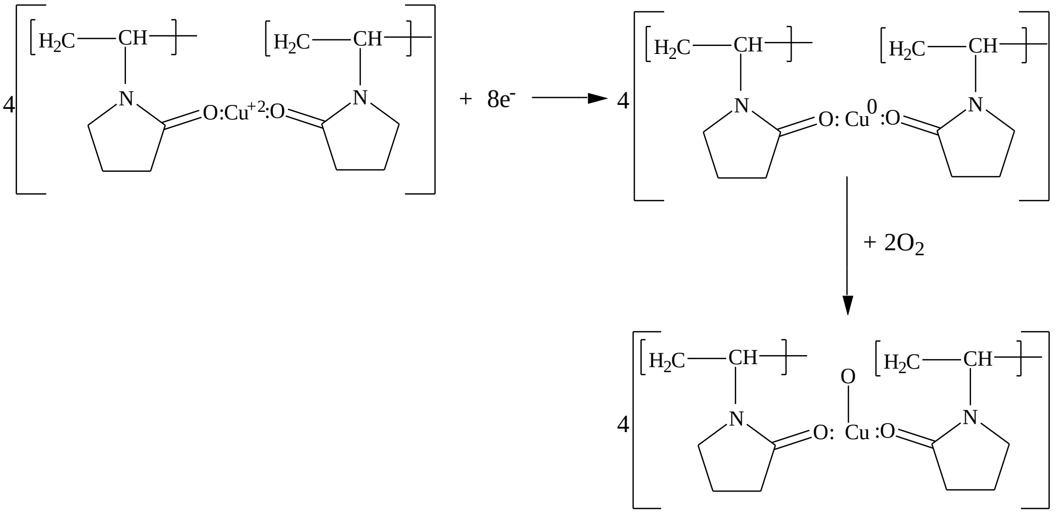

Step-III: Reduction of Cu^{2+} ions by $NaBH_4$ (product of step-II).

The execution of reduction reaction (Step-III) is evidenced from the change in the solution color from light yellow to dark red. Since, the product was in the oxidizing environment so within minutes it oxidized to Cu^{2+} and the solution color turned from red to dark green. Now, 10 mM AA was added into the solution (product of step-III). Within few minutes,

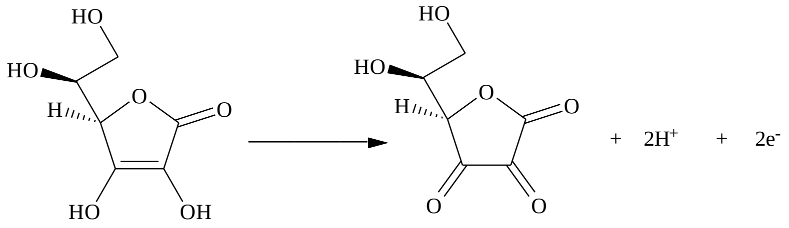

L-ascorbic acid Dehydroascorbic acid

Step-IV: Oxidation of L-ascorbic acid into dehydroascorbic acid.

the solution color again changes back from green to dark red. AA oxidizes into dehydroascorbic acid with a release of two electrons [39]. These electrons react with the oxidized product of step-III and reduce Cu^{2+} back into Cu^0. The oxidation by-product of AA, i.e. “dehydroascorbic acid” simulates a dynamic equilibrium (Step-V) around the Cu^0, which stabilizes CNPs against the oxidation [39]. The entire reduction mechanism is summarized as a schematic in **Fig. 3.51**.

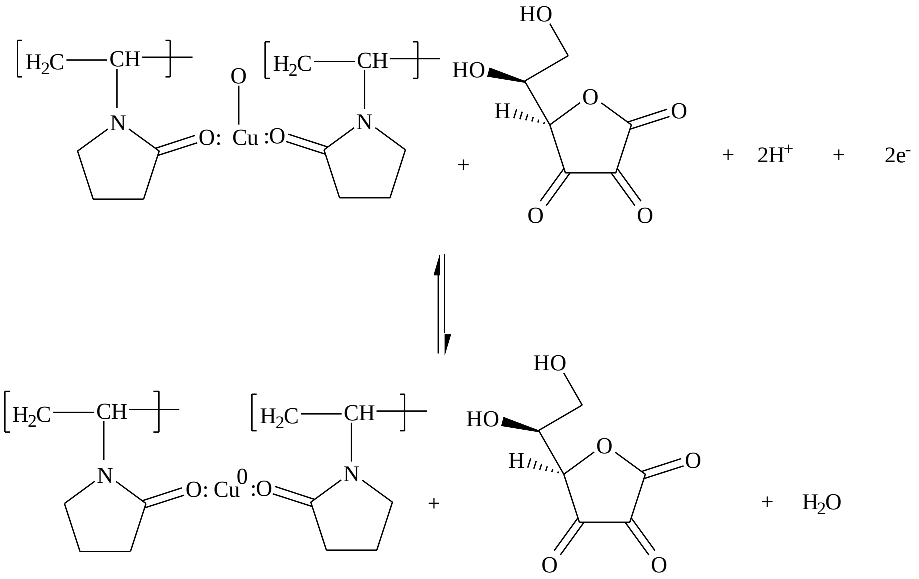

Step-V: Reduction of PVP-CuO complex by L-ascorbic acid and its stabilization by dehydroascorbic acid.

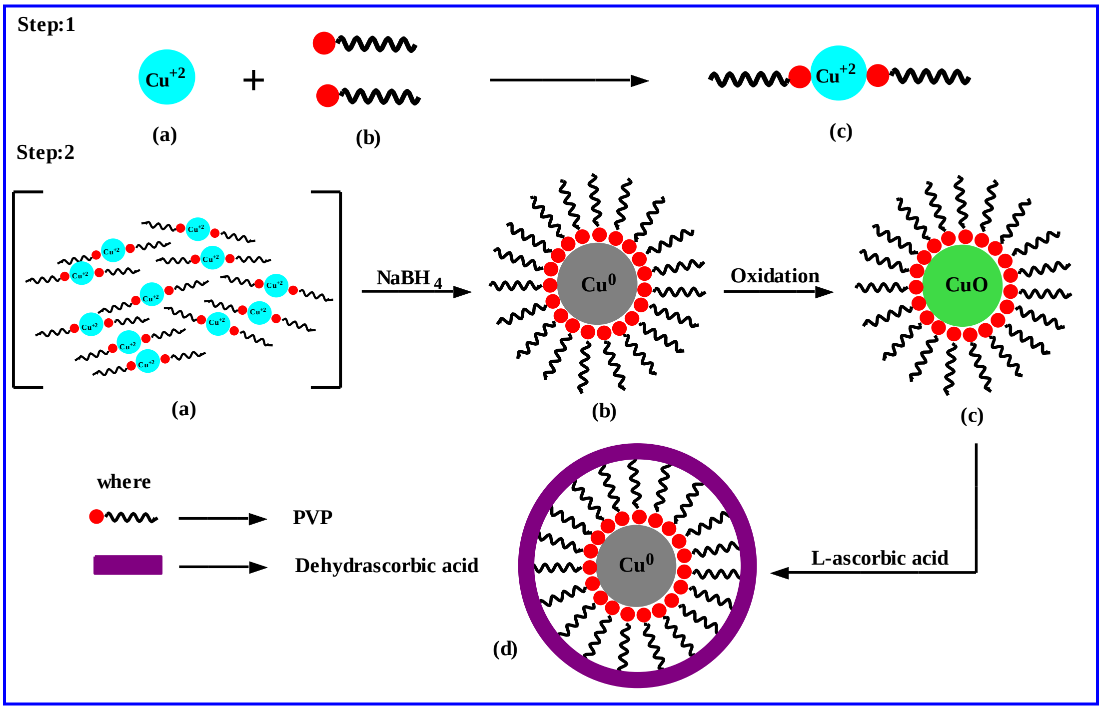

Fig. 3.51 Schematic representation of various steps that leads to the formation of ultra-small CNPs and its stabilization by dehydroascorbic acid.

3.3.4 Effect of Aging on the Stability of CNPs

Stability of the oxidation state of CNPs is very crucial. CNPs have a tendency to oxidise to CuO or Cu_2O phase. To evaluate the aging effect on the stability of CNPs against oxidation and aggregation, UV-visible and photon correlation spectroscopy were employed. **Fig. 3.52** shows the UV-visible spectra of as-synthesized and aged CNPs. The aging period was 120 days. Upon aging, no change in the position of SPR band (at 566 nm) corresponding to pure metallic phase of copper is observed. In addition, no signature of evolvement of CuO or Cu_2O phase is found in the UV-visible spectra of aged CNPs. This shows that CNPs are stable and resistant to oxidation in ambient condition.

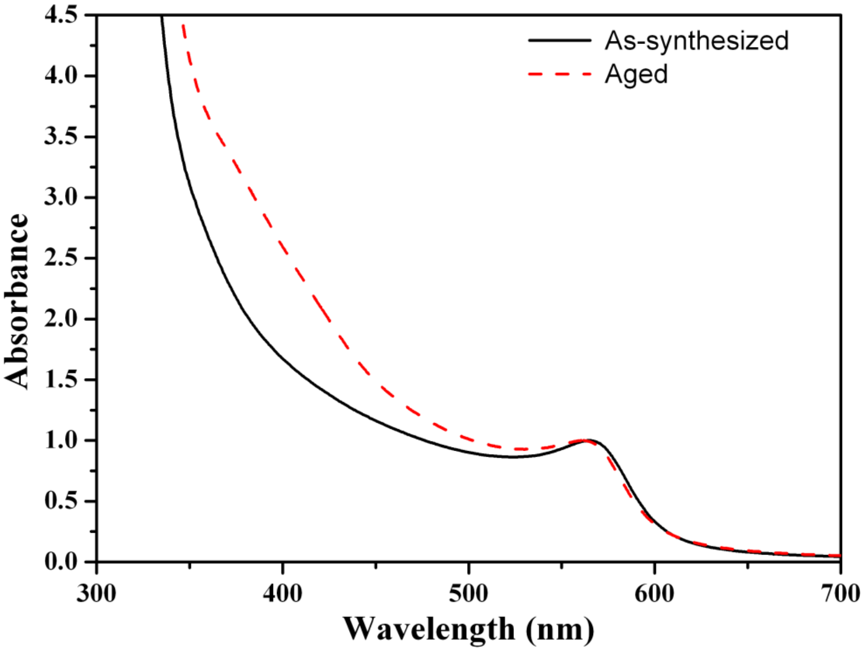

Fig. 3.52 UV-visible spectra of as-synthesized (—) and aged (- - -) CNPs. The aging period is 120 days. No signature corresponding to CuO or Cu_2O is observed in the aged sample indicating that CNPs are resistant to oxidation.

Particle size distribution histograms of as-synthesized CNPs prepared under optimized conditions and CNPs aged for 120 days are shown in **Fig. 3.53**. The mean hydrodynamic size of CNPs before and after the aging is 17.4 nm and 19.7 nm, respectively. The polydispersity index of as-synthesized CNPs is 0.13 and after aging, it increases to 0.16. Little increase in the hydrodynamic size and polydispersity of CNPs might be caused by formation of few aggregates of CNPs. Even though the CNPs are aged for a significantly large period of 120 days in ambient conditions, their particle size and polydispersity indices are almost constant revealing their impressive stability against aggregation.

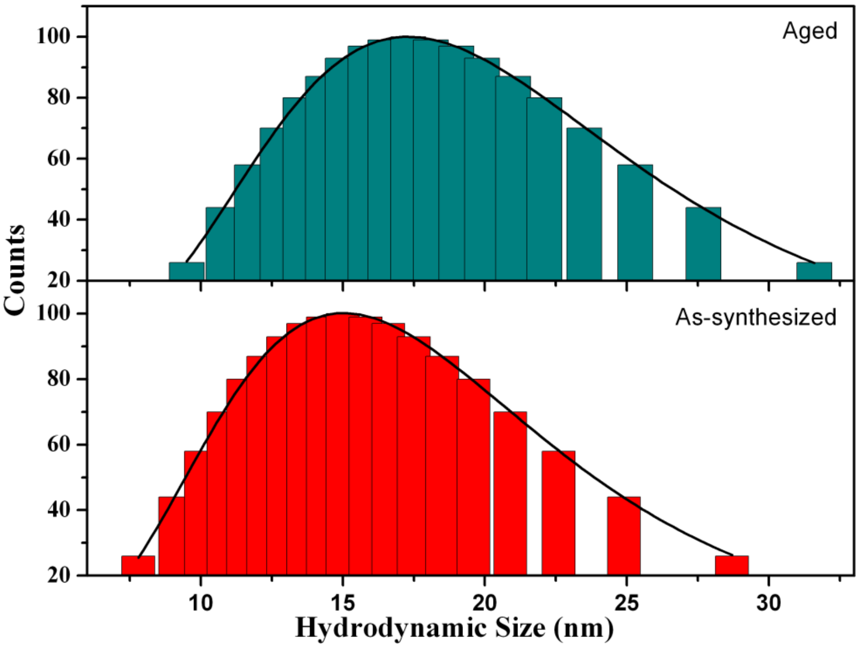

Fig. 3.53 Size distribution histograms fitted with lognormal particle size distribution function of as-synthesized (—) and aged (- - -) CNPs.

3.4 Synthesis of Titanium dioxide Nanoparticles (TNPs)

3.4.1 Materials

Titanium (IV) isopropoxide (97%) and cobalt (II) nitrate hexahydrate (≥ 99%) were obtained from Sigma Aldrich. Ethanol was procured from Merck. Millipore ultrapure water (ρ = 18.2 MΩ) was used for hydrolysis of Titanium (IV) isopropoxide. Concentrated nitric acid (70%) and concentrated hydrochloric acid (37%) were purchased from Loba chemie. All chemicals were used as-received without purification.

3.4.2 Synthesis of Undoped TNPs

Synthesis of TNPs was carried out by sol-gel technique [40]. Synthesis protocols followed in these experiments are summarized as schematic in **Fig. 3.54**. In a typical synthesis, a sol was prepared by mixing 35 mM titanium isopropoxide with 25.5 mL ethanol under constant magnetic stirring. The solution was stirred for 5 min at 500 rpm. To this, 2.55 mL ethanoic solution of conc. HNO_3 having acid to titanium isopropoxide molar ratio of 0.2 was added. The mixture was stirred for another 30 min. To induce gelation, a mixture of ethanol (16.1 mL) and water (2.55 mL) was added drop-wise. The molar ratio of water and titanium isopropoxide was maintained at 4. After the addition of water-ethanol mixture, it is stirred at room temperature until gelation. The gel was dried over night at 100 °C. The dried crystallites were grinded and washed with distilled water multiple times. The powder was air dried at 150 °C and calcine at 500 °C for 4 h.

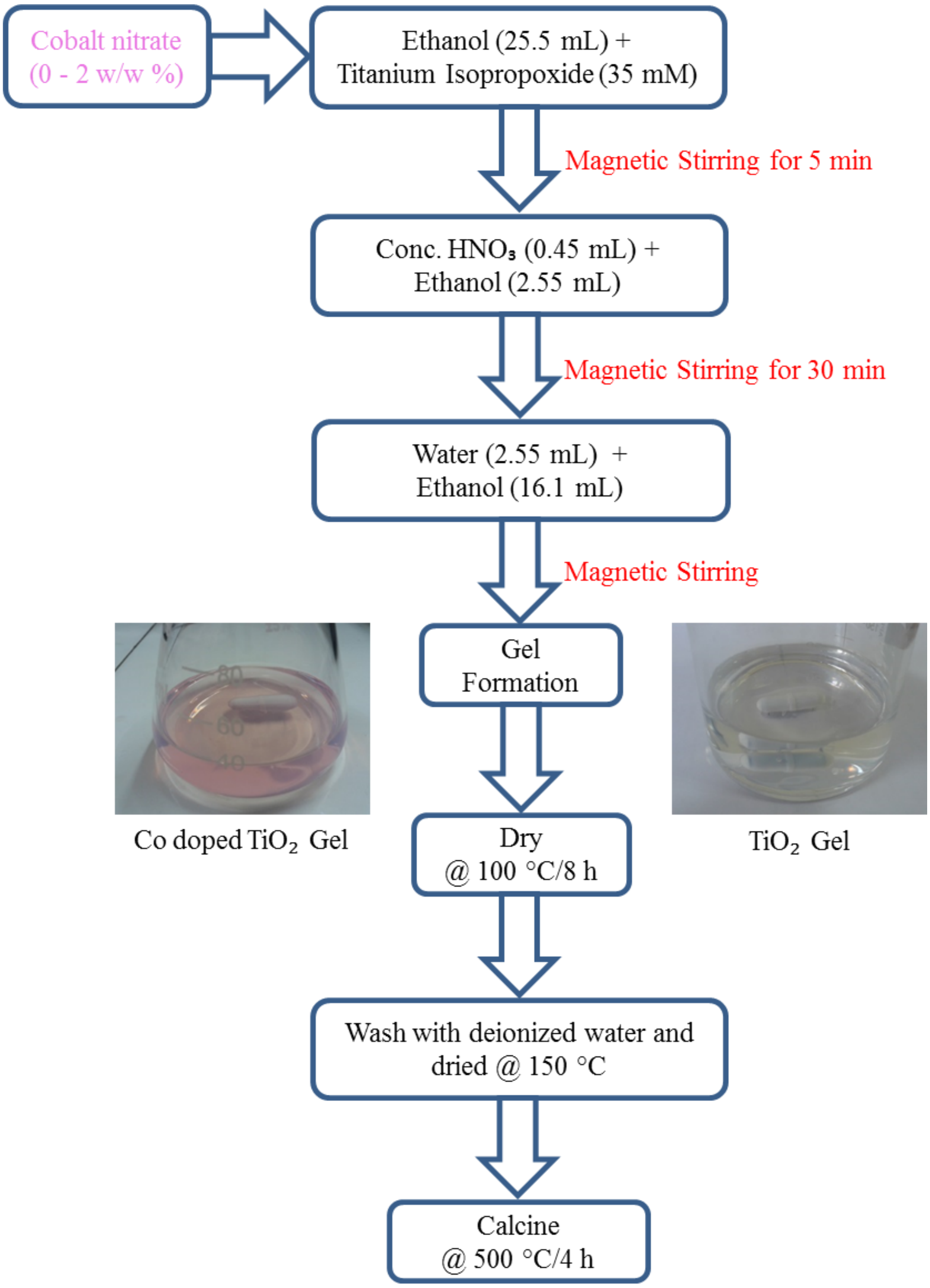

Fig. 3.54 Schematic presentation of the synthesis protocols followed for the preparation of undoped and cobalt doped TNPs by sol-gel technique.

3.4.3 Synthesis of Co-doped TNPs

Cobalt doped TNPs were also prepared by the sol-gel technique where the same protocols described for the synthesis of undoped TNPs in section 3.4.2 and summarized in **Fig. 3.54** were followed. Dopant concentration was varied from 0.05 wt %-2 wt % of TiO_2. In brief, ethanoic solution of $Co(NO_3)_2.6H_2O$ was prepared for each wt % of Co by dissolving appropriate quantity of $Co(NO_3)_2.6H_2O$ in required volume of ethanol so that its final concentration was adjusted to 0.1 M. To this, 25.5 mL ethanol was added and stirred for 5 min. In this solution, 10.5 mL titanium isopropoxide was added drop-wise under constant magnetic stirring. After 5 min, 2.55 mL ethanoic solution of conc. HNO_3 was added. The molar ratio of acid to titanium isopropoxide was 0.2. The solution was stirred for another 30 min. To induce gelation, ethanol (16.1 mL)-water (2.55 mL) mixture was added drop-wise. The molar ratio of water to titanium isopropoxide was 4. This will initiate the hydrolysis reaction. After adding the water-ethanol solution, the mixture was stirred at room temperature till gelation. The gel was dried over night at 100 °C and washed with distilled water multiple times. It was dried at 150 °C and calcined at 500 °C for 4 h.

3.4.4 Mechanism

Synthesis of TNPs via sol-gel process is a two-step approach [41,42]. In the first step, the organometallic source of Titanium (e.g. titanium isopropoxide) is hydrolysed via following chemical reaction:

$$Ti - (OC_3H_8) + H_2O \longrightarrow Ti - OH + C_3H_8OH$$

During the hydrolysis, water molecule attacks the titanium isopropoxide and supresses the condensation stage, which leads to the formation of TNPs. The presence of residual alkoxy groups also reduces the rate of crystallization of TNPs, which will also favor the formation of less dense anatase phase of TiO_2 [43]. In the second step, condensation of Ti – OH progresses with elimination of alcohol or water groups via alcohol or water condensation.

$$Ti - OH + C_3H_8 - Ti \longrightarrow Ti - O - Ti + C_3H_8OH$$

(Alcohol Condensation)

$$\mathrm{Ti-OH + HO-Ti \longrightarrow Ti-O-Ti + H_2O}$$

(Water Condensation)

Here, acid acts as a catalyst, which controls the kinetics of hydrolysis and condensation of titanium isopropoxide. Generally, the low pH in the reaction medium provides a good chance of preformation of TNPs which could supress further crystallization of TiO_2. The presence of excess anions of acid (NO_3^- or Cl^-) adsorbed on the surface of TNPs also supress their further growth [43]. Addition of acid does not form any residual impurity phases on the surface of TNPs after the calcination, which is confirmed from the X-ray diffraction measurement.

To find out appropriate value of crystallization temperature, the as-synthesized pristine and Co-doped TNPs are subjected to differential scanning calorimetry (DSC) measurement. The DSC thermograms of as-synthesized TNPs are shown in **Fig. 3.55**. An exothermic peak is observed between 400-460 °C. This peak corresponds to the transformation of amorphous TiO_2 to crystalline phase. The crystallization temperature corresponding to anatase phase for different cobalt doping is also represented in **Table - 3.2**.

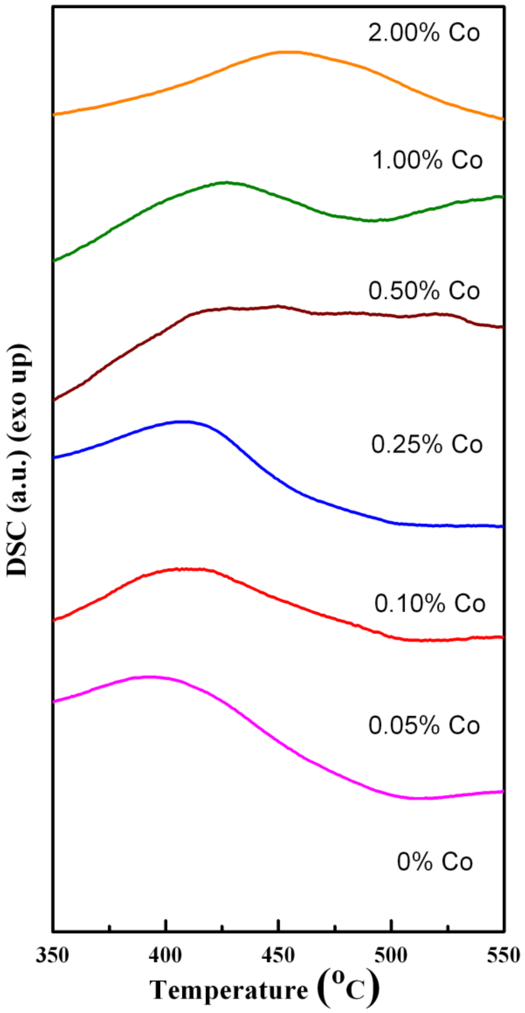

Fig. 3.55 DSC thermograms of cobalt (0-2 %) doped TNPs.

The crystallization temperature increases with Co-doping, indicating that the presence of cobalt ions in the TiO_2 matrix hinders the amorphous to anatase phase transition. From the obtained crystallization temperature data, 500 °C is chosen as the calcination temperature for all the samples of TNPs.

Table 3.2 Crystallization Temperature, Band Gap and Elemental Compositions of Co (0-2 %) doped TNPs.

Dopant Concentration (Cobalt) (wt %)	**Crystallization Temperature (°C)**	**Band Gap (eV)**	**Elemental Compositions obtained from EDS**		
			Ti (in wt %)	O (in wt %)	Co (in wt %)
0%	404	3.03	59.95	40.05	0
0.05%	392	2.95	59.91	40.03	0.06
0.10%	408	2.66	59.875	40.025	0.1
0.25%	408	2.56	59.78	40	0.22
0.50%	416	2.24	59.61	39.94	0.44
1%	427	1.97	59.21	39.82	0.98
2%	454	1.93	58.36	39.55	2.08

3.4.5 Investigation of TNPs

XRD patterns of undoped and cobalt doped TNPs are shown in **Fig. 3.56**.

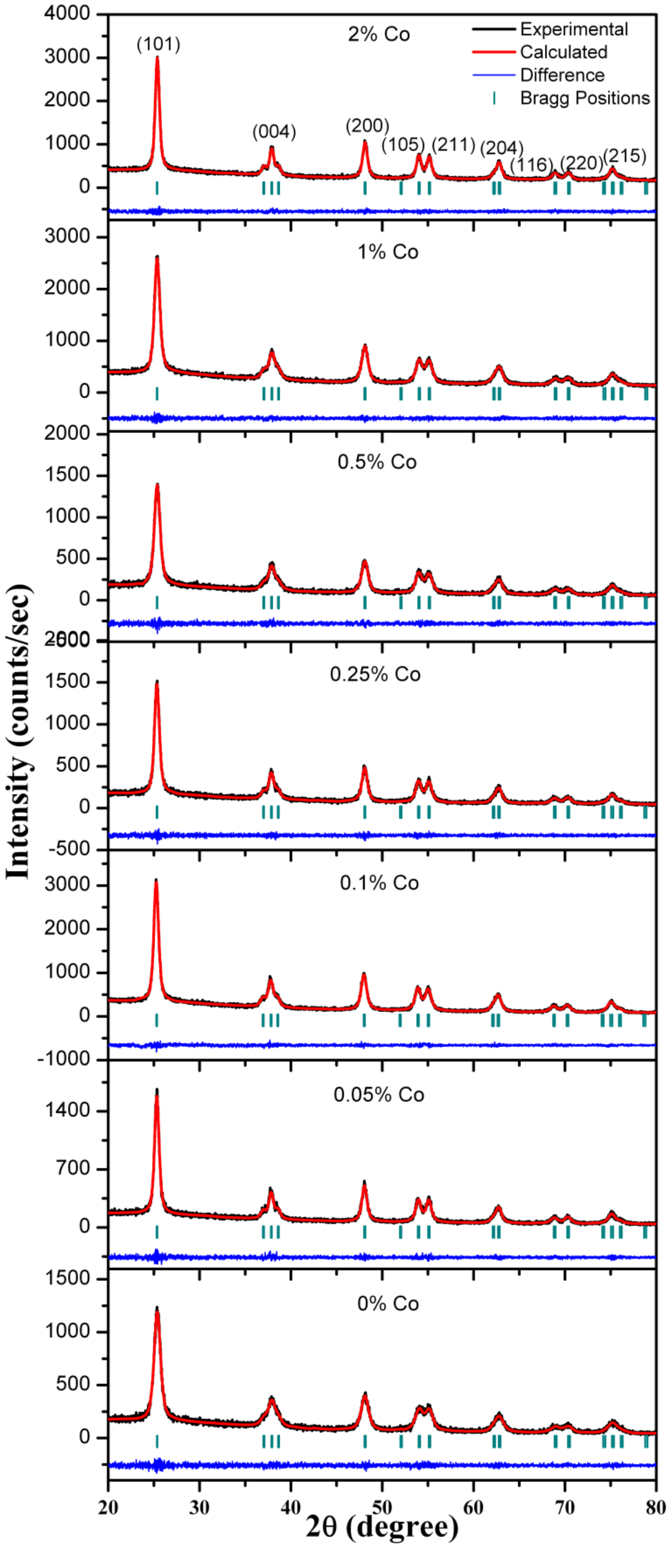

Fig. 3.56 XRD patterns of undoped and cobalt (0-2 %) doped TNPs.

Each diffractogram shows ten well resolved reflections. Peak positions of these reflections are in good agreement with the standard X-ray diffraction pattern of tetragonal anatase phase of TiO_2 (JCPDS card no. 21-1272). The (hkl) indices corresponding to each reflections are shown in **Fig. 3.56**. No signatures of rutile phase, pure cobalt or cobalt oxide are observed. The highest intense reflections of rutile and brookite phases are expected at 27.4° and 30.8°, respectively. The absence of these signatures in the X-ray diffractograms confirms the formation of single anatase phase TNPs. A slight shifting in the peak positions is observed. This shift is due to changes in the local structure around Ti^{4+} after Co^{2+} substitution [44]. Average crystallite size of TNPs is determined from the X-ray diffractograms by analysing them with Williamson-Hall analysis [Equation 3.1]. The crystallite sizes thus obtained are reported in **Table - 3.3**. The crystallite size varies between 8.5-11.7 nm. For undoped TNPs, the crystallite size is 8.5 nm. Upon Co doping, it increases and lies in the range of 9.5-11.7 nm. The crystallite size of Co doped TNPs is larger than the pristine TNPs. This result indicates that increasing Co concentration is not inhibiting the grain growth and hence it is likely that Co is entering into the TiO_2 lattice at interstitial or substitutional sites. From the Williamson-Hall analysis, the lattice strain has been calculated, which comes out to be of the order of 10^{-4}. This strain is one order smaller than that observed for SNPs. This might be because of lattice relaxation during sintering of amorphous titania.

In order to understand the effect of Co-doping on TiO_2 lattice, each XRD pattern is refined by Rietveld refinement technique by using Fullprof software package. XRD patterns are refined by assuming tetragonal symmetry with $I4_1/amd$ space group. The refined unit cell parameters of undoped and Co-doped TNPs are reported in **Table - 3.3**. $R_{wp} < 10\%$ and $\chi^2 \rightarrow 1$ indicate that the experimental patterns are in close correlation with the simulated patterns. The lattice parameter a = b do not show any significant deviation from the reported value of 3.7852 Å (JCPDS card no. 21-1272). Contrary to this, the lattice parameter c, which is along the long axis of the tetragonal unit cell shows a decrease in comparison to the reported value of 9.5139 Å. With increasing Co concentration, lattice parameter 'c' also increases and assumes maxima for 0.1 wt% Co. Further addition of Co in the TiO_2 matrix compresses the TiO_2 unit cell. For dopant concentration ≥ 0.5 wt%, the 'c' value is independent of doping. The same trend is also observed for unit cell volume (**Table - 3.3**). The Wyckoff positions of Ti, Co and O are also reported in **Table - 3.3**.

Table 3.3 Crystallographic parameters of Co (0-2%) doped TNPs obtained from Rietveld Refinement of XRD.

Dopant Concentration (Cobalt) (wt %)	**Crystallite Size (nm)**	**Atom**	**Site**	**Wyckoff positions**			**Lattice Parameters**		**Unit Cell Volume (Å^3)**	**Goodness of fit parameters**	
				x	y	z	a = b (Å)	c (Å)		χ^2	R_{wp} (%)
0%	8.5	Ti	4b	0	0.25	0.3750	3.7823(19)	9.4950(5)	135.83	1.15	8.98
		O	8e	0	0.25	0.1621(8)					
0.05%	11.6	Ti	4b	0	0.25	0.3750	3.7863(11)	9.5100(3)	136.34	1.23	9.41
		O	8e	0	0.25	0.1636(9)					
		Co	4b	0	0.25	0.3750					
0.10%	10.7	Ti	4b	0	0.25	0.3750	3.7900(8)	9.5160(2)	136.69	1.27	6.68
		O	8e	0	0.25	0.1634(3)					
		Co	4b	0	0.25	0.3750					
0.25%	10.8	Ti	4b	0	0.25	0.3750	3.7856(4)	9.5072(11)	136.24	1.14	8.88
		O	8e	0	0.25	0.1646(6)					
		Co	4b	0	0.25	0.3750					
0.50%	9.5	Ti	4b	0	0.25	0.3750	3.784(17)	9.5020(4)	136.06	1.17	8.51
		O	8e	0	0.25	0.1620(7)					
		Co	4b	0	0.25	0.3750					
1%	10.2	Ti	4b	0	0.25	0.3750	3.7839(11)	9.4950(3)	135.95	1.15	5.96
		O	8e	0	0.25	0.1614(4)					
		Co	4b	0	0.25	0.3750					
2%	11.7	Ti	4b	0	0.25	0.3750	3.7830(8)	9.4990(2)	135.94	1.15	5.76
		O	8e	0	0.25	0.1629(7)					
		Co	4b	0	0.25	0.3750					

No significant changes in the Wyckoff positions of O-atoms have been observed. This indicates that Co might have substituted at the Ti site. The observed little variation in the lattice parameter c and unit cell volume might be due to the difference in the ionic radii of Ti^{4+} (60.5 pm) and Co^{2+} (53 pm).

The SEM images of 0%, 0.1%, 1% and 2% cobalt doped TNPs are shown in **Fig. 3.57**. Irrespective of Co doping, nanoparticle clusters are observed in each micrograph with near spherical morphology. The average size of nanoparticles is 20 nm. The size distribution is uniform. Due to high density of particles in each micrograph, it is difficult to plot size distribution histograms from these micrographs and hence excluded from the study.

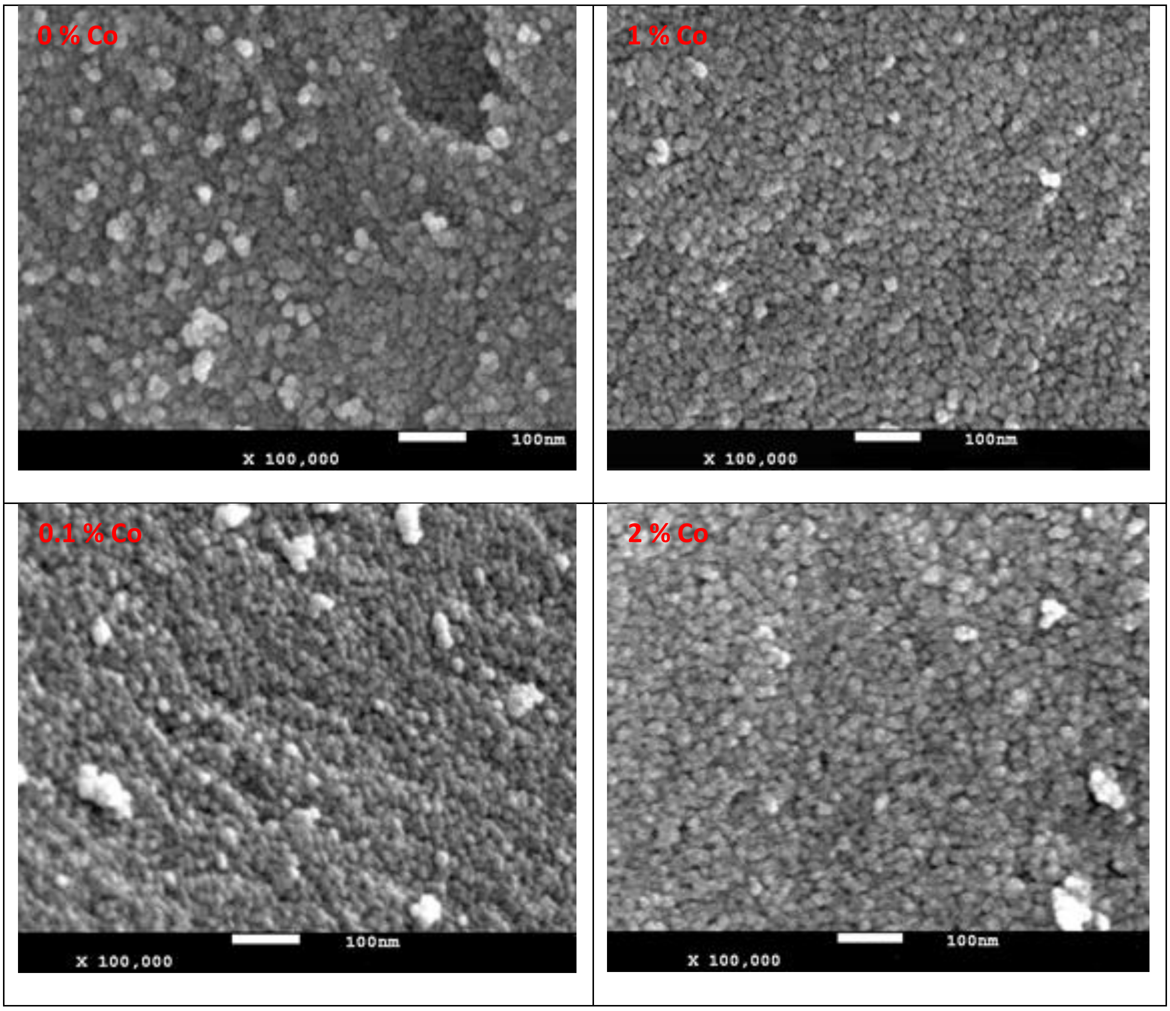

Fig. 3.57 SEM micrographs of undoped and cobalt doped TNPs.

The EDX patterns of pristine and Co doped TNPs are shown in **Fig. 3.58**.

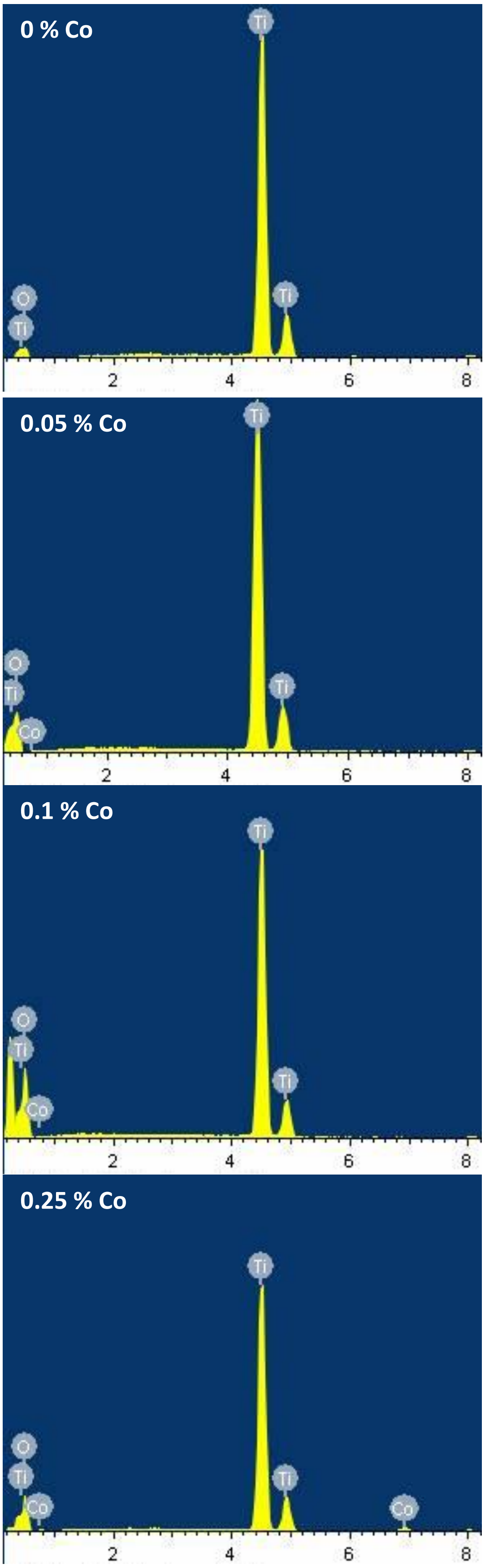

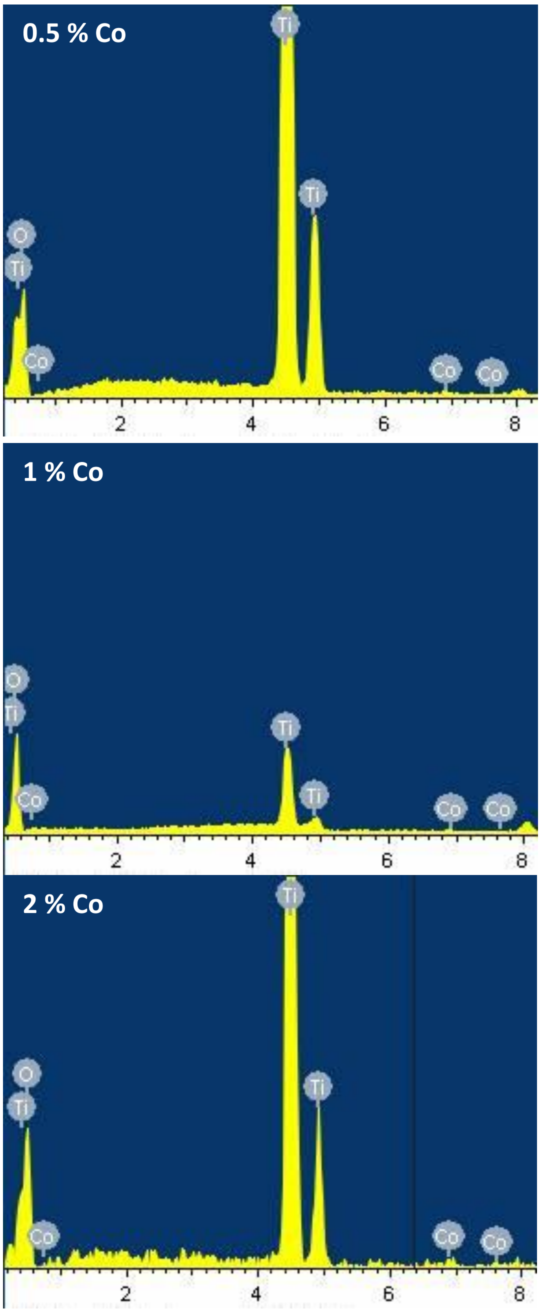

Fig. 3.58 EDX patterns of TNPs with different cobalt concentrations. X-axis represents energy of X-rays emitted by the specimen in keV.

The detail analysis of elemental analysis for each sample is presented in **Table - 3.2**. In the case of pristine TNPs, only titanium and oxygen are detected. The absence of foreign elements shows that the synthesized product has high chemical purity. The EDX spectra of doped samples also show the presence of cobalt. The detected cobalt content is in agreement with the expected concentration. The weight fraction of oxygen atoms decreases with increase in Co-doping. The observed % weight of oxygen in the sample is less than its accepted stoichiometric proportion. This data suggest that in the TiO_2 matrix, Ti^{4+} has been substituted by Co^{2+} and to compensate the extra charge and maintain charge neutrality of the sample, it creates additional vacancies at oxygen site [45]. The similar distortion of TiO_2 unit cell was also predicted from the XRD analysis.

A representative transmission electron microscopy image of undoped TNPs, which are calcined at 500 °C is shown in **Fig. 3.59**. Small nanoparticles with near spherical geometry can be observed in the TEM micrograph. Most of the nanoparticles are agglomerated, a typical character of nanoparticles generally observed when prepared via sol-gel route [46]. The average size of TNPs is 20 nm, which is in agreement with the results of scanning electron microscopy. Due to the heavy clustering, it is not possible to prepare their size distribution histograms.

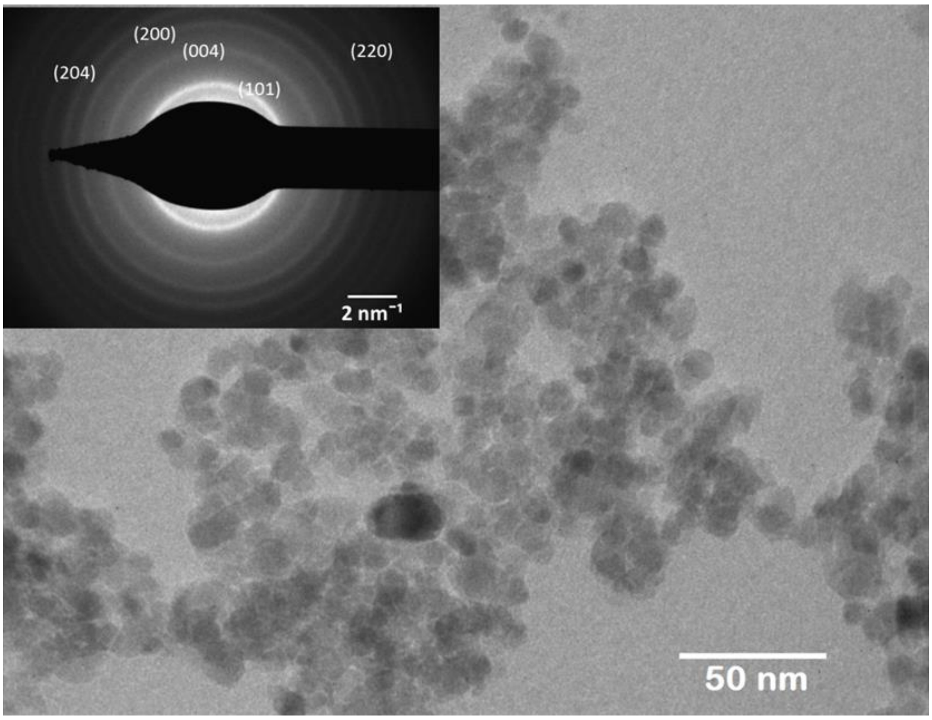

Fig. 3.59 TEM micrograph of undoped TNPs. The inset shows the selected area electron diffraction pattern of TNPs.

The top inset in **Fig. 3.59** shows the specific area electron diffraction image of TNPs. Well distinguish rings can be observed in the SAED pattern of TNPs confirming the polycrystalline nature of the nanoparticles. The SAED pattern is in well agreement with the anatase phase of TNPs. This result is also in good agreement with the results of X-ray diffraction studies.

Diffuse reflectance UV-visible spectroscopy is used to understand the substitution effect of dopant on host lattice and its co-ordination environment. Diffused reflectance spectra of undoped and Co-doped TNPs are shown in **Fig. 3.60**. Two small peaks at 497 nm and 584 nm are observed in 2% cobalt doped TNPs. These peaks are absent in case of pristine TNPs. The peak at 497 nm is due to the $^4T_{1g}$ to $^4T_{1g}(P)$ and at 584 nm is due to $^4T_{1g}$ to $^4A_{2g}$ transitions, which are due to the presence of Co^{2+} in the octahedral or pseudo octahedral coordination [47]. In case of anatase TiO_2, each Ti^{4+} is coordinated with six oxygen atoms. When Ti^{4+} is substituted by Co^{2+} then electrons in the d-orbital of Co^{2+} will undergo repulsion, which results in the splitting of d-orbitals of Co^{2+}. Kubelka-Munk equation [48] is used to relate the reflectance of the samples with their absorption. It is written as:

$$F(R) = (100-R)^2/200\,R \tag{3.3}$$

where R is the reflectance (in %) of the sample and F(R) is the corresponding absorbance [48].

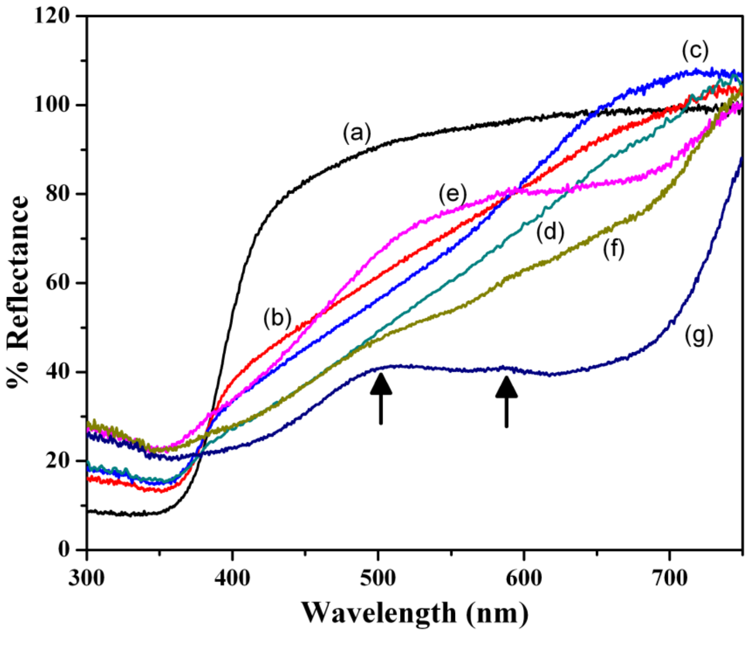

Fig. 3.60 Diffuse Reflectance UV-visible spectra of TNPs doped with (a) 0% Co, (b) 0.05% Co, (c) 0.1% Co, (d) 0.25% Co, (e) 0.5% Co, (f) 1% Co and (g) 2% Co.

To understand the effect of Co-doping on the energy band gap of TNPs, a graph of $[F(R)h\upsilon]^{1/2}$ → hυ is plotted in **Fig. 3.61**. The exponent ½ signifies that the band to band transition is of indirect nature. In order to determine the energy band, the linear portion of the curves are fitted and extrapolated for zero absorbance i.e. F[R] = 0. The point at which the extrapolated straight line intersects the X-axis is the band gap of the nanoparticles. The energy band gap of TNPs decreases with increasing dopant concentration (**Table - 3.2**).

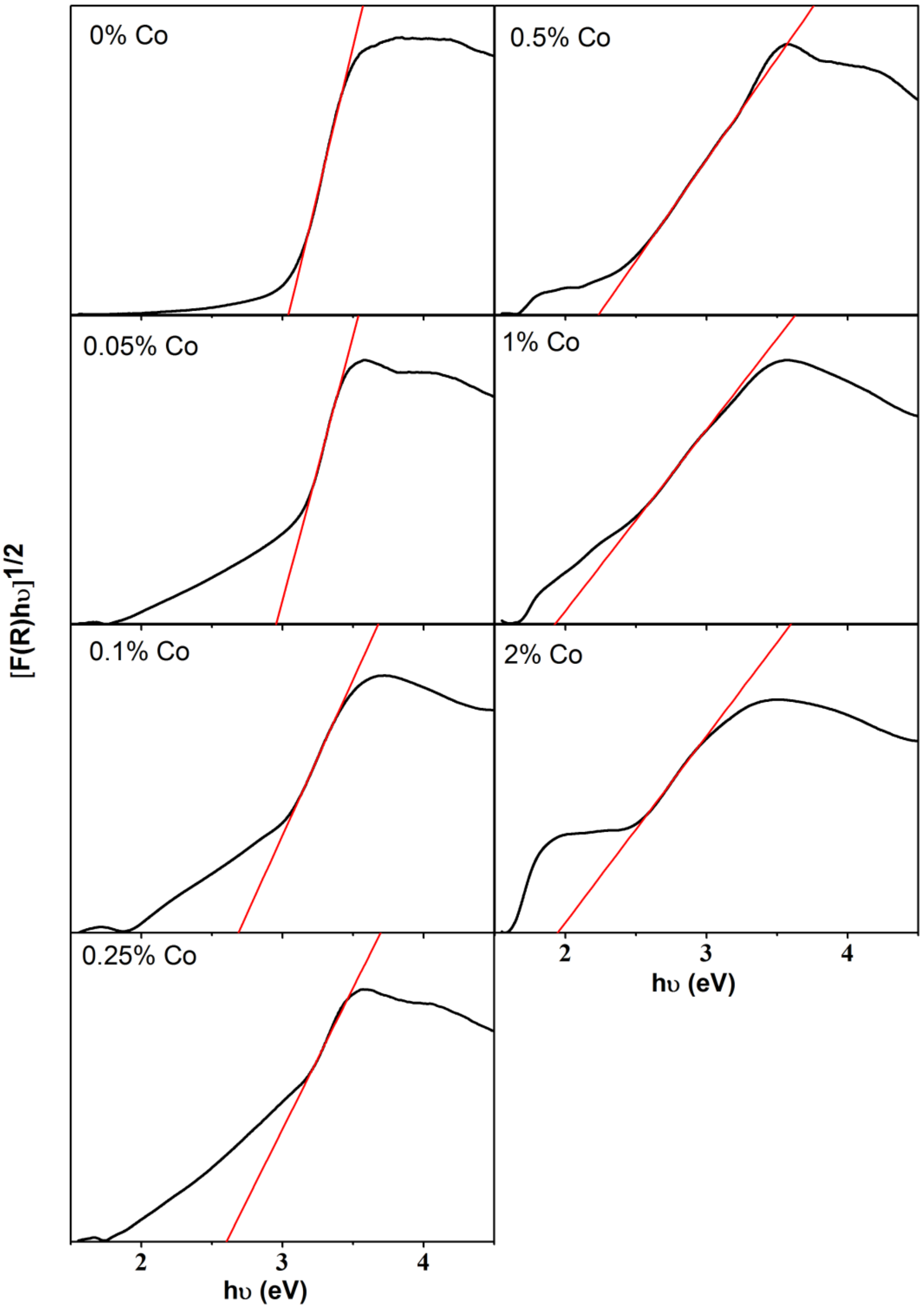

Fig. 3.61 The plots of $[F(R)h\upsilon]^{1/2}$ → hυ for Co (0-2%) doped TNPs.

The energy band gap of TNPs as a function of Co-doping is plotted in **Fig. 3.62**. The energy band gap of pristine TNPs is 3.03 eV. This energy band gap is lower than the reported band gap of anatase TiO_2 in bulk (3.2 eV) [45]. Generally decreasing particle size widens the energy gap [49]. Contrary to that, a band narrowing is observed in the present case. This decrease in energy band gap of pristine TNPs in reference to the reported band gap of bulk TiO_2 could be ascribed to the defect structure (oxygen vacancies) in the TNPs that introduces extra energy levels in the forbidden zone. The origin of such energy levels might be due to the change in the local distribution around Ti^{4+}or partial conversion of Ti^{4+} to Ti^{3+} and creation of oxygen vacant sites [45, 50-52].

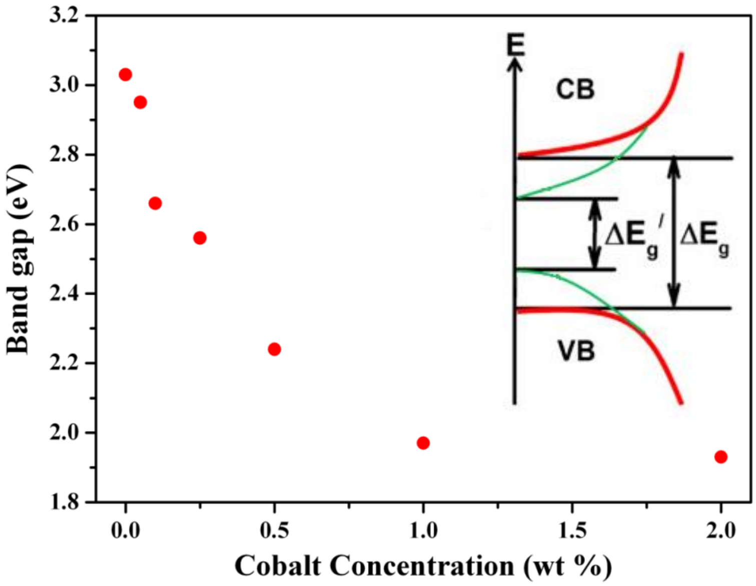

Fig. 3.62 Variation in the band gap of TNPs as a function of cobalt concentration. Inset shows the schematic representation of band narrowing in TNPs due to cobalt doping.

With increase in the Co-doping, the energy band gap of TNPs decreases drastically. Without Co, the band gap of TNPs is 3.03 eV, which decreases to 1.93 eV with 2 wt % Co-doping. The decrease in the energy band gap of TNPs with increasing cobalt doping can be assigned to the introduction of new d-states near the valence band edge which narrows the energy band gap of the system. In addition, the substitution of Co^{2+} at the Ti^{4+} site also introduces oxygen vacancy related defect states in the forbidden zone of the energy band gap of TiO_2. Both these mechanisms are responsible for band narrowing in cobalt doped TNPs. The schematic representation of band narrowing due to Co-doping is shown in the inset of **Fig. 3.62**.

References

1. Z. Guo and L. Tan, Fundamentals and Applications of Nanomaterials, Artech House, (2009).
2. G. Guisbiers, S. M. Rosales and F. L. Deepak, Journal of Nanomaterials 2012, Article ID 180976 (2012).
3. W. Jiang, H. C. Yang, S. Y. Yang, H. E. Horng, J. C. Hung, Y. C. Chen and C. Y. Hong, Journal of Magnetism and Magnetic Materials 283, 210-214 (2004).
4. E. Roduner, Chemical Society Reviews 35, 583-592 (2006).
5. S. Gnanam and V. Rajendran, Journal of Nanoparticles 2013, Article ID 839391 (2013).
6. B. Faure, G. S. Alvarez, A. Ahniyaz, I. Villaluenga, G. Berriozabal, Y. R. Miguel and L. Bergstrom, Science and Technology of Advanced Materials 14, 023001 (2013).
7. Z. Khan, S. A. Al-Thabaiti, A. Y. Obaid and A. O. Al-Youbi, Colloids and Surfaces B: Biointerfaces 82, 513-517 (2011).
8. Chandni, N. Andhariya, O. P. Pandey and B. Chudasama, RSC Advances 3, 1127-1136 (2013).
9. C. Khurana, A. K. Vala, N. Andhariya, O. P. Pandey and B. Chudasama, Journal of Biomedical Materials Research Part A (2013) doi: 10.1002/jbm.a.35005.
10. M. J. Kale, T. Avanesian and P. Christopher, ACS Catalysis 4, 116-128 (2014).
11. V. E. Ferry, J. N. Munday and H. A. Atwater, Advanced Materials 22, 4794-4808 (2010).
12. A. M. Alkilany, L. B. Thompson, S. P. Boulos, P. N. Sisco and C. J. Murphy, Advanced Drug Delivery Reviews 64, 190-199 (2012).
13. S. Magdassi, M. Grouchko and A. Kamyshny, Materials 3, 4626-4638 (2010).
14. R. G. Chaudhuri and S. Paria, Dalton Transactions 43, 5526-5534 (2014).
15. L. Armelao, D. Barreca, G. Bottaro, A. Gasparotto, C. Maccato, C. Maragno, E. Tondello, U. L. Stangar, M. Bergant and D. Mahne, Nanotechnology 18, 375709 (2007).
16. C. Jayaseelan, A.A. Rahuman, S. M. Roopan, A.V. Kirthi, J. Venkatesan, S.Kim, M. Iyappan and C. Siva, Spectrochimica Acta Part A: Molecular and Biomolecular Spectroscopy 107, 82-89 (2013).
17. M. Chen, Y. G. Feng, X. Wang, T. C. Li, J. Y. Zhang and D. J. Qian, Langmuir 23, 5296-5304 (2007).
18. J. Xie, S. Peng, N. Brower, N. Pourmand, S. Wang and S. Sun, Pure and Applied Chemistry 78, 1003-1014 (2006).
19. B. Chudasama, A. K. Vala, N. Andhariya, R. V. Mehta and R. V. Upadhyay, Journal of Nanoparticle Research 12, 1677-1685 (2010).
20. B. D. Cullity and S. R. Stock, Elements of X-ray Diffraction, 3rd Edition. Addison-Wesley Publishing Company, Inc. (2002).
21. K. Parekh, R. V. Upadhyay and R. V. Mehta, Bulletin of Materials Science 23, 91-95 (2000).
22. D. A. Ferrer, S. Guchhait, H. Liu, F. Ferdousi, C. Corbet, H. Xu, M. Doczy, G. Bourianoff, L. Mathew, R. Rao, S. Saha, M. Ramon, S. Ganguly, J. T. Markert and S. K. Banerjee, Journal of Applied Physics 110, 0143161-0143167 (2011).
23. G. A. M. Castanon, N. N. Martinez, F. M. Gutierrez, J. R. M. Mendoza and F. J. Ruiz, Journal of Nanoparticle Research 10, 1343-1348 (2008).

24. J. G. Barrasa, J. M. Lopez-de-Luzuriaga and M. Monge, Central European Journal of Chemistry 9, 7-19 (2011).
25. J. Zhang, S. Rana, R. Srivastava and R. Misra, Acta Biomaterialia 4, 40-48 (2008).
26. J. P. Novak and D. L. Feldheim, Journal of the American Chemical Society 122, 3979-3980 (2000).
27. P. Chandaroy, A. Sen, P. Alexandridis and S. Hui, Biochimica et Biophysica Acta 1559, 32-42 (2002).
28. S. Sun, H. Zeng, D. B. Robinson, S. Raoux, P. M. Rice, S. X. Wang and G. Li, Journal of the American Chemical Society 126, 273-279 (2004).
29. N. Andhariya, B. Chudasama, R. V. Mehta and R. V. Upadhyay, Journal of Nanoparticle Research 13, 1677-1688 (2011).
30. J. L. C. Huaman, K. Sato, S. Kurita, T. Matsumoto and B. Jeyadevan, Journal of Materials Chemistry 21, 7062-7069 (2011).
31. M. Hu, J. Chen, Z. Y. Li, L. Au, G. V. Hartland, X. Li, M. Marquez and Y. Xia, Chemical Society Reviews 35, 1084-1094 (2006).
32. S. W. Verbruggen, M. Keulemans, J. A. Martens and S. Lenaerts, The Journal of Physical Chemistry C 117, 19142-19145 (2013).
33. S. Pal, Y. K. Tak and J. M. Song, Applied and Environmental Microbiology 73, 1712-1720 (2007).
34. L. Li and Q. Wang, ACS Nano 7, 3053-3062 (2013).
35. Z. Zhang, B. Zhao and L. Hu, Journal of Solid State Chemistry 121, 105-110 (1996).
36. H. Hirai, H. Wakabayashi and M. Komiyama, Bulletin of the Chemical Society of Japan 59, 367-372 (1986).
37. I. Haas, S. Shanmugam and A. Gedanken, The Journal of Physical Chemistry B 110, 16947-16952 (2006).
38. W. Yu, H. Xie, L. Chen, Y. Li and C. Zhang, Nanoscale Research Letters 4, 465-470 (2009).
39. J. Xiong, Y. Wang, Q. Xue and X. Wu, Green Chemistry 13, 900-904 (2011).
40. F. Sayilkan, M. Asilturk, H. Sayilkan, Y. Onal, M. Akarsu and E. Arpac, Turkish Journal of Chemistry 29, 697-706 (2005).
41. M. T. Harris and A. Singhal, Journal of Sol-Gel Science and Technology 8, 41-47 (1997).
42. J. Livage, M. Henry and C. Sanchez, Progress in Solid State Chemistry 18, 259-341 (1988).
43. M. Hamadanian, A. R. Vanani and A. Majedi, Journal of the Iranian Chemical Society 7, S52-S58 (2010).
44. B. Choudhury and A. Choudhury, Journal of Luminescence 132, 178-184 (2012).
45. B. Choudhury, M. Dey and A. Choudhury, International Nano Letters 3, 25-32 (2013).
46. L. L. Hench and J. K. West, Chemical Reviews 90, 33-72 (1990).
47. J. D. Lee, Concise Inorganic Chemistry, 5th Ed. Wiley (1998).
48. K. Das, S. N. Sharma, M. Kumar, and S. K. De, The Journal of Physical Chemistry C 113, 14783-14792 (2009).
49. A. M. Smith and S. Nie, Accounts of Chemical Research 43, 190-200 (2010).
50. M. Sahu and P. Biswas, Nanoscale Research Letters 6, 441-454 (2011).
51. G. Liu, H. G. Yang, X. Wang, L. Cheng, H. Lu, L. Wang, G. Q. Lu and H. M. Cheng, The Journal of Physical Chemistry C 113, 21784-21788 (2009).
52. M. Pal, U. Pal, J. Jimenez and F. Rodriguez, Nanoscale Research Letters 7, 1-12 (2012).

CHAPTER 4

ANTIBACTERIAL ACTIVITY

4.1 Introduction

Development of antibiotic resistance in microbes is becoming increasing important issue in public health care [1, 2]. Limited options are available with pharmacologist to tackle the threats posed by rapidly growing community of multi-drug resistant strains [3]. More and more number of traditional antibiotic drugs is disappearing from the market as they are losing their sensitivity on microbes, which are developing resistance by mutations. Excessive and uncontrolled use of antibiotics in both preventive and curative healthcare across the globe has even worsen the situation, as microbes, which have never been exposed to a particular antibiotic drug are acquiring resistance towards that drug due to transfer of gene coding [4]. Hence, fighting multidrug resistance with traditional antibiotics is getting tougher and need is being felt for the development of non-traditional antibiotics against which microbes are unlikely to acquire resistance. The possible choice could be metals and metal oxide nanostructures as their anti-disinfectant properties in the bulk state are well known [5, 6].

In this chapter, antibacterial properties of nanostructured metals (SNPs and CNPs) and metal oxide (TNPs), which are designed and synthesized as per the protocols described in chapter-3 are evaluated. Antimicrobial tests of as-synthesized nanostructures are conducted on clinically important (*E. coli*, *S. aureus* and *P. vulgaris*) pathogenic bacterial strains by micro-dilution and disk diffusion techniques [4]. To further understand the synergetic effect of non-traditional antibiotics (metals or metal oxide nanostructures) on conventional antibiotics (tetracycline or kanamycin), formulations of antibiotic (tetracycline / kanamycin) adsorbed nanoparticles (SNPs / CNPs / TNPs) have been prepared and their antibacterial properties are also investigated by disk diffusion test.

Another important concern is the non-target effects of nanomaterials' biocidal activities on microbes that take part in bioremediation processes [7]. Nanoparticles leaching out from various products are getting accumulated in the environment. These leached nanoparticles can interact with the microbes present in the ecosystem of the earth and could irreversibly damage them [7]. Environmental implications of such interactions would be devastating. This aspect of nanobiotechnology is in infancy and requires serious consideration. In the second part of this chapter, antimicrobial activities of metals (SNPs / CNPs) and metal oxides (TNPs) are evaluated on non-pathogenic microbes of *B. subtilis* and *P. fluorescens*. Biocidal activities of nanoparticles (SNPs / CNPs / TNPs) and their formulations with antibiotics (tetracycline / kanamycin) are studied by micro-dilution and disk diffusion tests. Biocidal activities of nanoparticles and their formulations with antibiotics against pathogenic and non-pathogenic microbes are compared and results are scrutinized in reference to existing literature.

4.2 Materials

Mueller Hinton Agar (MM019) and nutrient broth (NM019) were purchased from Sisco Research Laboratories. Ultrapure MilliQ water (ρ = 18.2 MΩ) was used for the preparation of growth media. As-synthesized SNPs, CNPs, TNPs, commercially available antibiotics tetracycline (hydrochloride salt) and kanamycin (sulphate salt) were used as antimicrobial agents. Tetracycline and kanamycin were purchased from Sigma Aldrich. Antibacterial activities have been investigated on clinically important strains of *Escherichia coli* (MTCC No. 77), *Staphylococcus aureus* (MTCC No. 9760), *Proteus vulgaris* (MTCC No. 426) and eco-friendly microorganisms of *Bacillus subtilis* (MTCC No. 441) and *Pseudomonas fluorescens* (MTCC No. 1749).

4.3 Preparation of Nutrient Broth and Mueller Hinton Agar Medium

Nutrient Broth medium was prepared as per the standard protocols by dissolving 25 gm Nutrient Broth in 1 L of distilled water. Heated it to boiling and then autoclave it at 15 psi pressure and at 121 °C for 15 min. It was used for the determination of minimum inhibitory concentrations of antibiotics under test by micro-dilution method. Mueller Hinton Agar medium was prepared as per the standard protocols by dissolving 39 gm Mueller Hinton Agar in 1L of distilled water. Heated it to boiling and then autoclave it at 15 psi pressure and at 121 °C for 15 min. It was used for the determination of zone of inhibition of antibiotics under investigation by disk diffusion test.

4.4 Preparation of Antibiotic Adsorbed SNPs and CNPs

Antibiotic adsorbed SNPs and CNPs were prepared by vortex mixing of 10 mL aqueous colloidal dispersion of SNPs/CNPs with desired quantity of tetracycline or kanamycin for 12 hr. The final concentration of metal nanoparticles in antibiotics adsorbed nanoparticles was adjusted to 250 ppm. The mixture was centrifuged at relative centrifugal force (RCF) of 15471 x g (12000 rpm). Supernal was removed and the final volume of the colloid was readjusted to 10 mL by adding appropriate quantity of ultrapure water. This stock solution of antibiotics adsorbed metal nanoparticles was further used for the antibacterial test.

4.5 Antibiotic Content and Antibiotic Loading

Antibiotic content and antibiotic loading efficiency of tetracycline / kanamycin on nanoparticle surface was determined by UV-visible spectroscopy. Optical density of antibiotics that remained unincorporated (supernal) into the metal nanoparticles was measured at 357 nm for tetracycline and at 256 nm for kanamycin and its concentration was determined by Beer-Lambert law, $A = \varepsilon cl$ where A is the optical density at sample concentration c, l is the path length of sample cell (10 mm) and ε is molar absorptivity (ε for tetracycline and kanamycin is $14.58\times10^{6}\ M^{-1}cm^{-1}$ and $143.40\ M^{-1}cm^{-1}$, respectively) of the drug. Antibiotic content and antibiotic loading efficiency were determined by using the following expressions [8],

$$\text{Antibiotic Content} = \frac{\text{Weight of Antibiotic adsorbed on Nanoparticles}}{\text{Total weight of Nanoparticles}} \times 100 \qquad (4.1)$$

$$\text{Antibiotic loading efficiency} = \left[\frac{W_1 - W_2}{W_1}\right] \times 100 \qquad (4.2)$$

where W_1 is the total weight of antibiotic and W_2 is the weight of free antibiotic.

For tetracycline adsorbed SNPs, the loading efficiency of tetracycline was 15.30% while the drug content in the antibiotic adsorbed SNPs was 40.56%. For kanamycin, the loading efficiency was measured as 6.44% and the drug content in the antibiotic adsorbed SNPs was 90.40%. In case of tetracycline adsorbed CNPs, the loading efficiency was 8.6% and the drug content was 57.2%. For kanamycin, the loading efficiency was 10.63% and the drug content was 98.18% in antibiotic adsorbed CNPs.

4.6 Micro-dilution Test

Six sets of 10 mL nutrient broth medium containing nanoparticles with effective metals or metal oxide concentration between 0 to 500 µg/mL were prepared. Each set was inoculated aseptically with 10^8 CFU/mL of the respective bacterial suspension. The inoculated sets were incubated at 37 ºC for 24 h. Each experiment was carried out in triplicate. MIC is evaluated by visual inspection of growth or no growth of bacterial strain in the test tubes containing different concentrations of metal or metal oxide nanoparticles. Turbidity of the media is the indication of the bacterial growth. The lowest concentration of metal or metal oxide nanoparticles that inhibited bacterial growth is taken as the MIC for that particular bacterium [4]. Control experiments were also run parallel to investigate the antibacterial activities of nutrient broth medium.

4.7 Disk Diffusion test

32 mL of Mueller Hinton Agar medium was added to the disposable petridishes and allowed it to solidify. The bacterial strain (10^8 CFU/mL) was inoculated onto the entire surface of a Mueller-Hinton agar plate with the help of sterile cotton-tipped swab to form an even lawn. The sample disk / well containing appropriate quantity of the antibacterial agent (metal nanoparticles / tetracycline / kanamycin / tetracycline adsorbed metal nanoparticles / kanamycin adsorbed metal nanoparticles) was used. Each experiment was carried out in triplicate and results were statically averaged. Each set was incubated at 37 ºC for 24 h. ZIH was measured after the incubation period, which was the area on the agar plate where the colony formation was inhibited due to leaching of the antibacterial agent [4].

4.8 Adsorption of Antibiotics on SNPs and CNPs

To understand the interaction of antibiotics with SNPs, UV-visible spectra of SNPs, tetracycline, kanamycin, tetracycline adsorbed SNPs and kanamycin adsorbed SNPs were recorded. Absorption spectra of these samples are shown in **Fig. 4.1**. The characteristic SPR band of SNPs was observed at 428.5 nm. The UV-visible spectrum of tetracycline show three characteristics absorption bands centred at 357 nm, 275 nm and 250 nm, respectively. These multiplets correspond to the $\pi\rightarrow\pi^*$ transitions of C = C. Kanamycin did not show any characteristic absorption bands in the UV-Visible region of the electromagnetic spectrum. But its complex with copper shows characteristics absorption at 256 nm, which is also shown in **Fig. 4.1**.

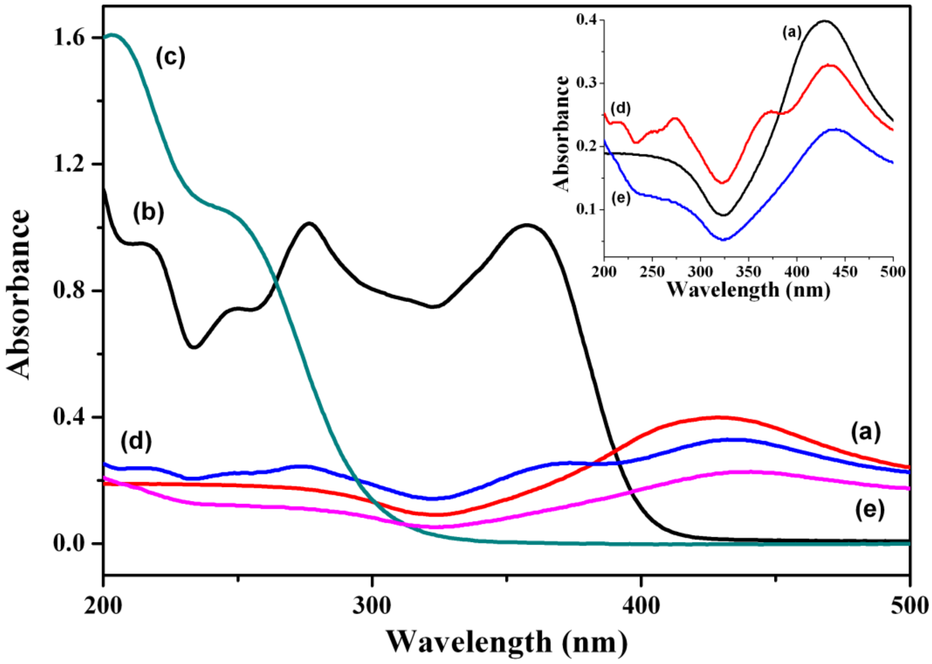

Fig. 4.1 UV-visible spectra of (a) SNPs (b) tetracycline (c) kanamycin (d) tetracycline adsorbed SNPs and (e) kanamycin adsorbed SNPs. Inset shows the magnified view of UV-visible spectra of (a) SNPs (d) tetracycline adsorbed SNPs and (e) kanamycin adsorbed SNPs.

In order to understand the interaction of tetracycline and kanamycin with SNPs, UV-visible spectra of tetracycline adsorbed SNPs and kanamycin adsorbed SNPs were also recorded. The multiplets of tetracycline were observed at 374 nm, 272 nm and 252 nm, respectively. The SPR band originating from the SNPs in the tetracycline-SNPs complex showed a red shift and positioned at 435 nm. In case of kanamycin adsorbed SNPs, the characteristic absorption of kanamycin at 256 nm shifted to 252 nm while the SPR band of SNPs shifted from 428 nm to 430 nm. Slight blue shift in the spectral bands of tetracycline, kanamycin and SNPs indicates that the antibiotics were adsorbed on the surface of the SNPs. UV-visible spectra of CNPs, tetracycline and tetracycline adsorbed CNPs are shown in **Fig. 4.2**. The characteristic absorption of tetracycline at 357 nm shifted to 363 nm while the SPR band of CNPs shifted from 564 nm to 566 nm in tetracycline adsorbed CNPs. **Fig. 4.3** shows the UV-visible spectra of CNPs, kanamycin and kanamycin adsorbed CNPs. The characteristic absorption of kanamycin at 256 nm shifted to 262 nm while the SPR band of CNPs shifted from 564 nm to 566 nm in kanamycin adsorbed CNPs sample. Little variation in the spectral signatures of tetracycline and kanamycin after their interactions with CNPs confirmed that both tetracycline and kanamycin were physiadsorbed on CNPs.

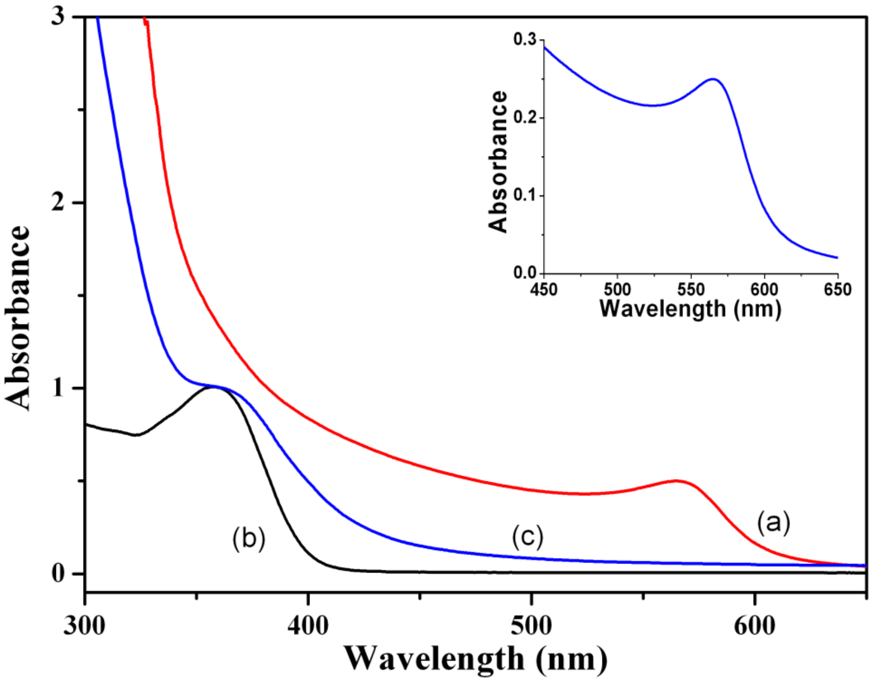

Fig. 4.2 UV-visible spectra of (a) CNPs (b) tetracycline and (c) tetracycline adsorbed CNPs. Inset shows the magnified view of UV-visible spectra of tetracycline adsorbed CNPs in 450 - 650 nm spectral range.

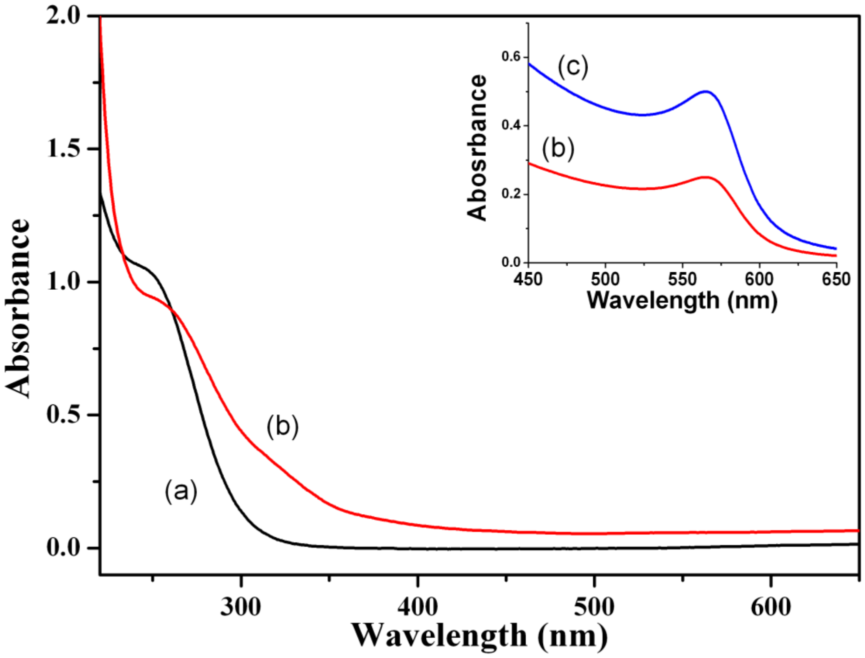

Fig. 4.3 UV-visible spectra of (a) kanamycin and (b) kanamycin adsorbed CNPs. Inset shows the magnified view of UV-visible spectra of (b) kanamycin adsorbed CNPs and (c) CNPs in 450-650 nm spectral range.

4.9 Antibacterial Activity

Antimicrobial activity of nanoparticles and nanoparticles adsorbed antibiotics have been studied against three pathogenic (*E. coli*, *S. aureus* and *P. vulgaris*) and two environmental friendly (*B. subtilis* and *P. fluorescens*) bacterial strains by micro-dilution and disk diffusion tests. From micro-dilution method, the MIC values of as-synthesized SNPs were determined for these bacterial strains. To further understand the effectiveness of SNPs on these microorganisms, the disk diffusion tests were also carried out in the presence of commercially available antibiotics; tetracycline and kanamycin. In this test, the zone of inhibition was measured after incubating particular strain in the presence of SNPs for 24 h.

The results of MIC tests against pathogenic strains are presented in **Fig. 4.4** and summarized in **Table 4.1**. The MIC value of SNPs is 30 µg/mL for *E. coli* followed by 100 µg/mL for *P. vulgaris* and 150 µg/mL for *S. aureus*. Photographic view of MIC tests of SNPs on *B. subtilis* and *P. fluorescens* is shown in **Fig. 4.5**. The MIC value of SNPs for *B. subtilis* and *P. fluorescens* is 25 µg/mL, each. The MIC values of SNPs for environmental friendly microorganisms are low as compared to pathogenic microorganisms. This observation shows that environmental friendly microorganisms under test are more susceptible to SNPs as compared to pathogenic microorganisms.

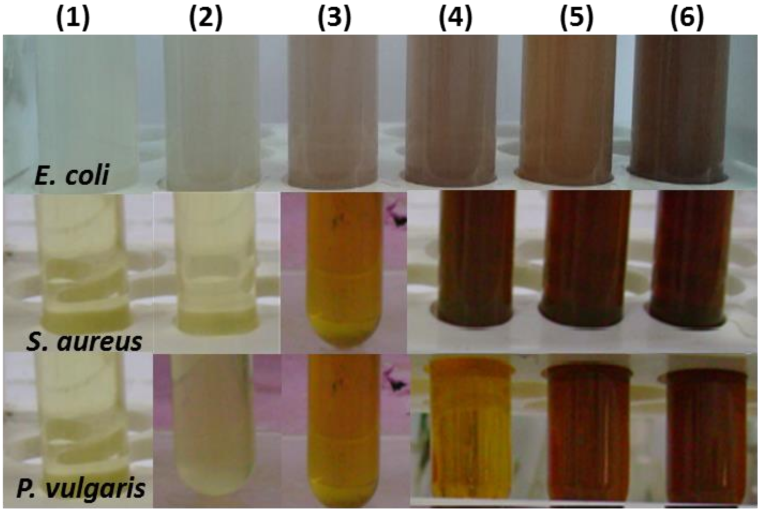

Fig. 4.4 Photographic view of MIC tests of SNPs on *E. coli*, *S. aureus* and *P. vulgaris*. Order of the tubes from left to right: 1. Negative control (i.e., medium alone); 2. Control (i.e., medium + antibacterial agent (SNPs)); 3. Zero concentration (i.e., medium + respective bacterial strain); 4. 30 % below MIC (i.e., medium + respective bacterial strain + SNPs having concentration 30 % below MIC); 5. 10 % below MIC (i.e., medium + respective bacterial strain + SNPs having concentration 10 % below MIC); 6. At MIC (i.e., medium + respective bacterial strain + SNPs having concentration equal to MIC).

Table 4.1 MIC values of SNPs, CNPs and TNPs.

Strains	**Class**	**Nature**	**MIC (µg/mL)**		
			SNPs	CNPs	TNPs
E. coli	Pathogenic	Gram -ve	30	20	Nil
S. aureus		Gram +ve	150	20	------
P. vulgaris		Gram -ve	100	30	------
B. subtilis	Non-pathogenic	Gram +ve	25	50	Nil
P. fluorescens		Gram -ve	25	20	Nil

The results of antimicrobial tests of SNPs, commercial antibiotics tetracycline and kanamycin and antibiotics adsorbed SNPs against pathogenic strains by disk diffusion method are shown in **Table 4.2**. For tetracycline, the ZIH was 28, 33 and 16 mm for *E. coli*, *S. aureus* and *P. vulgaris*, respectively. For kanamycin, the ZIH of 24 mm was observed for *E. coli*, 21 mm for *S. aureus* and 25 mm for *P. vulgaris*. The ZIH values for SNPs were 12, 11 and 7 mm for *E. coli*, *S. aureus* and *P. vulgaris*, respectively. To understand the additive effects of SNPs, the disk diffusion experiments were also carried out for tetracycline adsorbed SNPs and kanamycin adsorbed SNPs. The ZIH values for tetracycline adsorbed SNPs was same for *E. coli* and *P. vulgaris*, which was 27 mm and for *S. aureus*, it was 34 mm. The ZIH values for kanamycin adsorbed SNPs were 23, 26 and 27 mm for *E. coli*, *S. aureus* and *P. vulgaris*, respectively.

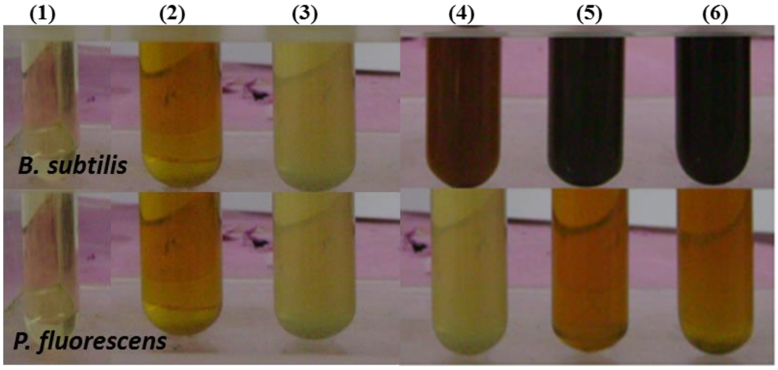

Fig. 4.5 Photographic view of MIC tests of SNPs on *B. subtilis* and *P. fluorescens*. Order of the tubes from left to right: 1. Negative control (i.e., medium alone); 2. Control (i.e., medium + antibacterial agent (SNPs)); 3. Zero concentration (i.e., medium + respective bacterial strain); 4. 30 % below MIC (i.e., medium + respective bacterial strain + SNPs having concentration 30 % below MIC); 5. 10 % below MIC (i.e., medium + respective bacterial strain + SNPs having concentration 10 % below MIC); 6. At MIC (i.e., medium + respective bacterial strain + SNPs having concentration equal to MIC).

Table 4.2 Additive effect of commercial antibiotics on antibacterial activities of SNPs.

Strains	**Class**	**Zone of Inhibition (ZIH) (mm)**					
		Control	Tetracycline	Kanamycin	SNPs	Tetracycline adsorbed SNPs	Kanamycin adsorbed SNPs
E. coli	Pathogenic	0	28	24	12	27	23
S. aureus	Pathogenic	0	33	21	11	34	26
P. vulgaris	Pathogenic	0	16	25	7	27	27
B. subtilis	Non-pathogenic	0	34	29	6	50	20
P. fluorescens	Non-pathogenic	0	22	11	7	40	30

Additive effect of SNPs is clearly evidenced from the increase in ZIH for antibiotic adsorbed SNPs with respect to the inhibition zone found for a particular antibiotic. The inhibition zone increases in the range of 60-186% for pathogenic microorganisms under investigation when tetracycline is adsorbed on SNPs while it increases in the range of 70-214% when used with kanamycin. These values were calculated by applying correction for drug loading efficiency (15.3% for tetracycline and 6.44% for kanamycin) in antibiotic adsorbed SNPs.

The images of disk diffusion test are shown in **Fig. 4.6** and **Fig. 4.7**. The inhibition zone of SNPs for the environmental friendly microorganisms was in the range of 6-7 mm. ZIH values of tetracycline and kanamycin were also measured. The images of disk diffusion test are presented in **Fig. 4.8**. Additive effect of SNPs is clearly evidenced from the increase in ZIH of antibiotic adsorbed SNPs with respect to ZIH for a particular antibiotic. Sharp increase in the antimicrobial activity was observed when antibiotics were adsorbed on the surface of SNPs. Against *B. subtilis*, the inhibition zone increases by 346% when tetracycline adsorbed on SNPs. For *P. fluorescens*, antibacterial efficiency of SNPs increases by 154% and 289%, respectively due to tetracycline and kanamycin adsorption. Both micro-dilution and disk diffusion tests clearly indicate strong antimicrobial activities of SNPs and antibiotic adsorbed SNPs against non-pathogenic strains of *B. subtilis* and *P. fluorescens* [7].

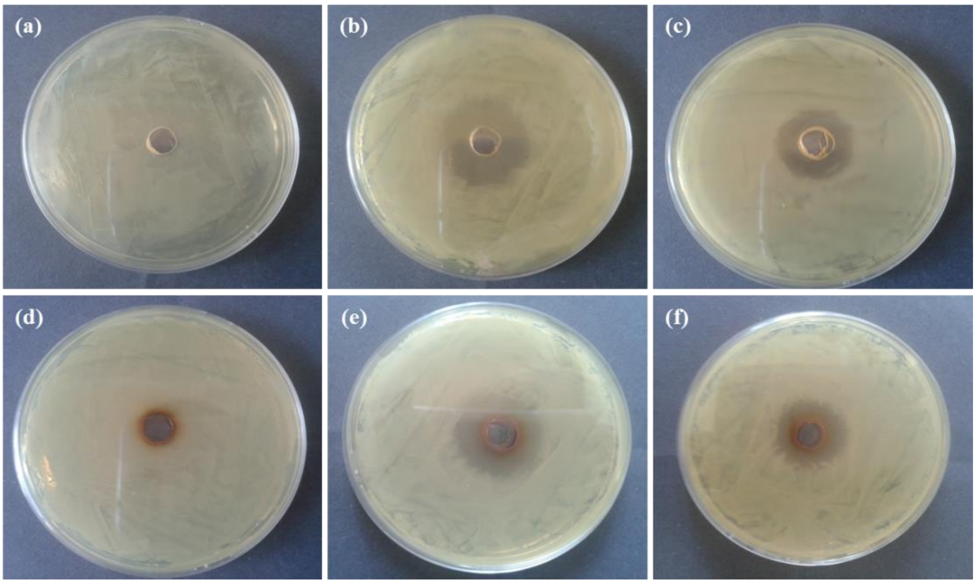

Fig. 4.6 Photographic view of zone of inhibition of *E. coli*, (a) control, (b) tetracycline, (c) kanamycin, (d) SNPs, (e) tetracycline adsorbed SNPs and (f) kanamycin adsorbed SNPs.

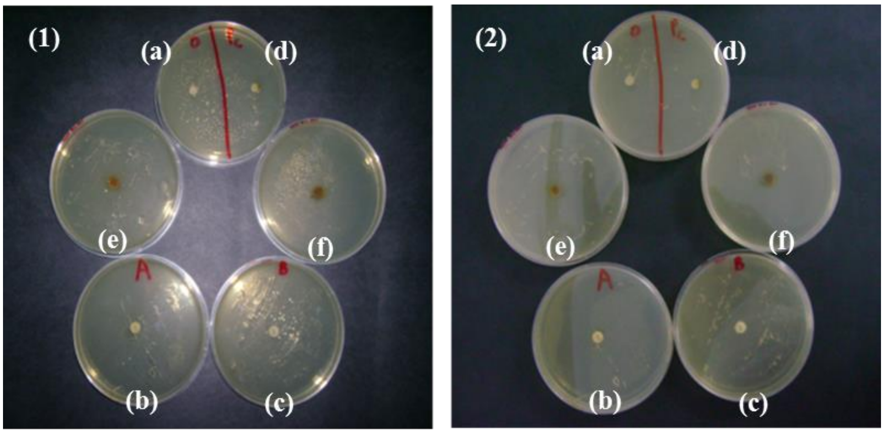

Fig. 4.7 Photographic view of zone of inhibition of (1) *S. aureus* and (2) *P. vulgaris*, (a) control, (b) tetracycline, (c) kanamycin, (d) SNPs, (e) tetracycline adsorbed SNPs and (f) kanamycin adsorbed SNPs.

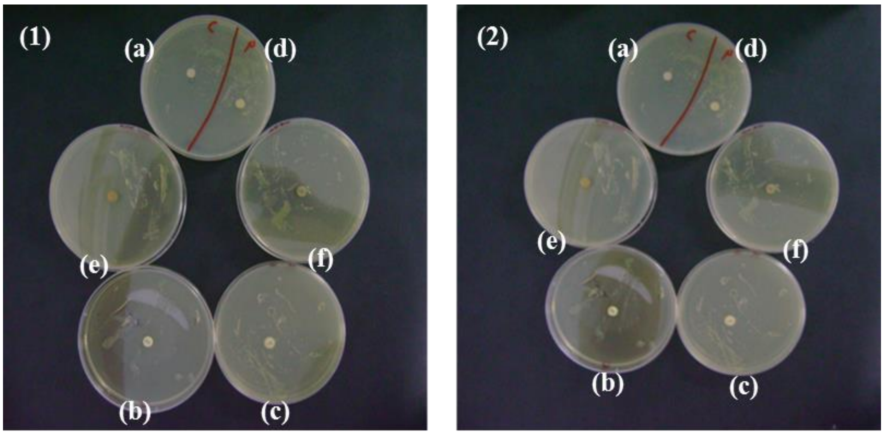

Fig. 4.8 Photographic view of zone of inhibition of (1) *B. subtilis* (2) *P. fluorescens*, (a) control, (b) tetracycline, (c) kanamycin, (d) SNPs, (e) tetracycline adsorbed SNPs and (f) kanamycin adsorbed SNPs.

To study antimicrobial activity of CNPs, the micro-dilution and disk diffusion tests were performed on same pathogenic and environmental friendly bacterial strains. **Fig. 4.9** shows the photographic view of micro-dilution test performed on pathogenic strains. The MIC values of CNPs for *E. coli* and *S. aureus* were equal (20 µg/mL) and for *P. vulgaris*, it was little higher (30 µg/mL). MIC values of CNPs were very small as compared to SNPs for the same bacterial strains. Antibacterial activities of CNPs are better than SNPs. The same was also confirmed from the disk diffusion test.

The results of antimicrobial tests of CNPs for pathogenic microorganisms by disk diffusion method are shown in **Table 4.3**. The inhibition zone was 23 mm for *E. coli* followed by 18 mm for *S. aureus* and 28 mm for *P. vulgaris*. To understand the additive effects of CNPs, the disk diffusion experiments were also carried out for tetracycline adsorbed CNPs and kanamycin adsorbed CNPs. Control experiments containing tetracycline and kanamycin only were also run parallel to these experiments. Images of disk diffusion test for *E. coli*, *S. aureus* and *P. vulgaris* are presented in **Fig. 4.10**, **Fig. 4.11** and **Fig. 4.12**, respectively. ZIH values for these bacterial strains are given in **Table 4.3**. For tetracycline, ZIH was 28, 33 and 16 mm for *E. coli*, *S. aureus* and *P. vulgaris*, respectively. For kanamycin, ZIH was 24, 21 and 25 mm for *E. coli*, *S. aureus* and *P. vulgaris*, respectively. The disk diffusion experiments were also carried out for tetracycline adsorbed CNPs and kanamycin adsorbed CNPs. The ZIH values for tetracycline adsorbed CNPs was 28 mm for *E. coli*, 31 mm for *S. aureus* and 26 mm for *P. vulgaris*. The ZIH values for kanamycin adsorbed CNPs were 25, 21 and 28 mm for *E. coli*, *S. aureus* and *P. vulgaris*, respectively.

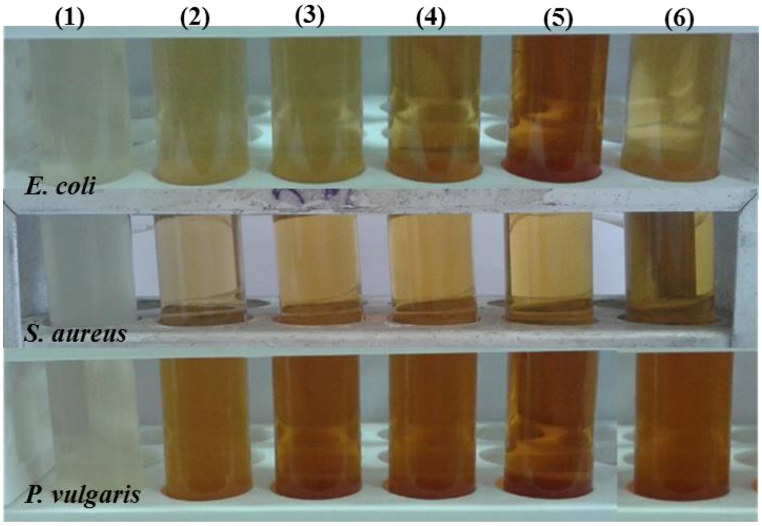

Fig. 4.9 Photographic view of MIC tests of CNPs on *E. coli*, *S. aureus* and *P. vulgaris*. Order of the tubes from left to right: 1. Negative control (i.e., medium alone); 2. Control (i.e., medium + antibacterial agent (CNPs)); 3. Zero concentration (i.e., medium + respective bacterial strain); 4. 30 % below MIC (i.e., medium + respective bacterial strain + CNPs having concentration 30 % below MIC); 5. 10 % below MIC (i.e., medium + respective bacterial strain + CNPs having concentration 10 % below MIC); 6. At MIC (i.e., medium + respective bacterial strain + CNPs having concentration equal to MIC).

The antimicrobial activities of CNPs improved by 0-49% for pathogenic microorganisms under investigation when tetracycline is adsorbed on CNPs while it improved by 0-4% when used with kanamycin. These values were calculated by applying correction for drug loading efficiency (8.6% for tetracycline and 10.63% for kanamycin) in antibiotic adsorbed CNPs. The enhancement in the biocidal activities of antibiotics adsorbed CNPs are small as compared to antibiotics adsorbed SNPs. The antimicrobial activities of CNPs are much better when compared with SNPs.

Table 4.3 Additive effect of commercial antibiotics on antibacterial activities of CNPs.

Strains	**Class**	**Zone of Inhibition (ZIH) (mm)**					
		Control	Tetracycline	Kanamycin	CNPs	Tetracycline adsorbed CNPs	Kanamycin adsorbed CNPs
E. coli	Pathogenic	0	28	24	23	28	25
S. aureus	Pathogenic	0	33	21	18	31	21
P. vulgaris	Pathogenic	0	16	25	28	26	28
B. subtilis	Non-pathogenic	0	34	29	22	32	30
P. fluorescens	Non-pathogenic	0	22	11	28	28	30

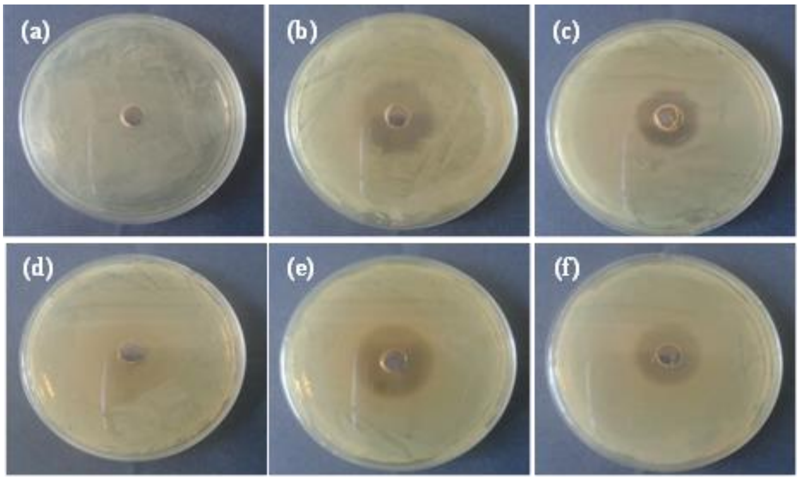

Fig. 4.10 Photographic view of zone of inhibition of *E. coli*, (a) control, (b) tetracycline, (c) kanamycin, (d) CNPs, (e) tetracycline adsorbed CNPs and (f) kanamycin adsorbed CNPs.

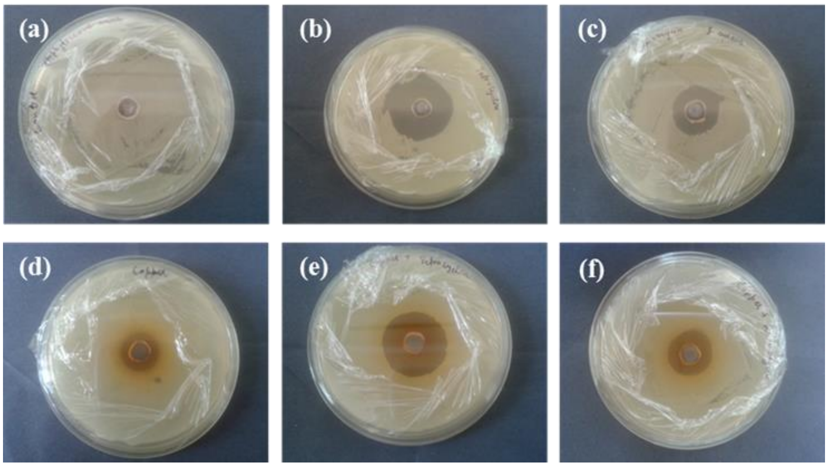

Fig. 4.11 Photographic view of zone of inhibition of *S. aureus*, (a) control, (b) tetracycline, (c) kanamycin, (d) CNPs, (e) tetracycline adsorbed CNPs and (f) kanamycin adsorbed CNPs.

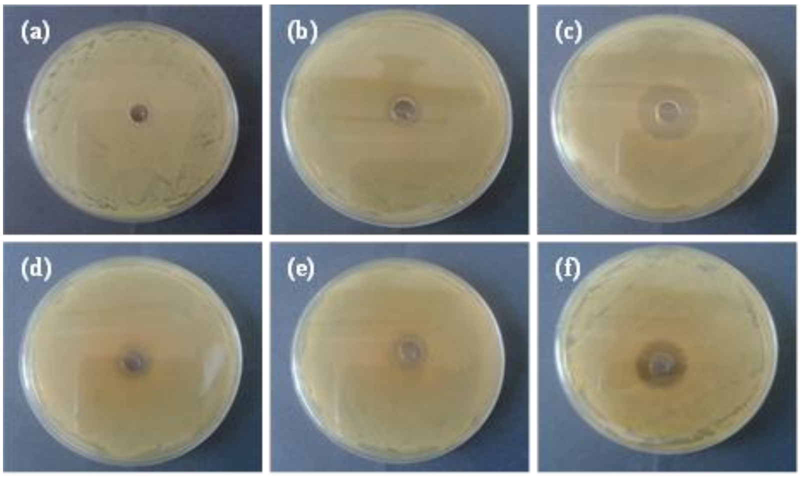

Fig. 4.12 Photographic view of zone of inhibition of *P. vulgaris*, (a) control, (b) tetracycline, (c) kanamycin, (d) CNPs, (e) tetracycline adsorbed CNPs and (f) kanamycin adsorbed CNPs.

The antibacterial activity of CNPs against environmental friendly bacterial strains was also studied. Photographic view of MIC tests and the corresponding values are presented in **Fig. 4.13** and **Table 4.1**. MIC values of CNPs were 50 and 20 µg/mL for *B. subtilis* and *P. fluorescens*, respectively.

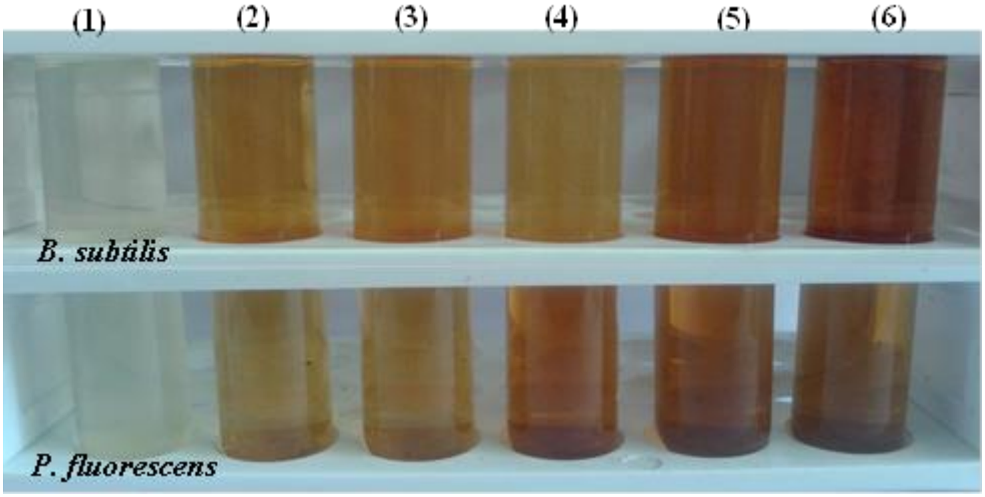

Fig. 4.13 Photographic view of MIC tests of CNPs on *B. subtilis* and *P. fluorescens*. Order of the tubes from left to right: 1. Negative control (i.e., medium alone); 2. Control (i.e., medium + antibacterial agent (CNPs)); 3. Zero concentration (i.e., medium + respective bacterial strain); 4. 30 % below MIC (i.e., medium + respective bacterial strain + CNPs having concentration 30 % below MIC); 5. 10 % below MIC (i.e., medium + respective bacterial strain + CNPs having concentration 10 % below MIC); 6. At MIC (i.e., medium + respective bacterial strain + CNPs having concentration equal to MIC).

To study the additive effect of antibiotics on CNPs, ZIH values were measured for CNPs, tetracycline adsorbed CNPs and kanamycin adsorbed CNPs. Control experiments having tetracycline and kanamycin alone were also run parallel. ZIH values of CNPs, tetracycline adsorbed CNPs and kanamycin adsorbed CNPs were 22, 32 and 30 mm, respectively for *B. subtilis* (**Fig. 4.14**). For *P. fluorescens* (**Fig. 4.15**), these values were 28 mm for CNPs and tetracycline adsorbed CNPs and 30 mm for kanamycin adsorbed CNPs. Increase in the biocidal activities of CNPs against *B. subtilis* was 30% for tetracycline adsorbed CNPs. In case of *P. fluorescens*, no change was observed in the biocidal activities of CNPs when tetracycline adsorbed on CNPs. For kanamycin adsorbed CNPs, this increment was 20% and 3% for *B. subtilis* and *P. fluorescens*, respectively. In case of environmental friendly strains, the additive effect of antibiotics on CNPs is small. This might be because of the adsorption of antibiotic on CNPs at a site that hinders its activity.

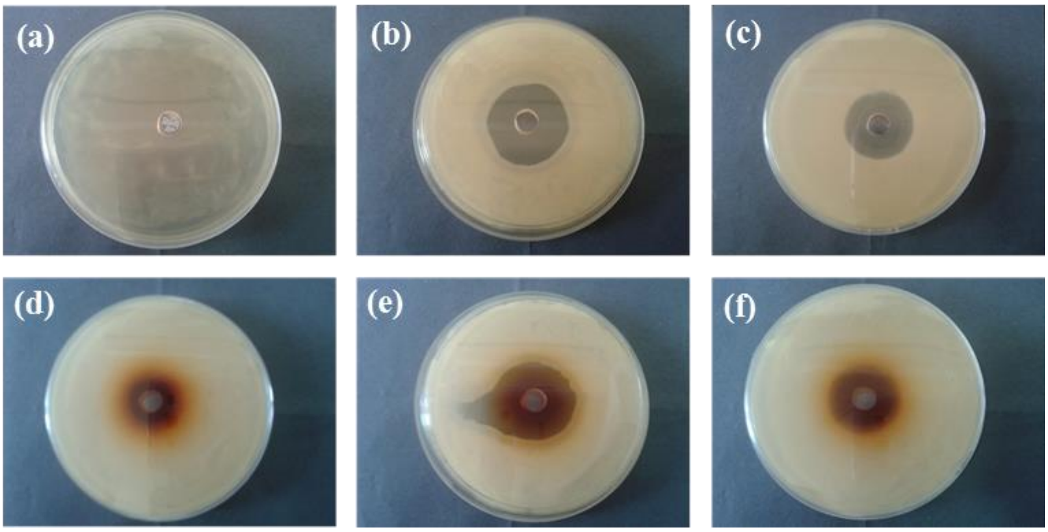

Fig. 4.14 Photographic view of zone of inhibition of *B. subtilis*, (a) control, (b) tetracycline, (c) kanamycin, (d) CNPs, (e) tetracycline adsorbed CNPs and (f) kanamycin adsorbed CNPs.

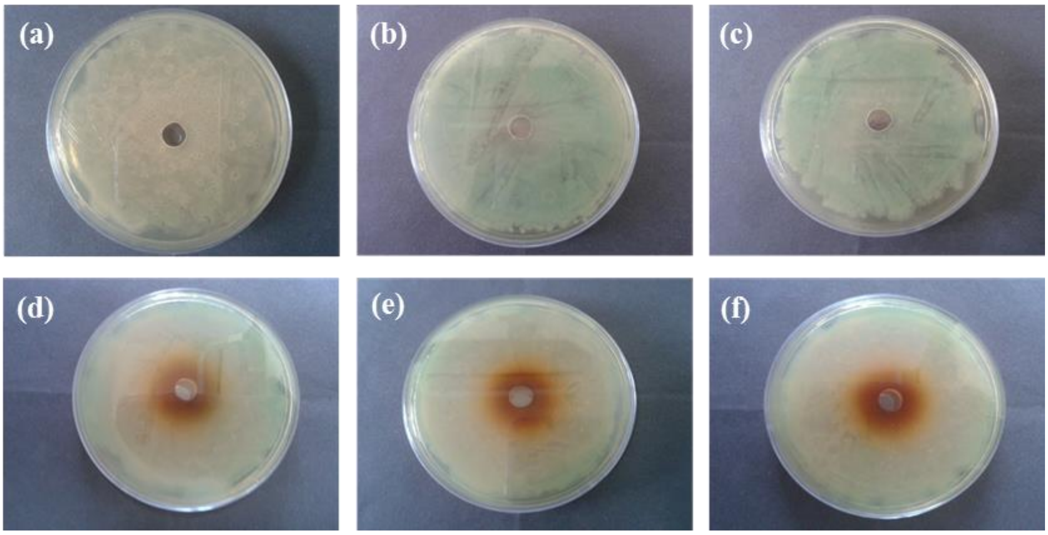

Fig. 4.15 Photographic view of zone of inhibition of *P. fluorescens*, (a) control, (b) tetracycline, (c) kanamycin, (d) CNPs, (e) tetracycline adsorbed CNPs and (f) kanamycin adsorbed CNPs.

Antibacterial activities of TNPs were also evaluated. For this purpose, one pathogenic (*E. coli*) and two environmental friendly (*B. subtilis* and *P. fluorescens*) strains were selected. Out of as-synthesized TNPs, three samples were chosen whose photo-catalytic response belongs to different region of the UV-visible region of the electromagnetic spectrum. The biocidal activity study was conducted under white light by micro-dilution method. No MIC of TNPs was observed against the tested microorganisms for nanoparticles concentration as high as 500 µg/mL. **Fig. 4.16** shows the photographic view of MIC test on *E. coli*, *B. subtilis* and *P. fluorescens*. Bacterial growth was observed in each case, irrespective of TNPs concentration, indicating that TNPs have not inhibited organism growth completely. Hence, no further study was conducted on the biocidal activities of TNPs.

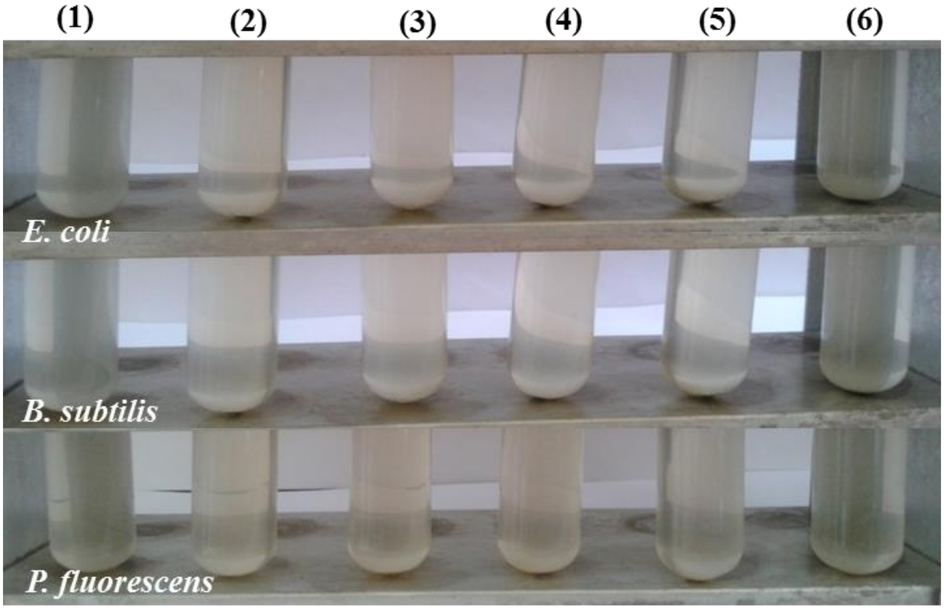

Fig. 4.16 Photographic view of MIC tests of TNPs on *E. coli*, *B. subtilis* and *P. fluorescens*. Order of the tubes from left to right: 1. Negative control (i.e., medium alone); 2. Control (i.e., medium + antibacterial agent (TNPs)); 3. Zero concentration (i.e., medium + respective bacterial strain); 4. 30 % below MIC (i.e., medium + respective bacterial strain + TNPs having concentration 30 % below MIC); 5. 10 % below MIC (i.e., medium + respective bacterial strain + TNPs having concentration 10 % below MIC); 6. At MIC (i.e., medium + respective bacterial strain + TNPs having concentration equal to MIC).

4.10 Mechanism

Nanoparticle toxicity could be due to several attributes, including traits that are particle specific such as their concentration, size, shape, surface charge and release of metal ions. Mechanism of bactericidal action of metal nanoparticles is not well understood. Various mechanisms of antibacterial action of metal nanoparticles on bacterial strains were proposed in literature [6, 9-23]. First step in antibacterial action of nanoparticles is their internalization into bacterial cell. Nanoparticles can diffuse into the cell directly through pores in the cell membrane due to their small size or they may enter through ion channels or through the transport proteins. Some nanoparticles may also enter into the bacterial cells via endocytosis. Nanoparticles which enter into the cell can directly interact with oxidative organelles and induces toxicity to bacterial cells. The toxicity of nanoparticles does not necessarily depend on internalization of nanoparticles. They can change the microenvironment near the bacterial cell wall and release reactive oxygen species (ROS) which induces optosys in bacterial cell. The mechanisms by which metal nanoparticles poison microbial cells can be categorized into the following categories:

1. Impaired membrane function
2. Reactive oxygen species and antioxidant depletion
3. Protein dysfunction
4. Genotoxicity
5. Interference with nutrient assimilation
6. Modulation of signal transduction

These modes of metal nanoparticles toxicity might not be exclusive and it is believed that the growth inhibition and cellular death are likely to be the result of a combination of these mechanisms.

1. Impaired membrane function

Antibacterial action of metal nanoparticles via impaired membrane function is shown in **Fig. 4.17**. Bacterial membranes contain polymers with highly electronegative chemical groups that serve as sites of adsorption for metal cations [9]. Because of their ability to coordinate with metals, it is expected that the membrane is the site where metal nanoparticles exerts bactericidal toxicity. The integrity of cytoplasmic membrane is severely compromised when exposed to toxic doses of metal nanoparticles. The bacterial cell wall is composed mainly of a thick peptidoglycan layer linked to teichoic acid that gives overall negative charge to the cell wall. The negative charge facilitates the interaction between the cell wall and positively charged metal nanoparticles. Such interaction causes the loss of membrane integrity. The damaged membrane allows the entry of substances from the environment, which results into osmotic imbalance. Some metals also disrupt the activity of bacterial electron transport chain [10]. Metal nanoparticles dissipate the chemiosmotic potential of the membrane by causing protein leakage through the membrane [11]. The damaged cell membrane also allows the leakage of minerals and genetic materials. The leakage of cytoplasmic content and consequent rupture of the cell leads to its death.

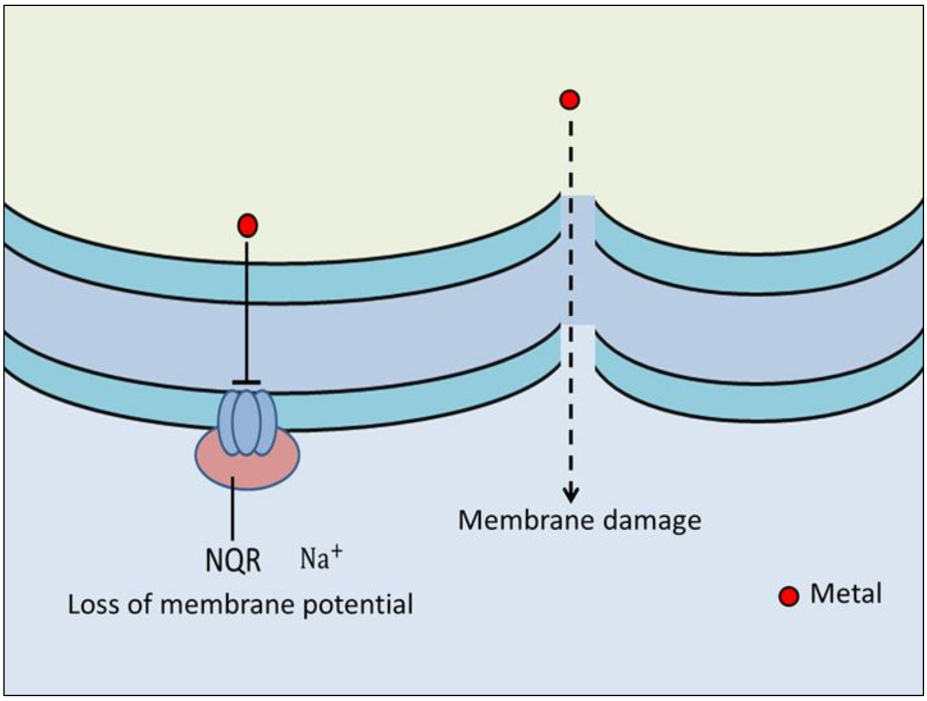

Fig. 4.17 Schematic representation of mechanism of Impaired Membrane Function induced toxicity in bacterial cells. Solid line represents pathway in which biochemistry has been elucidated, whereas dashed arrow represents a route of toxicity for which the biochemical mechanism is unclear. NQR represents NADH:quinone oxidoreductase [6].

2. Reactive oxygen species and antioxidant depletion

Toxicity of metal nanoparticles could be due to the ROS mediated cellular damage or it could be due to the metal catalysed oxidation reaction that could underline specific proteins, membrane or DNA damage. The antibacterial mechanism of metal nanoparticles by means of ROS and antioxidant depletion is shown in **Fig. 4.18**. Three mechanisms have been proposed which accounts for increased ROS production during the metal nanoparticles poisoning of bacteria. First, certain redox active transition metals can catalyse Fenton reaction, which gives rise to partially reduced form of molecular oxygen (O_2) such as hydrogen peroxide and superoxide. Second, metal nanoparticles might disrupt the cellular donar legends that coordinate with metal ions. Mounting evidence suggest that the primary targets for various metals are the solvent exposed (4Fe-4S) clusters of proteins [12]. The direct or indirect destruction of (4Fe-4S) clusters by metals could result in the release of additional Fenton active Fe into the cytoplasm resulting in increased ROS formation. Third, thiol-mediated reduction of some metal species leads to the generation of ROS via intermediate S radical chemistry [13]. Thiol-mediated reduction could produce other metal species that are Fenton active. Increasing ROS level in the cellular environment leads to the rapid degradation of cellular contents that eventually leads to the cell death.

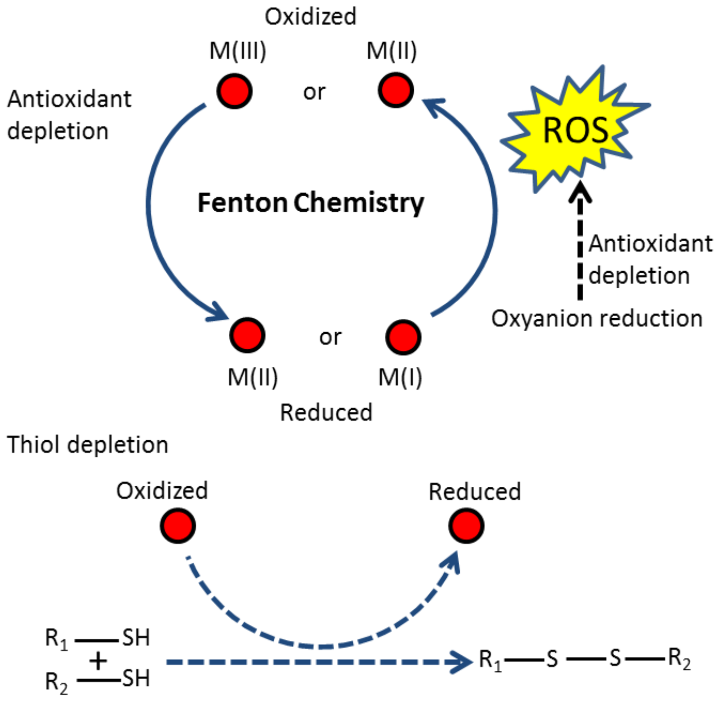

Fig. 4.18 Metal ion induced Production of reactive oxygen species (ROS) and antioxidant depletion in cellular environment. Red sphere represents metal ions released from metal nanoparticle. Solid arrows represent pathways in which biochemistry has been elucidated, whereas dashed arrows represent a route of toxicity for which the biochemical mechanism is unclear [6].

An important aspect of oxidative stress during bacterial metal poisoning is the oxidation of cellular thiols. Metal ions have electron sharing affinities that can result in the energetically favourable formation of covalent bonds with S, which can lead to the formation of protein disulphides and depletion of antioxidant reserves, particularly glutathione, within microbial cells [14,15]. Glutathione depletion could leave protein targets vulnerable to attack by metal species or ROS. It also prevents repair of oxidized protein-thiols by cellular thiol-disulphide exchange enzymes and thus enhances the possibility of oxidative stress induced cellular damaged in bacteria.

3. Protein dysfunction

Protein dysfunction induced metal nanoparticle poisoning of bacterial cell is presented in **Fig. 4.19**. One or more amino acid residue in a protein is susceptible to metal-catalysed oxidation [16]. Oxidation of amino acid side chains in proteins may cause loss of catalytic

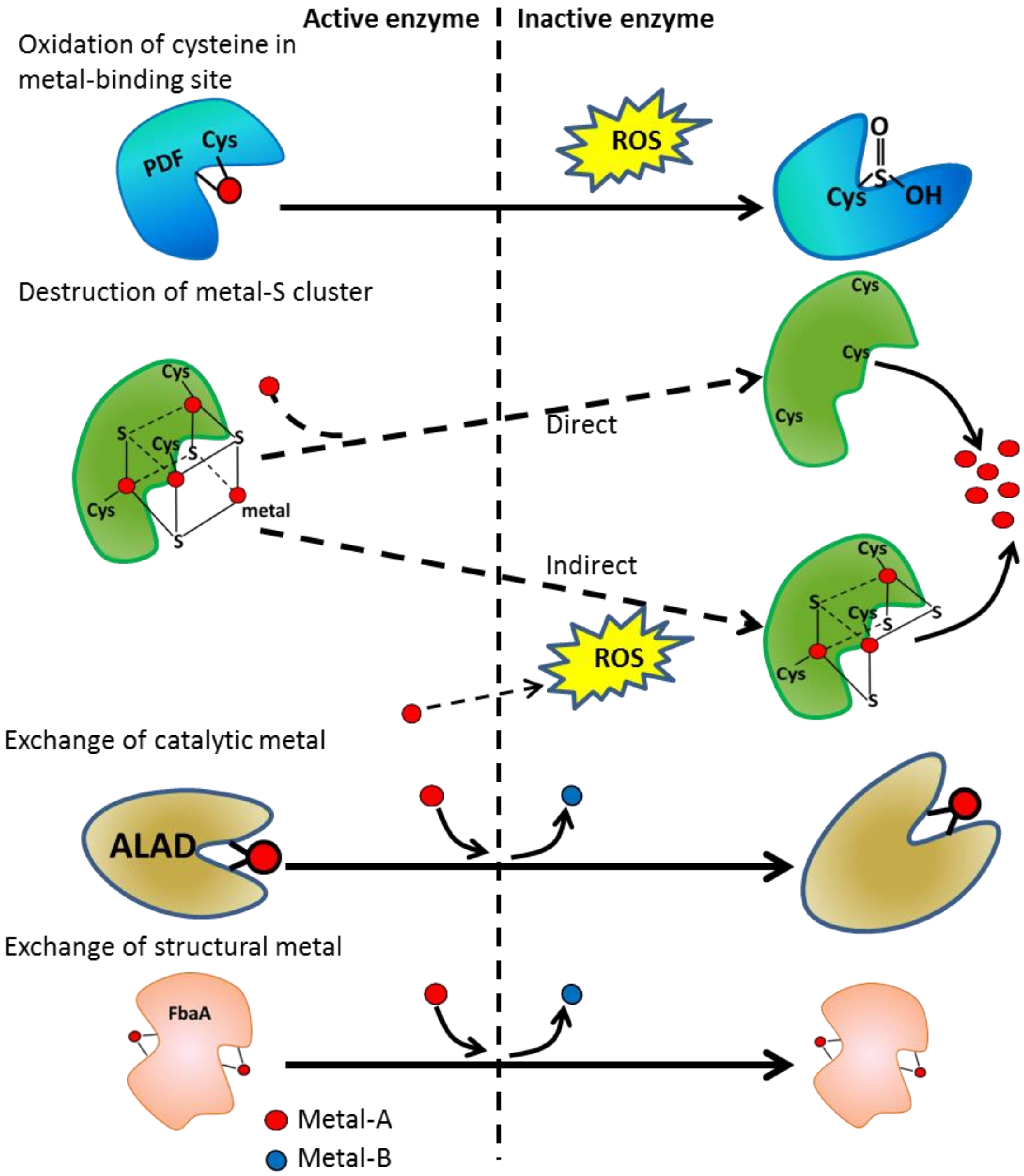

Fig. 4.19 Schematic representation of various modes of Protein dysfunction induced cellular toxicity. Solid arrows represent pathways in which biochemistry has been elucidated, whereas dashed arrows represent a route of toxicity for which the biochemical mechanism is unclear. Here ALAD, δ-aminolevulinic acid dehydratase; FbaA, fructose-1,6-bisphosphate aldolase; PDF, peptide deformylase [6].

activity and trigger an active process of protein degradation [16]. Hence, metal nanoparticles could catalyse site-specific damaged to cellular proteins. This damage might be responsible for toxicity of metal nanoparticles. Toxicity of metal nanoparticles is also associated with decrease activities of fumarase A and 6-phosphogluconate dehydratase, two enzymes that depend on Fe-S clusters for catalysis [17]. This activity is different from ROS toxicity as it is independent of oxygen. Another mechanism of site-specific enzymes inhibition that can result in metal nanoparticles poisoning is ionic mimicry in which an unbound cationic metal species mimics as essential element. In addition to destruction of active sites, metal substitution at non-catalytic binding sites can also inhibit enzyme activity.

4. Genotoxicity

The genotoxicity induced antibacterial activity of metal nanoparticles is schematically shown in **Fig. 4.20**. Metal mediated Fenton chemistry can catalyse lethal DNA damage in bacteria. For instance, mutations that disrupt metal homeostasis increase the amount of Fenton active metal ions in the cell. This accelerates DNA damage and causes cell death [18]. It has been reported that toxic doses of metal nanoparticles increase the intracellular reactive oxygen species (ROS). The exogenous addition of hydrogen peroxide (H_2O_2) or agents that catalyse the production of superoxide such as paraquat, leads to DNA damage and inhibits particular enzyme activities that are vital for cell growth [19]. Toxic doses of metal nanoparticles can also upregulate genes that are involved in the elimination of ROS [20]. Metal ions are released from nanoparticles and interfere with DNA replication [21]. DNA loses its replication ability and expression of ribosomal subunit when microorganisms were exposed to metal ions.

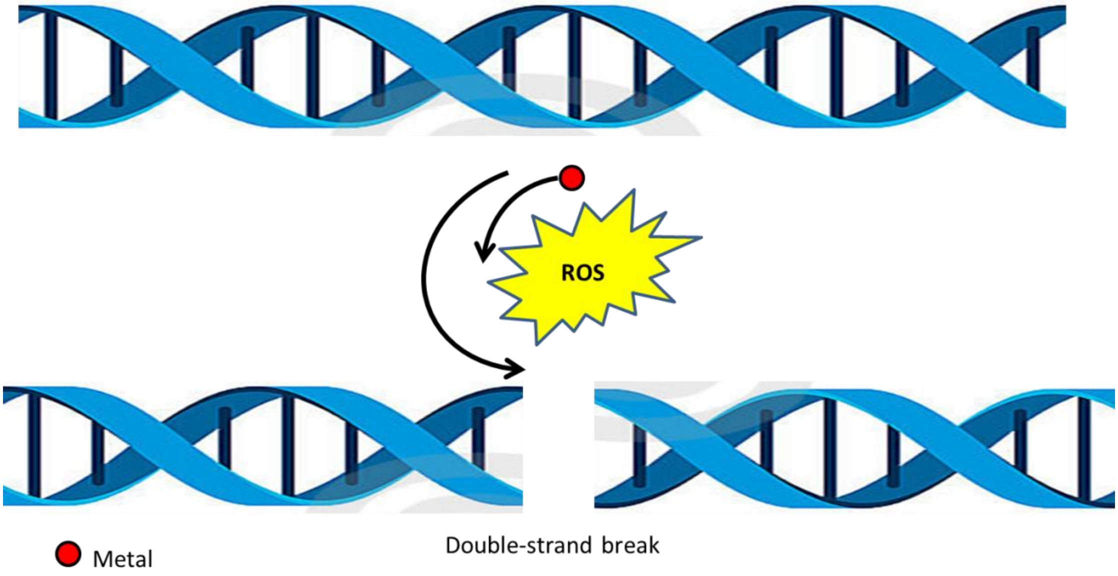

Fig. 4.20 Schematic representation of mechanism of metal ion induced Genetoxicity in bacterial cells [6].

5. Interference with nutrient assimilation

The schematic diagram of metal nanoparticles toxicity due to interference with nutrient assimilation in bacterial cells is shown in **Fig. 4.21**. The toxicity of metals is also linked to starvation-induced growth arrest. Metal nanoparticles inhibit the uptake of sulphate, deplete intracellular S metabolite pools and induce enzymes of S-sparing response [22]. Because supplementation with sulphate and other S sources mitigates toxicity in a concentration dependent manner, it has been suggested that metal nanoparticles starve cells of S by interfering with its sulphate uptake and thus induces the cell optosys.

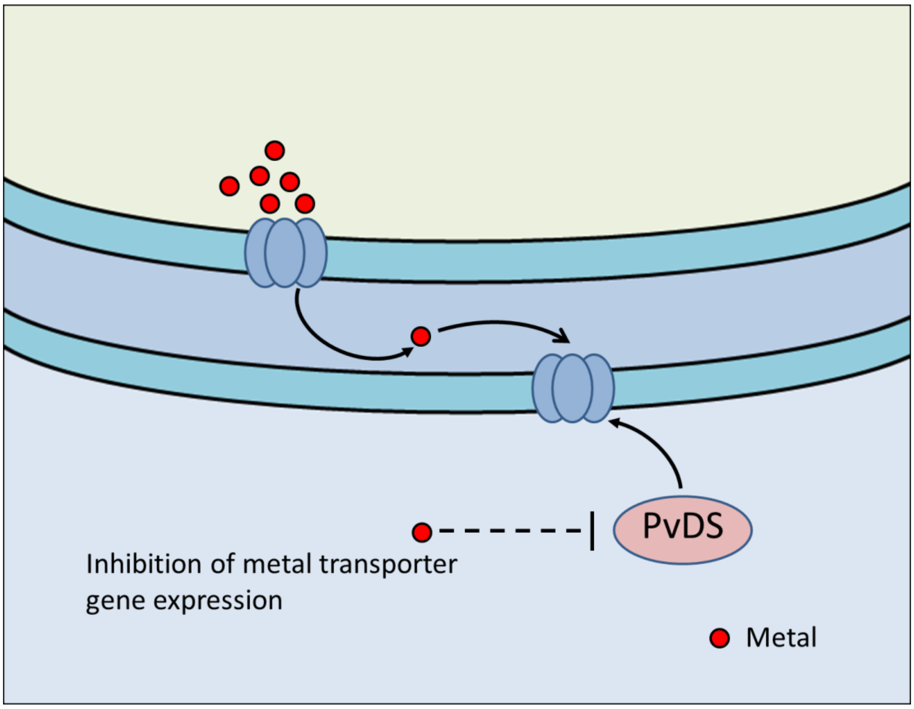

Fig. 4.21 Schematic representation of metal nanoparticles induced toxicity due to the interference of metal ions released from the metal nanoparticles with the nutrient uptake. Here PvdS, a σ-factor (σ^{24}) from *Pseudomonas aeruginosa* [6].

6. Modulation of signal transduction

Nanoparticles can modulate signal transduction in bacteria. It is a well-established fact that phosphorylation of protein substrates in bacteria influences bacterial signal transduction [23]. Dephosphorylation is present in tyrosine residue of gram negative bacteria. The phosphotyrosine profile of bacterial peptides is altered by nanoparticles. Metal nanoparticles dephosphorylate the peptide substrates on tyrosine residues, which lead to signal transduction inhibition and thus stoppage of growth which eventually leads to the cell destruction [23]. Biocidal activities of SNPs and CNPs reported here is due to one or more of this microscopic cellular phenomenon.

References

1. Sondi and B. S. Sondi, Journal of Colloid and Interface Science 275, 177-182 (2004).
2. J. R. Morones, J. L. Elechiguerra, A. Camacho, K. Holt, J. B. Kouri, J. T. Ramirez and M. J. Yacaman, Nanotechnology 16, 2346-2353 (2005).
3. S. L. Percival, P. G. Bowler and D. Russell, Journal of Hospital Infection 60, 1-7 (2005).
4. G. Lancini, F. Parenti and G. G. Gallo, Antibiotics: A multidisciplinary Approach, 2nd Ed., Springer Science BV. (1993).
5. A. Azam, A.S. Ahmed, M. Oves, M. S. Khan, S. S. Habib and A. Memic, International Journal of Nanomedicine 7, 6003-6009 (2012).
6. J. A. Lemire, J. J. Harrison and R. J. Turner, Nature Reviews Microbiology 11, 371-384 (2013).
7. M. T. Madigan, J. M. Martinko, D. A. Stahl and D. P. Clark, Block Biology of Microorganisms, 13th Ed., Pearson (2012).
8. J. Zhang and R. Misra, Acta Biomaterialia 3, 838-850 (2007).
9. Y. M. Zhang and C. O. Rock, Nature Reviews Microbiology 6, 222-233 (2008).
10. C. N. Lok, C. M. Ho, R. Chen, Q. Y. He, W. Y. Yu, H. Sun, P. K. Tam, J. F. Chiu and C. M. Che, Journal of Proteome Research 5, 916-924 (2006).
11. P. Dibrov, J. Dzioba, K. K. Gosink and C. C. Hase, Antimicrobial Agents and Chemotherapy 46, 2668-2670 (2002).
12. J. Middaugh, R. Hamel, G. Jean-Baptiste, R. Beriault, D. Chenier and V. D. Appanna, The Journal of Biological Chemistry 280, 3159-3165 (2005).
13. M. Valko, H. Morris and M. T. D. Cronin, Current Medicinal Chemistry 12, 1161-1208 (2005).
14. K. Helbig, C. Bleuel, G. J. Krauss and D. H. Nies, Journal of Bacteriology 190, 5431-5438 (2008).
15. K. Helbig, C. Grosse and D. H. Nies, Journal of Bacteriology 190, 5439-5454 (2008).
16. E. R. Stadtman, Annual Review of Biochemistry 62, 797-821 (1993).
17. L. Macomber and J. A. Imlay, Proceedings of the National Academic of Sciences, USA 106, 8344-8349 (2009).
18. D. Touati, M. Jacques, B. Tardat, L. Bouchard and S. Despied, Journal of Bacteriology 177, 2305-2314 (1995)
19. J. A. Imlay, Annual Review of Microbiology 57, 395-418 (2003).
20. G. M. Teitzel, A. Geddie, S. K. De Long, M. J. Kirisits, M. Whiteley and M. R. Parsek, Journal of Bacteriology 188, 7242-7256 (2006).
21. L. Sintubin, B. D. Gusseme, P. V. Meeren, B. F. G. Pycke, W. Verstraete and N. Boon, Applied Microbiology and Biotechnology 91, 153-162 (2011).
22. Y. Pereira, G. Lagniel, E. Godat, P. Baudouin-Cornu, C. Junot and J. Labarre, Toxicological Sciences 106, 400-412 (2008).
23. S. Prabhu and E. K. Poulose, International Nano Letters 2, 32-41 (2012).

CHAPTER 5

CONCLUSIONS AND SCOPE FOR FUTURE WORK

5.1 Conclusions

Major conclusions drawn out of the research work carried out to meet the objectives of this thesis are as follows:

Well dispersed, uniform SNPs with controllable size and narrow size distribution are prepared by chemical reduction technique. Nanoparticles' yield, their morphology, particle size, polydispersity and agglomeration are strongly correlated with concentration of reducing cum capping agent (oleylamine) and other kinetic parameters like nucleation temperature, nucleation time, growth temperature and growth time. Optimized conditions for these parameters have been established for which smallest particle size (< 10 nm), narrowest polydispersity (≈ 0.12) and highest yield (≈ 46%) of SNPs were obtained. Nucleation at 200 °C for 30 min and growth at 150 °C for 4 h are the optimum processing parameters for highest nanoparticle yield, lowest particle size and polydispersity index with no or very little aggregation.

Present study also reveals that oleylamine traditionally known as reducing and capping agent, also functions as grain growth inhibitor. 15 mM is the optimized concentration of reducing agent to prepare well dispersed self-assembled spherical SNPs. Below this concentration, SNPs aggregate strongly due to the lack of monolayer coating of oleylamine. Growth of SNPs follows the classical condensation mechanism. Oleylamine coating on SNPs make them hydrophobic. For medical applications, nanoparticles need to be hydrophilic. Hence, a facile phase transfer protocols have been developed to transfer hydrophobic SNPs into hydrophilic by ligand-exchange reaction using pluronic F-127. No deviation in the physical or surface properties of SNPs has been observed after the phase transfer.

Well dispersed, uniform colloidal CNPs with controllable hydrodynamic size and narrow particle size distribution were obtained by reducing copper (II) chloride with a combination of strong ($NaBH_4$) and weak (L-ascorbic acid) reducing agents in the presence of a surfactant (PVP). Concentration of strong reducing agent, weak reducing agent and capping agent has major impact on the crystal phase, size and size distribution of CNPs. Absence of the strong reducing agent or the weak reducing agent or the surfactant either does not form CNPs or the formed nanoparticles are not stable and get oxidized. Present study reveals that in addition to strong reducing agent, a secondary weak reducing agent is essential to simulate dynamic equilibrium around the surface of CNPs, which prevents their oxidation and stabilizes the metallic copper phase. Spherical, ultra-small CNPs with uniform physical size (≈ 2 nm) are synthesized at 80 °C under optimized conditions when concentration of each PVP, $NaBH_4$ and L-ascorbic acid is 10 mM. The protocols developed here for the synthesis of air stable CNPs do not require any inert environment / protective gases. As-synthesized CNPs form stable aqueous colloidal dispersion, which do not show any sign of aggregation or oxidation even after their storage under ambient conditions for 120 days.

Pristine and cobalt doped TNPs are prepared by sol-gel technique. Titanium (IV) isopropoxide is hydrolysed and condensed into amorphous titanium dioxide gel by water / ethanol under acidic conditions. Amorphous TiO_2 gel is crystallized into anatase crystallographic phase when calcine at 500 °C. The optical band gap of pristine (0% Co doped) TNPs is 3.03 eV (λ = 409 nm), which decreases upto 1.93 eV (λ = 642 nm) when Co concentration in TiO_2 matrix increases from 0 to 2%. Co(+2) substitution at Ti(+4) site generates additional oxygen vacancies in the titania unit cell, which introduces extra energy levels in the forbidden band that reduces the indirect energy band gap of TNPs. Irrespective of the Co concentration, TNPs always crystallize into anatase phase when calcined at 500 °C. No signature of other isomorphous phases i.e. rutile or brookite are detected. With increasing Co doping, the amorphous to crystallization anatase phase transition temperature increases from 404 °C to 454 °C. The average physical size obtained from SEM measurement is ≈ 10 nm. Co doping in TNPs make them sensitive to visible radiation and, hence their photoresponse is expected to be better under sun light than pristine bulk titania, which is active in the UV-region of the electromagnetic spectrum.

Antibacterial activities of as-synthesized SNPs, CNPs and TNPs have been investigated against clinically important pathogenic strains (*E. coli*, *S. aureus* and *P. vulgaris*) and eco-friendly microorganisms (*B. subtilis* and *P. fluorescens*). No biocidal activities of pristine and cobalt doped TNPs are observed against microorganisms under test for TNPs concentration as high as 500 µg/mL both under dark and light conditions. Strong antimicrobial activities are observed in case of SNPs and CNPs against both pathogenic and non-pathogenic strains under investigation. Amongst SNPs and CNPs, CNPs report enhanced biocidal activities against all tested microorganisms (pathogenic and non-pathogenic), whose minimum inhibitory concentration values lie in the range of 20 - 50 µg/mL. For SNPs, the minimum inhibitory concentration values against the same set of microorganisms fall in the range of 25 -150 µg/mL. CNPs are equally effective against all tested microorganisms as no significant variation in their MIC values is observed. SNPs exhibit strongest biocidal activities against both the eco-friendly strains and one pathogenic strain (*E. coli*). *S. aureus* is least vulnerable to SNPs (MIC = 150 µg/mL). Results reported here are either better or comparable to those found in literature.

To understand the effect of adsorption of commercial antibiotics (tetracycline and kanamycin) on SNPs and CNPs, antibiotic adsorbed SNPs and antibiotic adsorbed CNPs formulations have also been prepared. The loading efficiency of tetracycline in SNPs is 15.3% while for CNPs, it is 8.6%. The loading efficiency of kanamycin is 6.44% for SNPs and 10.63% for CNPs. The antibacterial activities of antibiotics adsorbed nanoparticles formulations have been evaluated by disk diffusion test, in which zone of inhibition is measured both for pristine (SNPs / CNPs) and antibiotic adsorbed nanoparticles (tetracycline adsorbed SNPs / kanamycin adsorbed SNPs / tetracycline adsorbed CNPs / kanamycin adsorbed CNPs). The percentage enhancement of antibiotic efficiency of SNPs when antibiotic (tetracycline / kanamycin) get adsorbed on their surface is in the range of 66 - 346% for tetracycline and 70 - 289% for kanamycin. Such strong enhancement in the biocidal activities of CNPs is not observed when antibiotics get adsorbed on the surface of CNPs. The enhancement in the biocidal activities of CNPs lies in the range of 0 - 49% for tetracycline and 0 - 20% for kanamycin. The vast difference between the enhancement in the biocidal activities of SNPs and CNPs when antibiotics are adsorbed on their surface might be because of the difference in the site of adsorption of antibiotics on nanoparticles' surface, which is making them active or inactive. Both tetracycline and kanamycin adsorption on SNPs are equally effective while tetracycline is more effective compare to kanamycin when adsorbed on CNPs. Results of antibacterial tests of nanoparticles and their formulations with antibiotics are summarized in **Table 5.1**.

Table 5.1 Summary of antibacterial activities of nanoparticles and their formulations with antibiotics tetracycline and kanamycin.

Strains	**Class**	**Nature**	**MIC (µg/ mL)**			**Zone of Inhibition (ZIH) (in mm)**							
			SNPs	CNPs	TNPs	Tetracycline	Kanamycin	SNPs	CNPs	Tetracycline adsorbed SNPs	Tetracycline adsorbed CNPs	Kanamycin adsorbed SNPs	Kanamycin adsorbed CNPs
E. coli	Pathogenic	Gram -ve	30	20	Nil	28	24	12	23	27	28	23	25
S. aureus		Gram +ve	150	20	------	33	21	11	18	34	31	26	21
P. vulgaris		Gram -ve	100	30	------	16	25	7	28	27	26	27	28
B. subtilis	Non-pathogenic	Gram +ve	25	50	Nil	34	29	6	22	50	32	20	30
P. fluorescens		Gram -ve	25	20	Nil	22	11	7	28	40	28	30	30

Overall conclusion of the entire study is that out of the three nanoparticle systems designed in the present study, CNPs are most lethal on tested microorganisms. This is in contradiction with the existing literature where highest biocidal activities are reported for SNPs. This could be because of their ultra-small particle size (2 nm) and very high resistance towards oxidation and aggregation. Both nanoparticle systems (SNPs and CNPs) and their formulations with antibiotics are more toxic to eco-friendly strains than to pathogenic ones. Antimicrobial activities of antibiotic adsorbed nanoparticles are higher than the discrete sum of biocidal activities of individual components (nanoparticles and antibiotics). Thus nanoparticle-antibiotic formulations can be used to further enhance the biocidal activities of commercial antibiotics.

5.2 Scope for future work

This thesis reports synthesis of three nanoparticulate systems (SNPs, CNPs and TNPs) and evaluation of antimicrobial activities of these nanoparticles and their formulations with commercial antibiotics tetracycline and kanamycin. Enhanced antimicrobial activities of SNPs and CNPs along with their formulations with commercial antibiotics have been observed. This piece of work could find potential applications in pharmaceutical industries. However, for industrial utilization of these nanostructures and their formulations with commercial antibiotics, synthesis protocols and their subsequent processing with antibiotics need to be modified suitably. In particular, the process needs to be scaled up to make it economically viable for their use as non-traditional antibiotics in health-care industry.

Before commercial utilization of any drug or health-care product, they need to meet certain standards set by food and drug administration. These standards basically define exposure limits of drugs or health-care products. For nanomaterials or nanomaterials based products, such standards are not available. Hence, toxicity of these nanoparticles and their formulations with antibiotics needs to be investigated as per the standard protocols for any potential nanomaterial based new drug. Based on the outcome of this study, exposure limits for these nano-antibiotics needs to be defined.

Antimicrobial activities of metals and their oxides is a vibrant field of research in today’s nanobiotechnology. Most of the investigated nanostructures for their biocidal activities are toxic to human cells and because of this, they cannot be used for *in-vivo* purposes. Amongst the biocompatible class of nanomaterials, those showing biocidal activities are of great industrial relevance. Amongst them, SNPs and CNPs are the chief candidates for potential applications in preventive and curative healthcare. There are multiple reports of their biocidal activities along with the present one in this thesis. Despite of wide spread study of this aspect of SNPs and CNPs, the exact mechanism responsible for their biocidal activities are largely unclear. A detailed study needs to be conducted to understand the mechanism responsible for biocidal activities of SNPs and CNPs. The current literature predicts that pathogenic microorganisms, which are developing new strains by mutation are resistant to one or more first line antibiotics, are unlikely to develop such resistance against SNPs and CNPs. However, detailed study of this aspect is completely missing and needs to be evaluated urgently as many health-care products are now using nanostructures at commercial level. Any possible mutation of pathogenic strains that is resistant to these nanostructures would be devastating and very difficult to control.

Nanomaterials are now commercially explored in large number of technical, engineering and medical products. Nanoparticles will eventually leach out from these materials and will accumulate in water and land fields. These accumulated nanostructures may cause severe damage or alteration to terrestrial ecosystems of the earth by interacting with microbes, which are playing critical role in various natural cycles. Such interactions between nanoparticles leaching out from the toxic nanomaterials’ waste and eco-friendly microorganisms present in soil, water, air and plants have potential to extinct these microorganisms. Hence, environmental concerns of nanomaterials need to be addressed urgently and a systematic study is essential that will include impact of commercial nanoparticles on microbes of terrestrial and marine origin. The outcome of such study will eventually define permissible levels of nanomaterials in air, land and water bodies. A separate study can also be conducted on remediation and recycling of nanostructured based pollutants.